NANO-EPITAXY MODELING AND DESIGN: FROM ATOMISTIC SIMULATIONS TO CONTINUUM METHODS

A Dissertation
Presented to
The Academic Faculty

by

Wei Ye

In Partial Fulfillment
of the Requirements for the Degree
Doctor of Philosophy in the
School of Mechanical Engineering

Georgia Institute of Technology
December 2013

NANO-EPITAXY MODELING AND DESIGN: FROM ATOMISTIC SIMULATIONS TO CONTINUUM METHODS

Approved by:

Dr. Mohammed Cherkaoui, Co-Advisor
School of Mechanical Engineering
Georgia Institute of Technology

Dr. Abdallah Ougazzaden, Co-Advisor
School of Electrical and Computer Engineering
Georgia Institute of Technology

Dr. Ting Zhu
School of Mechanical Engineering
Georgia Institute of Technology

Dr. Richard W. Neu
School of Mechanical Engineering
Georgia Institute of Technology

Dr. Hanchen Huang
School of Mechanical Engineering
University of Connecticut

Date Approved: October 18, 2013

To my family

ACKNOWLEDGEMENTS

For this work, I need to devote my thanks to my co-advisors, Dr. Cherkaoui and Dr. Ougazzaden first. Now I still remember that, when I came to Georgia-tech, Lorraine campus in the summer of 2008, both of them welcomed me to join this work group. Our work is indeed a close cooperation between the ME lab, which I am currently in, and one ECE lab working on semiconductor nano-epitaxy. The ME lab is about material designs by computing and modeling method under the direction of Dr. Cherkaoui, while the ECE lab can provide experimental support with the help of Dr. Ougazzaden. Therefore, I feel grateful to benefit from both sides.

During the process of this work, I am fortunate to receive the help of many other people. For technical problems, especially at the beginning of doing molecular dynamic simulations, I honestly devote my thanks to Dr. Raulot who is not registered in Georgia-tech, Lorraine campus but works in the lab of University of Metz here in France. I thank him deeply for his enthusiasm and discussions on simulations. I also want to thank the people I have been working with here in the city of Metz. I truly enjoy the discussions with my colleagues, Dr. Berbenni, Sadiq, Malek and Mathieu. As for this dissertation, I want to thank the committee members, Dr. Zhu, Dr. Neu and Dr. Huang, for their kindness to serve in my committee and their suggestions on my work.

After this, I need to thank a group of people here that have made my life in this campus merry and colorful, such as Jingfei, Ning, Zheshen and many, many others that I can’t list out here. Especially, I feel foremost grateful to Mr. Leslie Cheung, whose art work enchanted me and the personality influenced me profoundly.

At the end, I will always thank my family in my homeland. My grandma and parents were a little worried when I chose the pursuit of studying abroad, but they supported me unconditionally. My brother is the one always encouraging me up and always giving his advices to me. Above all, I dedicate this dissertation to my family with all my love.

TABLE OF CONTENTS

LIST OF TABLES

Page

LIST OF FIGURES

Page

SUMMARY

Nano-epitaxy is widely used in nanotechnologies and semiconductor fabrications. Nowadays III-nitride materials (GaN, AlN, InGaN, etc.) are widely investigated for the next generation semiconductors due to their wide bandgap and the potential to deliver high quality illumination with high efficiency. However, defects, especially dislocations, may lead the device to poor properties (mechanical, electrical and optical), so it becomes critical and inevitable to minimize such defects. This work aims at a systematic investigation about the dislocation dissipation mechanism in nanostructures by combining the surface effect at atomistic level and the mechanical model at macroscopic level. It is intended to provide some feasible and reliable design tools or routines for growing high quality nanostructures. It will contribute to providing guidance for the fabrication of next-generation dislocation-free nano-devices.

The dissertation starts from the understanding of dislocation dissipation mechanism due to the image force acting on the dislocation. This work implements a screw dislocation in solids with free surfaces by a novel finite element model, and then image forces of dislocations embedded in various shaped GaN nanorods are calculated. By comparing with critical force to overcome the lattice resistance, it will demonstrate the mechanism of dislocation dissipation in GaN nanorods. As surface stress could dramatically influence the behavior of nanostructures, this work has developed a novel analytical framework to solve the stress field of solids with dislocations and surface stress. The core idea of this framework is to combine the general eigenstrain problem solution from micromechanics and the surface elasticity model from atomistic studies.

The surface elasticity tensors are obtained through Molecular Dynamic (MD) simulations, and especially a complete dataset of GaN surface property tensors will be calculated and it could be used to study the surface effect of GaN nanostructures in the future. In principle, the analytical framework could be applied to general anisotropic 3D materials which are unable to be handled by other literature works (mostly based on complex potential method and its variants). Furthermore, it is successfully implemented in this framework for the case of isotropic circular nanowires (2D) and the analytical result of the image force has been derived afterwards. With the very few results available in literatures, this work could contribute to the pioneering work regarding the interaction between dislocations and surface stress.

Based on the finite element analysis and the analytical framework, this work has proposed the combination of these two approaches and come up with a semi-analytical solution to the image force of isotropic nanorods (3D) with surface stress. The influences of the geometrical parameter and surface stress are illustrated and compared with the original finite element result. In continuation, this work has extended the semi-analytical approach to the case of anisotropic GaN nanorods. It is used to analyze image forces on different dislocations in GaN nanorods oriented along polar (c-axis) and non-polar (a, m-axis) directions. The result shows the dislocation dissipation could be more effective in a-GaN but less in m-GaN by comparing with the standard growth of c-GaN. The approach developed in this work is applicable to other material systems, such as GaAs, InGaN etc. Therefore, it could contribute to a wide range of nanostructure design and fabrication for dislocation-free devices.

CHAPTER 1

INTRODUCTION

This chapter provides an introduction to the research conducted in the PhD work. First, the motivations to do nano-epitaxy modeling and design will be discussed. Second, we will make a broad and comprehensive literature review on this topic, which could also be the foundation for our work. Finally, we will present the objectives and goals of the PhD research. This could be seen as a brief guideline to the current dissertation.

Motivations

For decades, epitaxy is used in nanotechnologies and semiconductor fabrications. So far, it's the only affordable method of high quality crystal growth for many semiconductor materials. Heterostructures developed from these make it possible to solve the considerably more general problem of controlling the fundamental parameters inside the semiconductor crystals and devices [1]: band gaps, effective masses of the charge carriers and the mobilities, refractive indices, electron energy spectrum, etc. As one newly arising study and application branch of epitaxy, Nano Selective Area Growth (SAG) is widely used to fabricate materials of different thicknesses and composition on different regions of a single wafer. All of these new and promising fields have caught the interests and attentions of all the researchers around the world.

Practically, GaN bulk material has been prepared by Metal Organic Vapor Phase Epitaxy (MOVPE) [2-4]. Due to the high lattice mismatch between the substrate and GaN epilayer, strain energy will accumulate in the material and eventually generate dislocations inside. In this work, Nano Selective Area Growth (NSAG) of GaN-based materials is performed in the MOVPE T-shape reactor. First, a SiO_2 dielectric mask with a thickness of 140 nm is deposited on a <0001>-oriented GaN/Al_2O_3 template using

chemical vapour deposition. Electron-beam lithography and reactive ion etching are then used to pattern the SiO_2 mask on the template.

Figure 1 shows a scanning electron microscopy (SEM) micrograph of the porous mask prepared in this work. The nano-openings are 80 nm in diameter. The nano-openings act as the nucleation sites for the subsequent growth of the GaN nanorod.

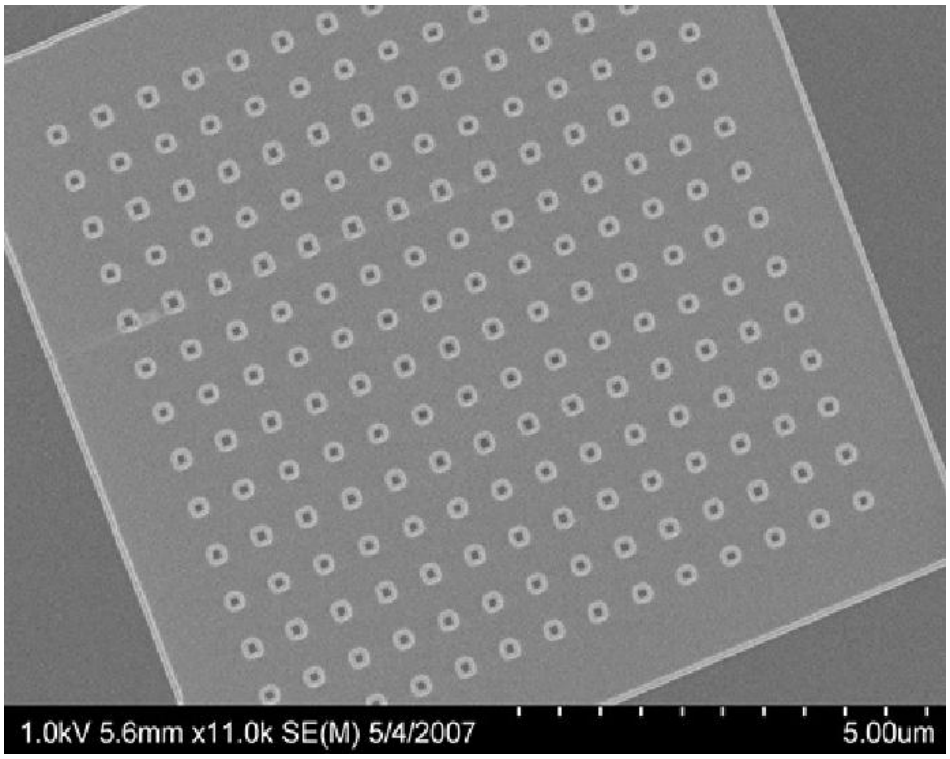

Figure 1. Porous mask for growing GaN nanorods

The MOVPE growth conditions are as follows:

• Temperature: 1000 ℃

• Pressure: 1.33 kPa (100 Torr)

• V/III ratio: 4500

• Growth rate: <1 μm/h

• Carrier gas: Nitrogen

• Precursor: TMGa and NH_3

The growth rate is kept relatively low in order to obtain a high crystal quality and a perfect selectivity. The growth starts with NSAG of GaN at 1000 ℃ until the faceted pyramids are obtained. The surface morphology of the faceted nanostructures is first characterized by scanning electron microscopy (Figure 2). It can be seen that perfectly selective growth is obtained and the nanorods are completely confined in the opening of the mask.

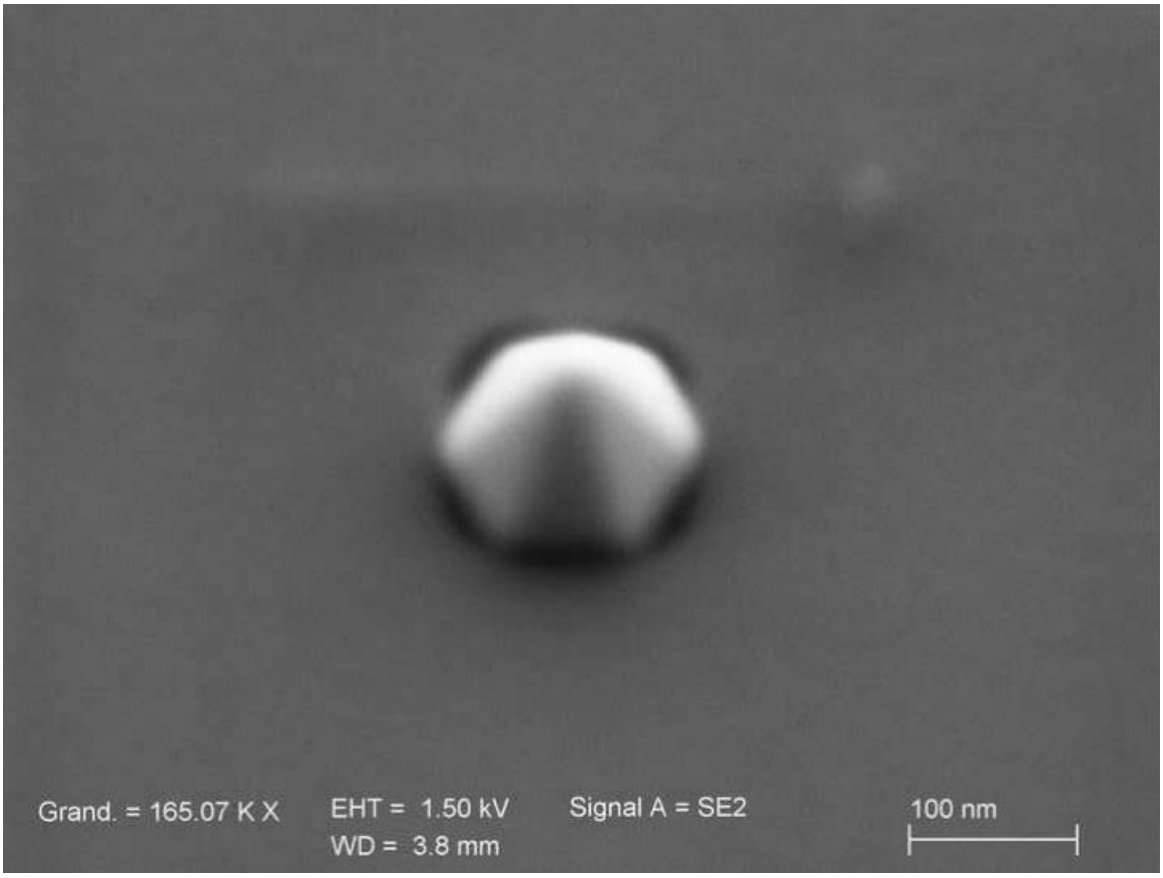

Figure 2. SEM image of a hexagonal GaN nano-pyramid grown by NSAG

Atomic force microscopy (AFM) is also performed as shown in Figure 3. Nanorods are with very smooth surface morphology and homogeneous in both width and height dimensions. Several patterns have been characterized, and the heights of the nanorods measured are between 70 to 100 nm. It can be seen again that the growth is perfectly selective, which confirms the result in the SEM image.

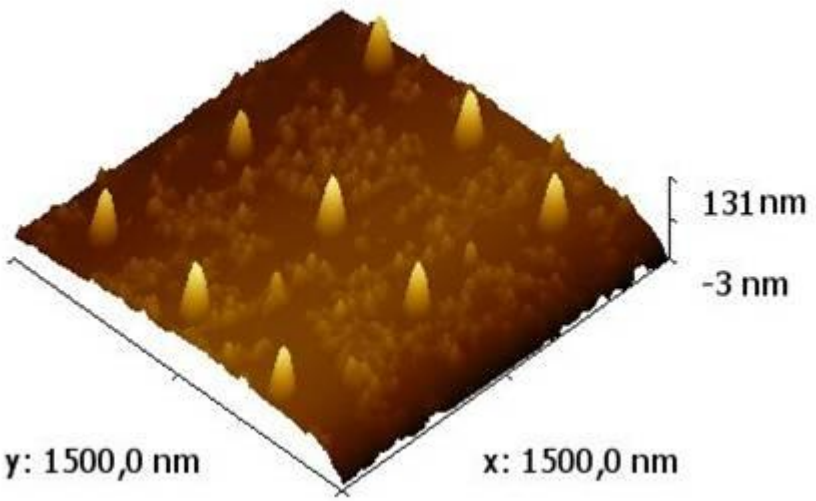

Figure 3. AFM image of GaN nanorods

To study the internal structural properties, GaN nanorods are cut on the (1-100) plane by focused ion beam and then characterized by the transmission electron microscopy (TEM). In Figure 4, threading dislocations have been observed in the base part of some GaN nanorods but the top cap region is dislocation-free.

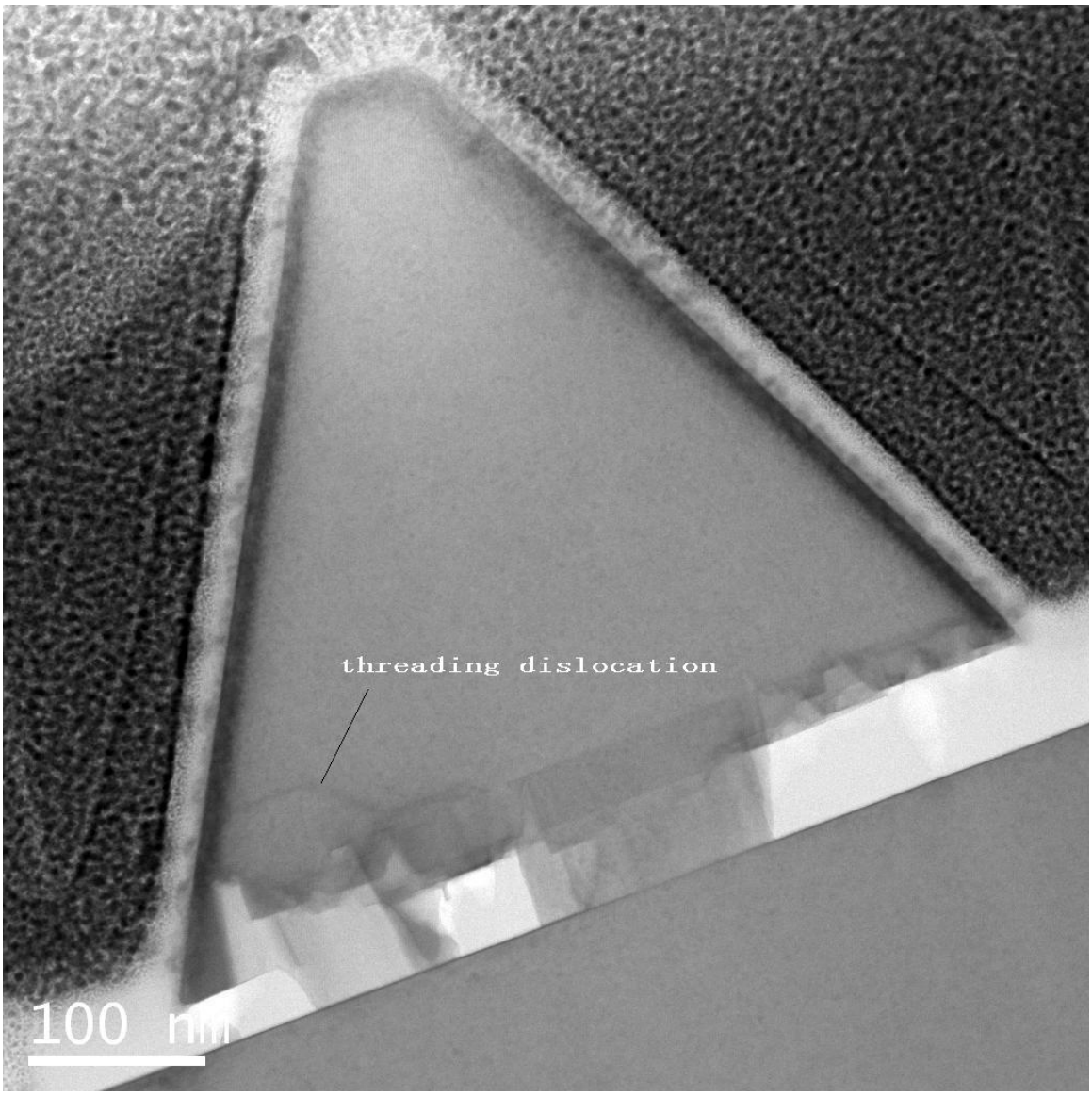

Figure 4. Cross-sectional TEM image of GaN nanorod

Dislocations in solids play an important role in determining the mechanical and electronic properties of materials [5-11], due to the fact that the atoms of the dislocations have different bonding and environment from the other atoms buried in the bulk. This PhD work will investigate the mechanism of dislocation dissipation with anisotropic material properties in GaN nanorods, with the consideration of length scale effect which

is due to the surface effect at nano-scale. The objective is to find out the optimized ranges of geometrical parameters of GaN nanorods with no dislocations. This could be adapted in nanostructure design and provide guidance for the fabrication of dislocation-free nanostructures.

Literature Reviews

During the epitaxy process, the epilayer will be strained due to the lattice mismatch between the substrate and the epilayer itself. As the epilayer grows, elastic strain energy is accumulating in the material and the atoms of the structure will accommodate to decrease the strain energy. The accommodation of atoms is more effective where the atoms encounter any free surfaces because the surfaces provide more degrees of freedom for the relaxation of atoms. In case that the elastic strain energy becomes too large and the accommodation of atoms is insufficient, the nanostructures will undergo a plastic deformation and then defects, such as dislocations, will be introduced into the material.

S. Luryi and E. Suhir [6] pioneered quantitatively to analyze the lattice-mismatched system and determined the threshold strain energy of generating dislocations by approximating the lateral stress with an exponential distribution. Based on their work, D. Zubia and S. D. Hersee [12] refined the analysis by considering the compliance of the substrate. However, these publications obtained the analytical results basing on their approximations of the stress or strain fields. Kröner [13] mathematically described the elastic field with defects in solids, which led to solving the stress field by taking the dislocation induced strain as eigenstrain. Z. Liang et al. [14, 15] numerically implemented this eigenstrain method by finite element framework and calculated the image force on GaN dislocations of nanorods for free surfaces although.

When the dislocation is embedded in nanostructures with dimensions on the order of tens of nanometers, the behavior of the dislocation becomes highly sensitive to the

surrounding environment because the atoms near the dislocation will interact more actively in such extremely small domain. Generally, external loads, grain boundaries, inclusions and surfaces/interfaces, etc. will affect the behavior of the dislocation. This influence might be crucial in determining the way that the dislocation behaves in nanostructures, thus it should be taken into consideration in comprehensive studies.

Relationship of the deformation-dependent surface energy with the surface stress was first described by the Shuttleworth's equation [16]. Gurtin et al. [17, 18] linked the surface stress to the bulk stress at the vicinity of the surface by regarding the surface as a negligibly thin object adhering to the underlying material without slipping. Fang et al. [19-22] combined the surface stress model with complex variable method to solve the stress fields for a screw or edge dislocation located in materials of a circular nanowire embedded in an infinite matrix. Luo and Xiao [23] extended this analysis to the case of an elliptical nanowire embedded in an infinite matrix with conformal mappings. Recently, Ahmadzadeh-Bakhshayesh et al. [24] adopted the same method to analyze the surface/interface effect on elastic behavior of a screw dislocation in an eccentric core–shell nanowire. However, these results based on the complex variable method provide the stress fields as infinite power series, which are difficult to manipulate in further situations. The influences of the size parameter and surface elasticity are also hard to interpret clearly. Beside this limitation, their solutions by using the complex variable method are limited to Airy's stress functions which are only capable to deal with 2D elastic plane stress or strain problems and mainly used for isotropic materials.

Dissertation Objectives and Goals

This work starts from the understandings of the mechanism of dislocation dissipation in solids. In classical continuum mechanics, J. P. Hirth and J. Lothe [25] shows that for a dislocation embedded in a semi-infinite solid, a fictitious image

dislocation has to be imposed in the mirror position to maintain the stress-free surface boundary condition, which leads to the "image force" exerted on the dislocation. The image force on the dislocation is the driving force to move the dislocation. When its magnitude is large enough to overcome the lattice resistance, the dislocation will be driven towards the free surfaces. According to the kinetic rule of dislocation dynamics [26], this driving force will increase itself as the dislocation moves until it's dissipated out of the solid. Therefore, this work implements a screw dislocation in solids with free surfaces by a novel finite element model, and then image forces of dislocations embedded in various shaped GaN nanorods are calculated. By comparing with critical force to overcome the lattice resistance, it will demonstrate the mechanism of dislocation dissipation in GaN nanorods.

The analysis through finite element modeling provides a straightforward illustration of the dislocation dissipation by the image force, but it is limited to numerical results that are not flexible to handle for various applications. Moreover, to understand deeply the interaction between the dislocation and surfaces in a physical and mechanical sense, systematic studies are needed in an analytical way. This work will follow the concept of eigenstrain for the dislocation and use Green's function to formulate the strain or stress field. It will also take into account the surface effect to complete an analytical framework for a general 3D domain of defected material with elastic anisotropy.

As a start point, this work has obtained the close-form solutions to the stress fields of an infinite isotropic nanowire. It helps to consolidate the current analytical framework. The work will be followed by extending isotropic materials to anisotropic materials (e.g., wurzite GaN). This can be implemented by plugging the corresponding anisotropic tensors into the formulation. On the other hand, the proposed analytical framework should have the flexibility to take 3D structures of solids, which could be adjusted to fit into various situations (finite cylinders, nanodots with a cap, etc). The ultimate target is to provide a promising solution to the analysis and design of general anisotropic materials

with 3D shapes. In this way, the framework of this work could be applied to multi-scale studies of materials and bridge up other models developed for different dimensional scales of solids.

CHAPTER 2

INVESTIGATION OF DISLOCATION DISSIPATION MECHANISM

This chapter presents the theory of dislocation dissipation mechanism. It basically focuses on the concept of "Image Force" to provide an explanation of how the dislocation is driven towards surfaces. In this chapter, we will also summarize the two main methods used to calculate the image force, and by comparing their pros and cons, we can decide which approach should be used in our work.

Definition of Image Force

The concept of "Image Force" originates from the requirement of enforcing the stress-free surface boundary condition when a dislocation is embedded in a semi-infinite solid[25, 26]. In this case, a fictitious image dislocation needs to be imposed with the same magnitude but opposite direction of the Burgers vector (Figure 5). The image dislocation is not real but there is indeed a force acted on the dislocation. Generally speaking, the dislocation is prone to be attracted to a compliant ("soft") surface and repelled from a rigid one conversely.

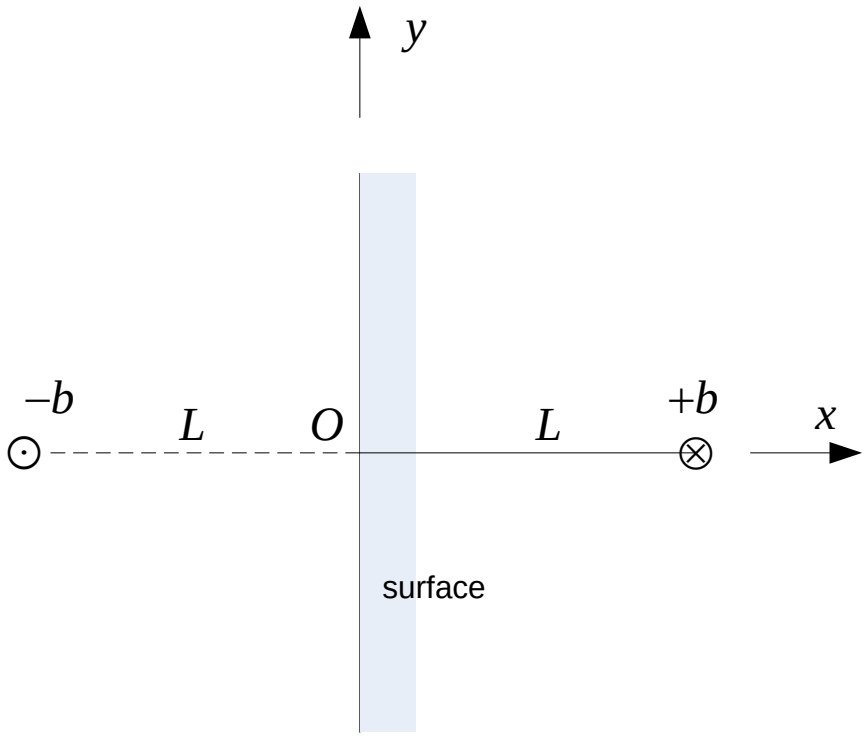

Figure 5. A screw dislocation and its "image" in the space

For a simple case in Figure 5, the image force could be easily determined from the stress field. First, it is already known that the stress field of a screw dislocation at the coordinate origin of an infinite media is:

$$\sigma_{xz} = -\frac{\mu b}{2\pi}\frac{y}{x^2+y^2}, \tag{1}$$

$$\sigma_{yz} = \frac{\mu b}{2\pi}\frac{x}{x^2+y^2}, \tag{2}$$

where μ is the shear modulus of the solid and b is the magnitude of the screw dislocation.

Now the media becomes semi-infinite, which introduces a free surface to the space at $x = 0$. It is obvious that the stress field in Eqs. (1) and (2) violates the free

surface boundary condition, and it must be modified by adding the stress contribution from the image dislocation:

$$\sigma_{xz} = -\frac{\mu b}{2\pi}\frac{y}{(x-L)^2+y^2} + \frac{\mu b}{2\pi}\frac{y}{(x+L)^2+y^2}, \tag{3}$$

$$\sigma_{yz} = \frac{\mu b}{2\pi}\frac{x-L}{(x-L)^2+y^2} - \frac{\mu b}{2\pi}\frac{x+L}{(x+L)^2+y^2}, \tag{4}$$

where L is the distance of the dislocation away from the free surface.

The two parallel dislocations, i.e., the real screw dislocation and its image, will interact with each other, and thus the image force (per unit length) acted on the screw dislocation is calculated as[26]:

$$f = \sigma_{yz} b. \tag{5}$$

From Eqs. (4) and (5), the image force per unit length on the screw dislocation by the free surface is evaluated at $x = L, y = 0$:

$$f = -\frac{\mu b^2}{4\pi L}. \tag{6}$$

Interestingly, this image force is incidentally the same with the solo force due to the image dislocation located at $x = -L$. This might be the reason that the force is called "Image Force" thereafter.

Calculation of Image Force

The calculation of image force in Figure 5 is easy and straightforward because of the simple geometry of the solid and the configuration of the dislocation. For finite systems, the shape of the solid could be arbitrary and even a general curved dislocation needs to be taken into consideration. All these factors could complicate the analysis of the image force a lot. However, there are mainly two approaches that could handle such general problems: the nonlocal method and energy method.

Nonlocal method

In nonlocal method, one can calculate the image force along the dislocation line using the Peach-Koehler equation [25]:

$$\vec{f} = (\sigma^{NL} \bullet \vec{b}) \times \vec{\xi}, \tag{7}$$

where $\vec{f}$ is the image force density vector along the dislocation line, σ^{NL} is the nonlocal stress exerted on the dislocation, and $\vec{\xi}$ is the unit vector along the direction of the dislocation line.

The nonlocal stress requires a volumetric integration of the stress tensor over the whole crystal space [27]:

$$\sigma^{NL}(\vec{x}) = \int_V \kappa(\vec{x} - \vec{x}')\sigma(\vec{x}')dV' \tag{8}$$

where $\kappa(\vec{x} - \vec{x}')$ is a correlation kernel that links the local point ($\vec{x}$) on the dislocation line to the nonlocal point ($\vec{x}'$) in the rest crystal space.

The nonlocal stress σ^{NL} should be the sum of the contribution from all other portions of the crystal to the dislocation, which accounts for the long range effects from the free surfaces. Usually a volumetric integration over the whole crystal space should be calculated for σ^{NL}.

In the case of Figure 5, since the image dislocation could be easily determined for such simple configurations, the nonlocal stress is naturally the only contribution from this image dislocation. In fact, the nonlocal stress field can be also viewed as the equivalent part of the difference of the total stress field minus the original stress field of the same dislocation in the infinite media without the surface. Therefore, the nonlocal stress field can be determined from Eqs. (3) and (4) as:

$$\sigma_{xz}^{NL} = \frac{\mu b}{2\pi} \frac{y}{(x+L)^2 + y^2}, \tag{9}$$

$$\sigma_{yz}^{NL} = -\frac{\mu b}{2\pi} \frac{x+L}{(x+L)^2 + y^2}, \tag{10}$$

The image force can be derived from Eq. (7) directly and it is the same with Eq. (5), which gives the final result of the image force in Eq. (6). As we can see in Eq. (5), the image force only consists f_x part, and f_y part happens to be zero in this case.

Energy method

The energy method is based on the virtual work principle. In mechanics, a general force is defined as the change of the total energy relative to a general configuration coordinate change:

$$f = -\frac{\partial W}{\partial a}, \tag{11}$$

where ∂a can be seen as the change of the dislocation position in this case, and the total energy W should be the total energy stored in the solid.

A more general definition is given in thermodynamics, with the free energy taking place of the mechanical energy here, and with parameters such as composition put on equal footing with the coordinate change. The coordinates of a system tend to change spontaneously to lower its total free energy. In this sense, forces on dislocations are virtual forces representing the change in the free energy of the system with displacement of the dislocation. Physically, the elastic force is in fact distributed throughout the elastically strained material rather than acting directly on the dislocation line.

For the present, we only discuss about purely elastic and mechanical effects, and we also exclude the influence of any potential energy due to external forces, such as the gravity or electro-magnetic field, etc. The total energy per unit length of a screw dislocation parallel to a free surface with an offset of L from the surface (Figure 5) can be determined from the classical elasticity theory[25]:

$$W = \frac{\mu b^2}{4\pi} \ln(\frac{L}{r_0}) \tag{12}$$

where r_0 is the core radius of the dislocation.

Note here that the energy will diverge as the core radius of the dislocation tends to zero, which arises from the inadequacy of linear elasticity theory to deal with the severe lattice distortion near the core of the dislocation. To be accurate, the total energy should also cover the dislocation core energy as an extra term in Eq. (12). However, according to atomistic simulations[28], the dislocation core energy could be considered as a constant and restricted to a rather small region of the size of $r_0 \sim b$. Furthermore, by combining Eqs. (11) and (12), we can see the image force has no relation to the dislocation core

energy and the parameter of r_0 has also disappeared. In the end, we can obtain again the same result of the image force in Eq. (6).

CHAPTER 3

DISLOCATION DISSIPATION BY FREE SURFACES

This chapter introduces a finite element model of implementing a screw dislocation in solids with only free surfaces, which facilitate the specification of the surface boundary condition. The stress field obtained from finite element analysis is then used to calculate the image force of the dislocation. Through this numerical model, image forces of a screw dislocation embedded in various shaped GaN nanorods are calculated. By comparing with critical force to overcome the lattice resistance, this work will demonstrate the mechanism of dislocation dissipation in GaN nanorods.

Finite Element Modeling of Dislocations in Solids

In a 3D Cartesian coordinate system, a single screw dislocation is embedded in a finite solid along $\vec{\xi} = [0, 0, 1]$ direction with Burgers vector $\vec{b} = [0, 0, b]$. The dislocation induces two nonzero plastic strain components, which can be considered as eigenstrains [29]:

$$\varepsilon_{yz}^{*} = \varepsilon_{zy}^{*} = \frac{1}{2} b\delta(y)H(x), \tag{13}$$

where $\delta(y)$ is the Dirac's delta function and $H(x)$ is the Heaviside function.

The constitutive relationship between the stress tensor, σ_{ij} and the total strain tensor ε_{kl}^{T} is described as [30]:

$$\sigma_{ij} = C_{ijkl}(\varepsilon_{kl}^{T} - \varepsilon_{kl}^{*}), \tag{14}$$

where C_{ijkl} is the stiffness tensor of the material.

From the classical continuum mechanics theory, the mechanical equilibrium of the solid is achieved by [31]:

$$\sigma_{ij,j} = 0. \tag{15}$$

From Eqs. (13) - (15), the general stress field of the solid can be obtained as [30]:

$$\sigma_{ij}(\vec{r}) = C_{ijkl}\int_{-\infty}^{\infty} C_{pqmn}(G_{kp,qn}(\vec{r}-\vec{r}\,')\varepsilon_{ml}^{*} - G_{kp,ql}(\vec{r}-\vec{r}\,')\varepsilon_{mn}^{*})d\vec{r}\,', \tag{16}$$

where $\vec{r}$ is the space vector measured from the origin to the point of interest, and $G(\vec{r}-\vec{r}\,')$ is the Green's function and the integration factor is $\vec{r}\,'$.

In addition to these equations, the boundary conditions need to be included. A simple classical formulation of free surface condition is described as [31]:

$$\sigma_{ij}n_j = 0, \tag{17}$$

where $\vec{n}$ is the unit vector normal to the surface.

Eq. (17) is used in the work of Z. Liang et al. [14] and they have calculated the image forces of dislocations for nanostructures which have the lowest length dimension below 10 nm. However, when the size of the structure drops down to several nanometers, the traditional continuum mechanical definition of free surface in Eq. (17) is unable to capture the subtle behavior of the surface. The atoms from the surface have good flexibility to accommodate themselves and the relaxation is more effective than the atoms from the bulk of the structure. This important property of solid surface is the surface

stress [32] and it is proven to change the elastic behavior of the surface dramatically when the dimensions of structure features are below 10 nm [33-38]. A proper formulation of the surface stress in relation to the deformation dependent surface energy is described by the Shuttleworth's equation [16]:

$$\sigma_{\alpha\beta}^{S} = \gamma\delta_{\alpha\beta} + \frac{\partial\gamma}{\partial\varepsilon_{\alpha\beta}^{S}}, \tag{18}$$

where $\sigma_{\alpha\beta}^{S}$ is the surface stress tensor, $\varepsilon_{\alpha\beta}^{S}$ is the surface strain tensor and γ is the surface energy density which can be obtained from atomistic simulations.

Theoretical and numerical studies of the surface stress indicate that the surface stress can significantly alter the nature of interaction forms in nanostructures and the stress profile deviates largely from conventional result of Eq. (17) below 10 nm.

As a start point, the simple free surface boundary condition in Eq. (17) is implemented in the following finite element analysis. To obtain the stress field numerically, Eq. (14) has to be implemented for the material property but the Dirac's delta function is involved with an infinite value. To avoid the infinity of the Dirac's delta function, Z. Liang et al. [14] have mapped this dislocation eigenstrain into Hooke's Law and the mechanical equilibrium systems to obtain a similar form of Eq. (16), but it remains quite a difficult task to code such equations in finite element software like ABAQUS or ANSYS to incorporate the eigenstrain.

This work introduces an alternative method to model the screw dislocation to avoid the coding work. It is very easy to implement and quite fast for computation. In Figure 6, the screw dislocation introduces a slip plane with two adjacent moving surfaces. To mimic the same eigenstrain components in Eq.(13), the two adjacent surfaces are displaced $+b/2$ and $-b/2$ along opposite directions respectively. In the finite element

analysis, the displacements are applied as boundary conditions and they introduce a non-elastic strain that is the same as the eigenstrain in Eq. (13).

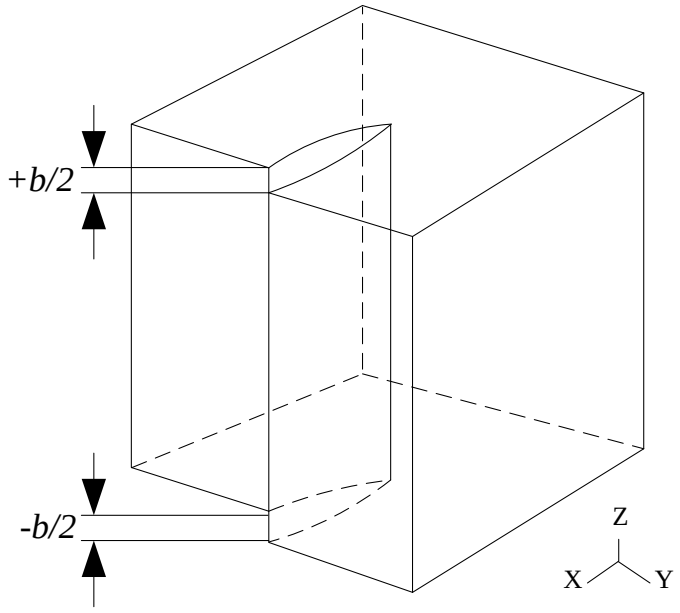

Figure 6. A screw dislocation embedded in the solid

To validate the stress result of this method, a simple cubic and isotropic solid is analyzed in ABAQUS with the material Lamé constants: λ = 141.2 GPa, μ = 116.5 GPa. The length of the cube is set to L = 200 nm and the magnitude of the Burgers vector is b = 0.1 nm to mimic a sufficiently large solid. The analytical stress field of an infinite solid has only two nonzero components as given in Eq. (1) and (2).

The shear stress component along a path centered in the cube has been plotted in Figure 7. The path starts from [0, -L/2, 0] and ends at [0, L/2, 0]. The stress profile from this finite element model agrees very well with the analytical solution.

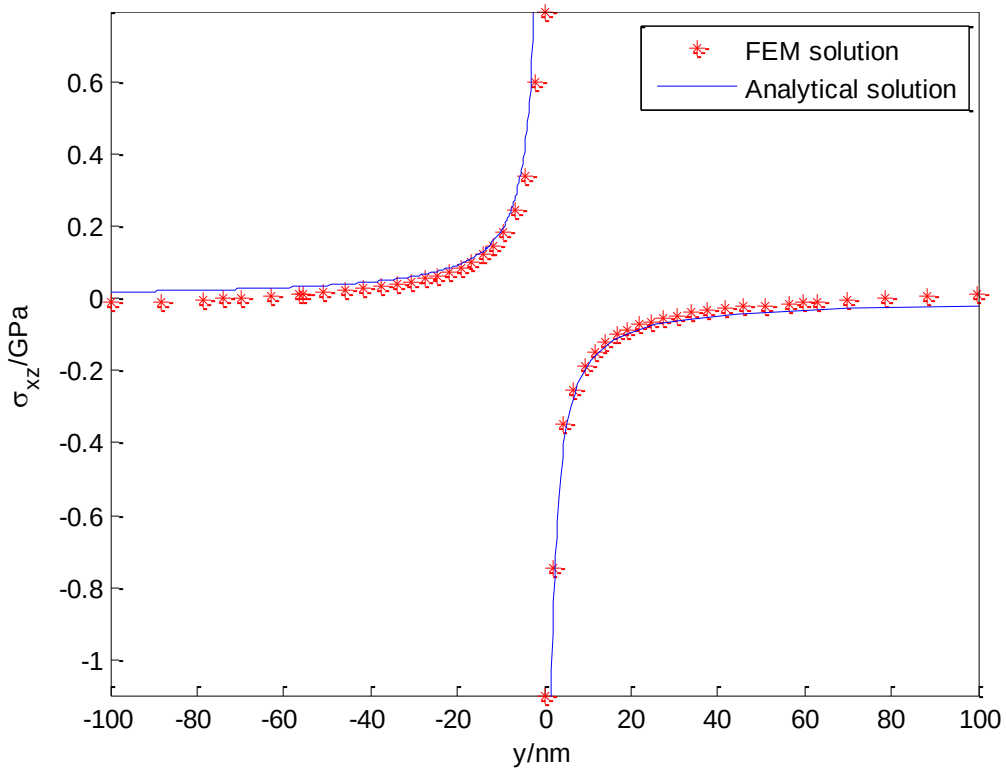

Figure 7. Shear stress along the path centered in the solid

The model of implementing the dislocation in this work is easy to implement since it requires no implementation of Eq. (14) or (16) through coding user material property in ABAQUS or ANSYS. In addition to that, when surface stress is required to be incorporated to refine the analysis of nanostructures, this model provides the good extending flexibility to deal with surface stress formulation like Eq. (18) alone. This work will apply this model to the analysis of the image forces on a screw dislocation and illustrate the dislocation dissipation mechanism of GaN nanostructures.

Application to GaN nanorods

This work considers four shapes of GaN nanorods: (i) cylinder; (ii) cylindrical base and conical cap; (iii) cylindrical base and pyramid cap; (iv) cylindrical base and top chopped pyramid cap (Figure 8). GaN nanorods of shape (iv) have not been investigated

so far in other literatures. Cylindrical nanorods of shape (i) are obtained when the growth of the MOVPE process is limited within the holes of the masks [39, 40]. After the growth fills the holes in the masks, overgrowth of GaN takes place on top of the cylindrical base. Nanorods of shape (iii) are obtained when the growth is finally terminated while some nanorods of shape (iv) can be obtained when the growth is terminated before the final stage [41-43]. In this work, nanorods of shape (ii) are also studied although it is not feasible to obtain from experiments, but it can be used to compare the stress profile with that of shape (iii). These two shapes have different surface features in the cap region and the comparison will illustrate the effect of surface stress on the nanostructures.

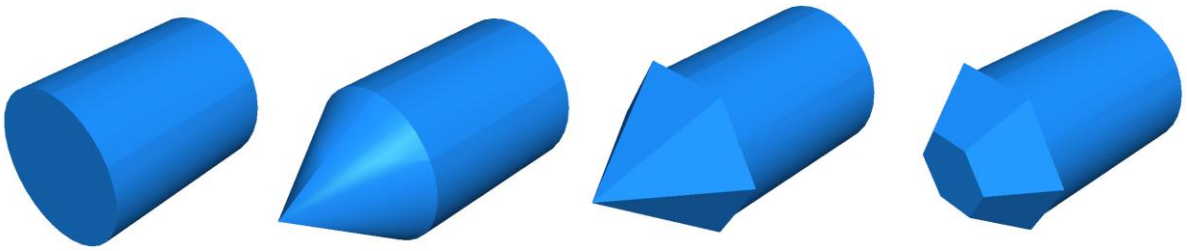

Figure 8. Four shapes of GaN nanorods studied in this work

The screw dislocation is set to be oriented along <0001> direction with a (11-20) slip plane according to the experimental data[15]. It is located off-center with an offset (δ) equal to one half of the radius of the cylindrical base (Figure 9).

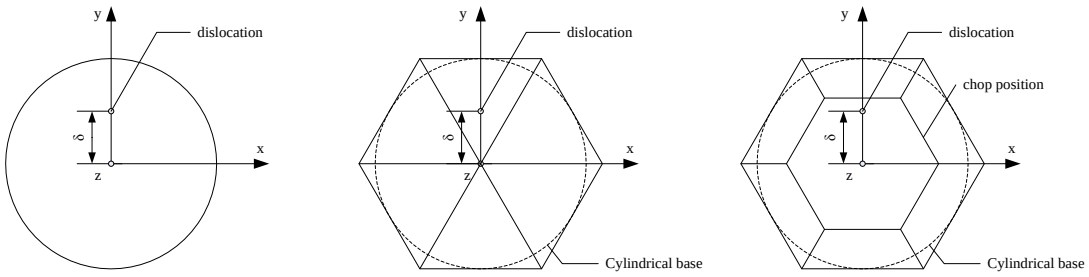

(a) (b) (c)

Figure 9. Schematic top view of the nanorods

(a) nanorod of shape (i) or (ii); (b) nanorod of shape (iii); (c) nanorod of shape (iv)

The geometrical parameters, the anisotropic material property of GaN and Burgers vector [44] are listed in Table 1 for shape (i-iii) in Figure 8. As for the shape (iv) with top chopped cap, the cap region height will vary from 0 nm to 60 nm.

Table 1. Parameters used in the finite element analysis of this work

Parameter	Value
Cylindrical base radius, r	40 nm
Cylindrical base height, h	100 nm
Full cap region height, d	60 nm
Dislocation offset, δ	20 nm
Elastic constant, C_{11}	390 GPa
Elastic constant, C_{12}	145 GPa
Elastic constant, C_{13}	106 GPa
Elastic constant, C_{33}	398 GPa
Elastic constant, C_{44}	105 GPa
Burgers vector's magnitude, b	0.518 nm

The simulation domain has been meshed non-uniformly with denser elements near the dislocation line (Figure 10). A typical simulation in this case contains the number of linear tetrahedral elements on the order of 10^5, and it only takes around 5 minutes for one simulation on a computer with 2.0 GHz Intel CPU and 2.0 GB RAM.

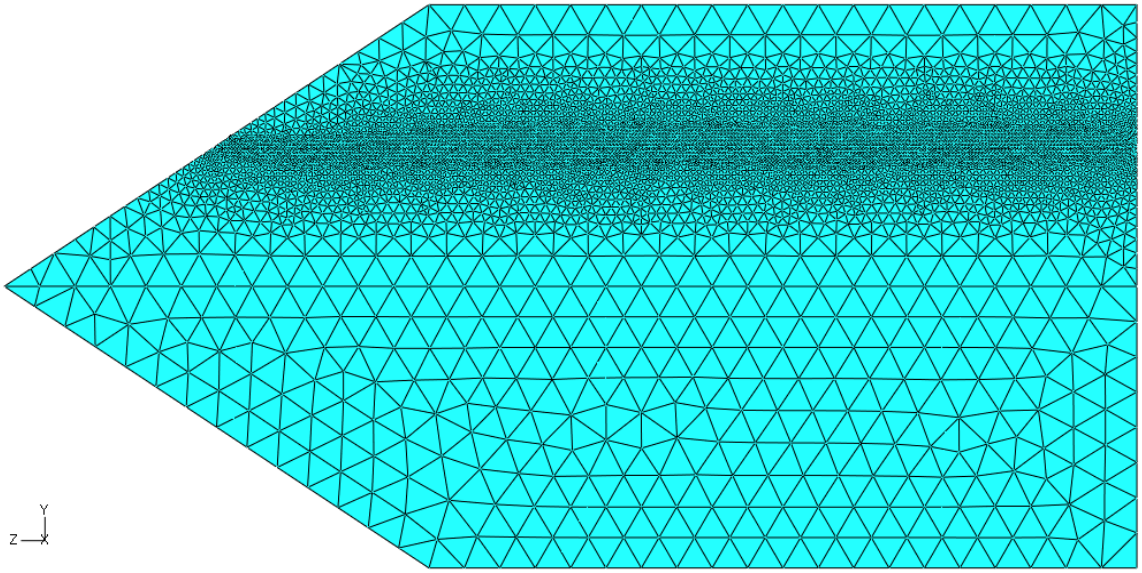

Figure 10. Cut view of the meshed elements of nanorod with a conical/pyramid cap

The complete stress field has been computed in ABAQUS, and the image force along the dislocation line can be obtained in Eq. (7). The nonlocal stress σ^{NL} should be the sum of the contribution from all other portions of the crystal to the dislocation, which accounts for the long range effects from the free surfaces. Usually a volumetric integration over the whole crystal space should be calculated for σ^{NL}. However, for a screw dislocation oriented in <0001> direction and wurzite anisotropic GaN, the stress field is symmetric with respect to *y*-*z* plane, so it can be reduced to a linear integration [14]:

$$\sigma_{ij}^{NL}(0,\delta,z)=\frac{\int_{y_{\min}(z)}^{y_{\max}(z)}\sigma_{ij}(0,y,z)dy}{y_{\max}(z)-y_{\min}(z)}, \tag{19}$$

where y_{min} and y_{max} are the minimum and maximum of the y-coordinates in the domain.

The calculation of this nonlocal stress by Z. Liang et al. [14] requires two equivalent simulations for two complementary integrating paths. This work only needs one simulation and the integration form is a little different from equation (10) in their work [14]:

$$\sigma_{ij}^{NL}(0,\delta,z)=\frac{\int_{y_{\min}(z)}^{\delta}\sigma_{ij}(0,y,z)dy}{\delta-y_{\min}(z)}+\frac{\int_{\delta}^{y_{\max}(z)}\sigma_{ij}(0,y,z)dy}{y_{\max}(z)-\delta}. \tag{20}$$

Note that for <0001>-oriented screw dislocation, Eq. (7) can be further simplified as:

$$f=b\sqrt{(\sigma_{13}^{NL})^2+(\sigma_{23}^{NL})^2}, \tag{21}$$

where σ_{13}^{NL} and σ_{23}^{NL} are the shear components of the nonlocal stress, which can be calculated from Eq. (20).

When the calculated image force is larger than the critical force, which is 0.5N/m estimated for <0001>-oriented screw dislocation embedded in GaN crystal [14], it will drive the dislocation toward the free surface, which in turn increases the image force itself and finally dissipates the dislocation out of the crystal according to dislocation dynamics [25, 26].

Results

Figure 11 shows the image force exerted on the dislocation for GaN cylindrical nanorod and the critical force as a dashed horizontal line. This result agrees well with the solution of Z. Liang et al. [14] who obtained the result by implementing the dislocation through coding user material property. The image force starts from zero and increases along the height of the cylindrical nanorod. The magnitude stays at approximately 0.4N/m for the most part of the cylinder between 20nm and 80nm along the height. Since this region is far from the bottom and top surfaces, the lateral free surface can be considered as the only contribution to the image force for this region, while the region at two ends can be affected by both the lateral surface and the bottom or top surfaces. The image force decreases after the height of 80nm and it is symmetric with the result before 20nm because the two ends of the cylinder are symmetric. For GaN cylindrical nanorod with the geometry provided in Table 1, the magnitude of image force is less than the critical force, so the dislocation can't be driven out and is confined inside the cylinder.

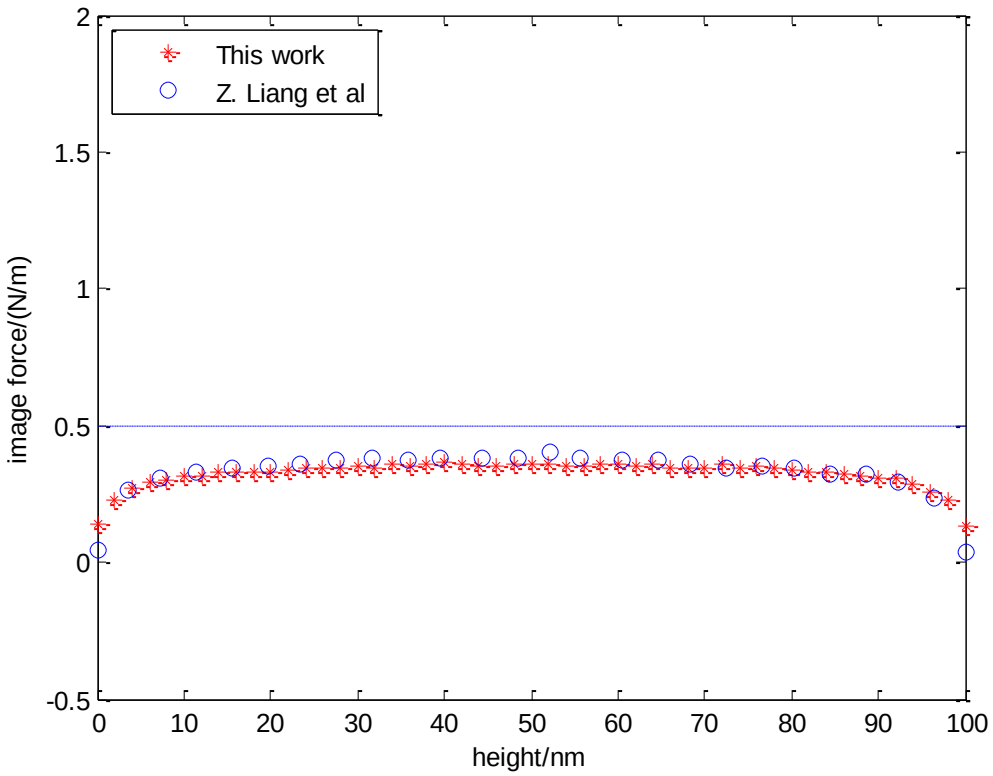

Figure 11. Image force exerted on the dislocation for GaN cylindrical nanorod

Figure 12 shows the image force of GaN nanorod with a cylindrical base and a pyramid cap. Note that the height of the pyramid cap in the work of Z. Liang et al. [14] is a little different from this work because they specified the pyramid shape by the six faceted planes but didn't show the value of height explicitly in their plots. The overall tendencies of the two results are similar and both demonstrate the dissipation of the dislocation in the cap region. In the lower cylindrical region the image force behaves similarly as the case of GaN cylindrical nanorod. It starts pinned at the bottom, increases along the height, and keeps on the same magnitude of approximately 0.4N/m in the whole cylindrical base. When the dislocation enters the cap region from 100nm along the height, the magnitude of the image force increases largely because the dislocation gets closer to the surrounding free surfaces of the six slanted pyramid facets. However, the

magnitude of the image force exceeds the critical force only when the dislocation enters the deeper region of the cap, which is about 110nm measured from the bottom face of the nanorod. The image force keeps increasing dramatically along the height of the cap until the dislocation ends at the facet of the pyramid. Comparing its magnitude with the critical force, the dislocation experiences a force large enough to dissipate itself toward the free surfaces after the height of 110nm. From Figure 12, the magnitude of the image force in the region of the pyramid cap is much greater than that of the cylindrical base. This indicates that the contribution from the free surfaces affects the behavior of the dislocation significantly, and dislocation-free material can be obtained in the cap domain of the nanorod.

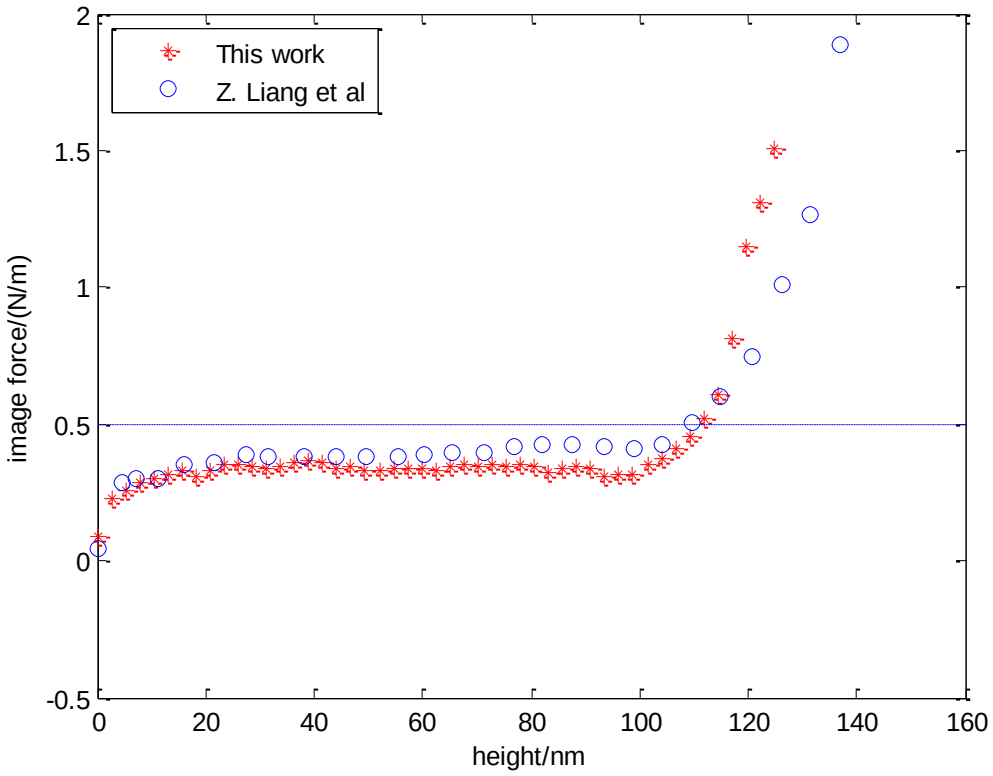

Figure 12. Image force exerted on the dislocation for GaN nanorod with a cylindrical base and a pyramid cap

This work also investigates the dislocation behavior of top chopped GaN nanorods, which have not been investigated for dislocation dissipations so far in other literatures. The cap is chopped incrementally along the height for different nanorods. In Figure 13, the chop position is measured from the top of the cylindrical base and the cap region height is respectively set as 0 nm (same as cylindrical nanorod of shape (i) in Figure 8); 15nm; 30 nm; 45 nm and 60 nm (same as shape (iii) in Figure 8).The rest parameters of the simulation are the same as those in Table 1.

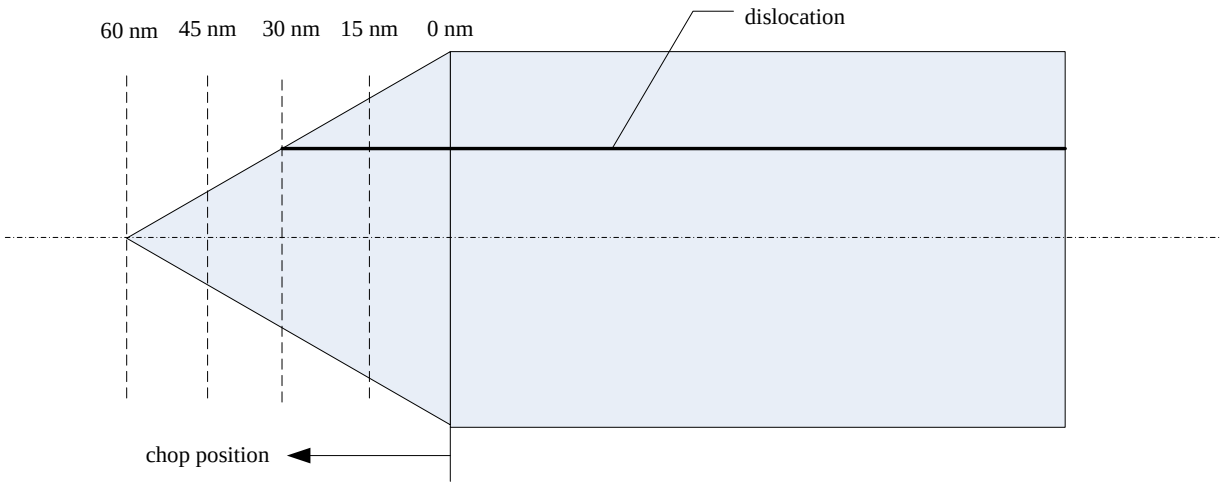

Figure 13. Different chop positions of GaN nanorod with a pyramid cap

Figure 14 shows the image forces exerted on the dislocation for GaN nanorods with a cylindrical base and different top chopped pyramid caps. Because the cylindrical base part is the same for all the nanorods, the image forces almost overlap from 0 nm to 80 nm along the height. The nanorod with chop position of 15 nm has the image force increasing a little when the dislocation enters the cap region, but the force drops down quickly as the dislocation approaches the chopped surface. Since the dislocation is

exposed to the free surface on the end of the chopped cap region, it is enclosed by the lateral and top free surfaces of a chopped flat plateau. This surface surrounding environment is similar to the end of a cylindrical nanorod (chop position of 0 nm), so the image force with chop position of 15 nm is similar with that of the cylindrical nanorod. However, due to the size shrinking of the cap region, the image force of the nanorod with chop position of 15 nm ends with a higher magnitude than that of the cylindrical nanorod.

The image force profile of the nanorod with chop position of 30 nm is similar to that in Figure 12 as its magnitude increases largely after the dislocation enters the cap region. This nanorod is quite special because the dislocation ends exactly at the chop position, which means the dislocation intercepts with the intersection of the top surface and the pyramid lateral surface. In this situation, the final magnitude of the image force at the chop position should be infinite as it can be seen from the nonlocal stress calculation in Eq. (20), where the denominator of the second term becomes zero at the point of the chop position. The overall image forces of nanorods with chop position of 30nm, 45 nm and 60 nm (full cap shape) are similar since their dislocations are all fully buried inside the structures, and the image forces are only computed on the dislocation line. The difference is seen from the final magnitude of the image force at the end of the dislocation line. The force of the nanorod with chop position of 30 nm should be the largest although it is not plotted as the magnitude is infinite, while the force of the nanorod with chop position of 45 nm is larger than that with chop position of 60 nm. This is determined by the surrounding surface environment at the end of the dislocation line, as the chopped cap has an extra flat top surface that gets the end of the dislocation closer to the free surface.

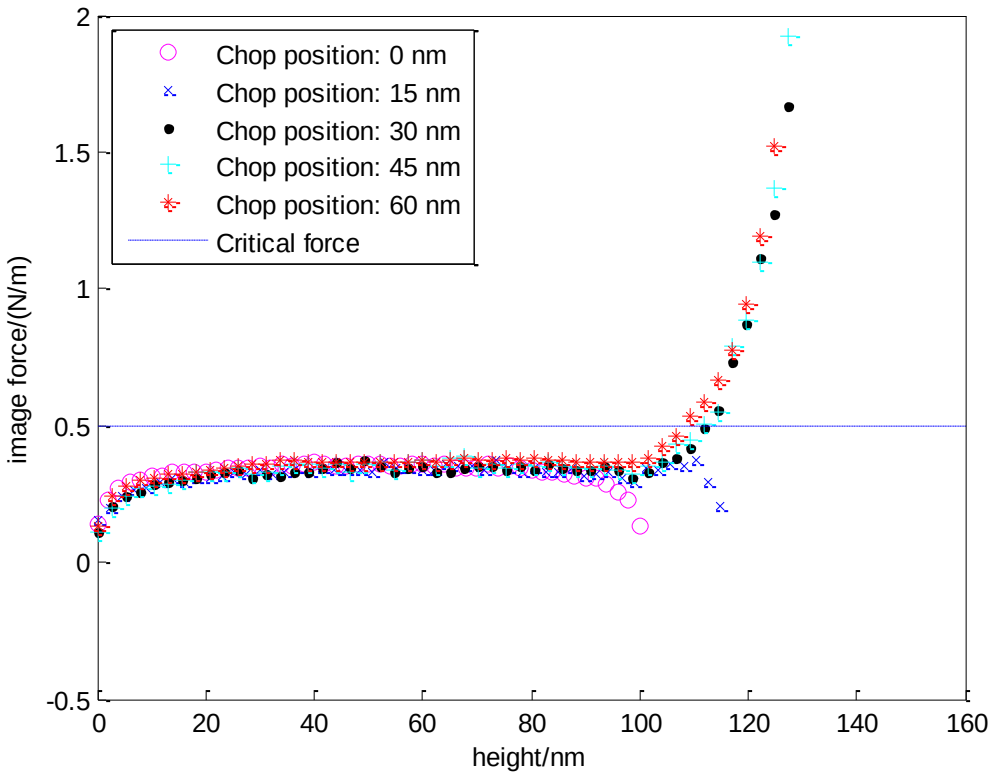

Figure 14. Image force exerted on the dislocation for GaN nanorod with a cylindrical base and different top chopped pyramid caps

Discussions

In addition to the nanorod with a pyramid cap, the nanorod with a conical cap is also studied in this work to illustrate the effect of surface stress to the image force in the cap region. Both nanorods have the same cylindrical base and their cap region heights are also the same (see Table 1). Figure 15 shows that both of them are expected to dissipate the dislocation towards the free surfaces after 110nm of the height where the image forces exceed the critical force.

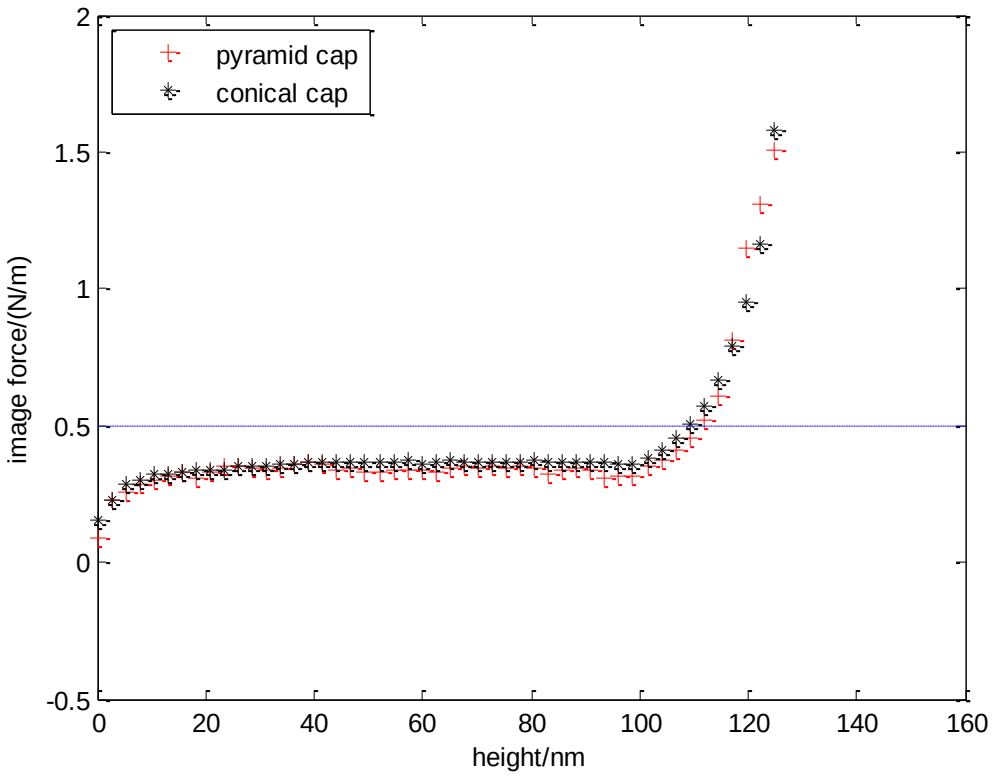

Figure 15. Image force exerted on the dislocation for GaN nanorod with a cylindrical base and a conical/pyramid cap

However, the image forces in these two nanorods have almost the same magnitude in the cap region. This means the contribution from the smooth lateral surface of the conical cap to the image force has no apparent difference from the six planar surfaces of the pyramid cap. Controversially, these two kinds of surfaces have quite different curvatures and especially, the pyramid cap has sharp edges where two planar facets intersect each other, so the image forces in these two kinds of caps should be expected to be different. In Eq. (21), the magnitude of the image force is demonstrated to be determined by the stress component σ_{13} and σ_{23}. These two stress components of GaN nanorods with cylindrical base and pyramid/conical cap are shown in Figure 16. In both geometries, the stress near the vicinity of the surface is almost the same as that of a rather

thick region away from the surface. This indicates the surface effect formulation in Eq. (17) used by this work and Z. Liang et al. [14] fails to capture the geometrical differences of the GaN nanorods. This formulation is used for classical surface macroscopically but it is inappropriate in the analysis of such nanostructures.

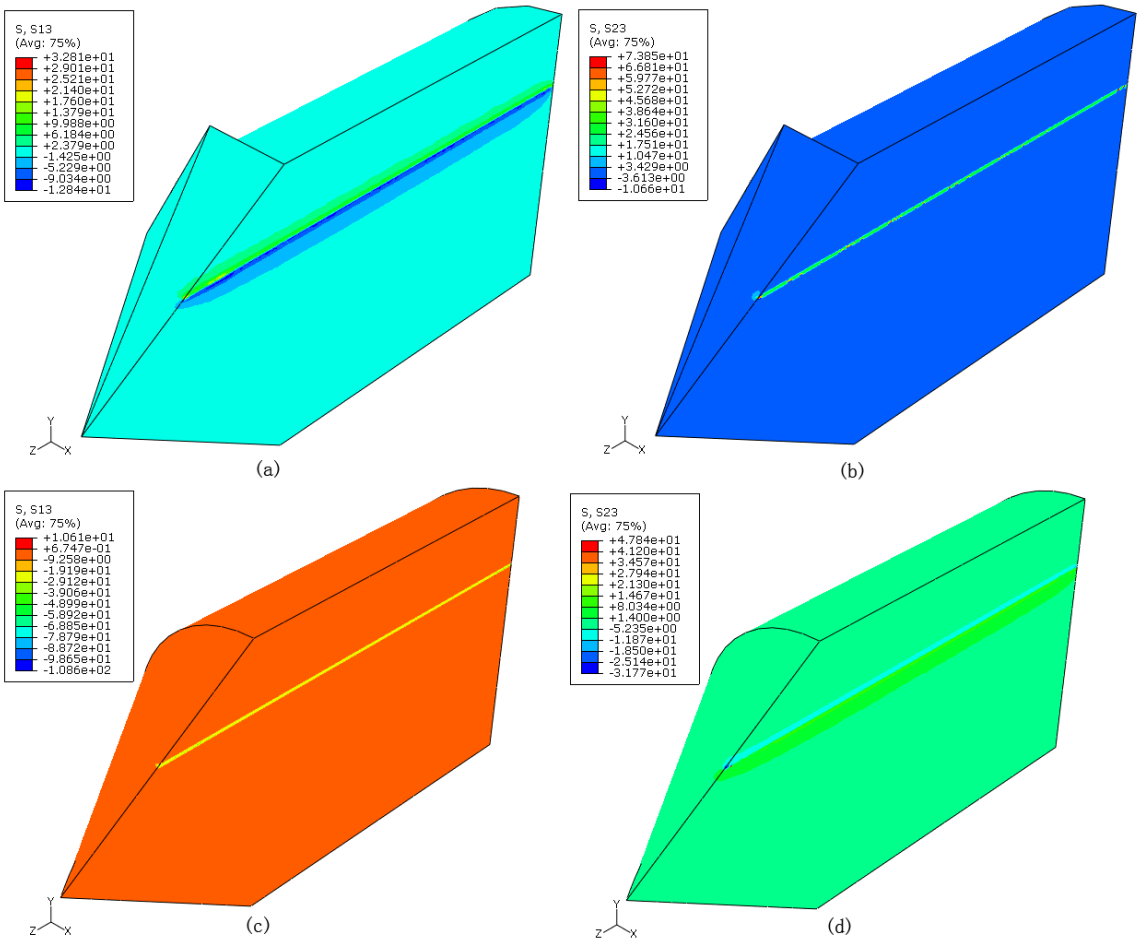

Figure 16. Stress component of GaN nanorods (cut view) with cylindrical base and pyramid/conical cap ((a) σ_{13} for pyramid cap; (b) σ_{23} for pyramid cap; (c) σ_{13} for conical cap; (d) σ_{23} for conical cap)

In typical nanostructures such as nanorods, nanowires or nanofilms, the size is usually on the level of tens of nanometers, which leads to a high sensitivity of the surface effect on stress distributions. In this case, a refined surface effect formulation should be used. Eq. (18) demonstrates that the surface stress is related to the deformation dependent surface energy, which means the surface stress could be a linear or nonlinear strain-dependent quantity. This formulation of surface effect as the surface stress could be adopted in the future work to refine the calculation of the stress field. G. Wei et al. [45] implemented a finite element framework which accounts for surface elasticity from the potential energy functional to describe the size dependence of the mechanical properties in nanosystems. Its validity has been verified from the stress concentration at a nanovoid and has then been applied to the investigation of surface effects in the interaction between nanovoids and the effective moduli in nanoporous materials. L. Tian and R. Rajapakse [34] also adopted a surface stress model to analyze nanoscale inhomogeneities in elastic matrix materials and found that the elastic field is size-dependent when the hole or inhomogeneity length parameter is less than 15 nm.

As for the GaN nanorods studied in this work, when the nanoscale surface effect is incorporated in a better way, the image force behavior should be expected to be distinct, and the dislocation dissipation could be investigated more accurately. Based on the methodology introduced in this work, it provides a feasible approach to incorporate the surface stress into the current dislocation model without great effort. This improvement might be crucial to the design and fabrication of nanostructures, especially when their dimensions are below 10 nm.

CHAPTER 4

NANOSTRUCTURE PROPERTIES BY ATOMISTIC SIMULATIONS

This chapter provides a brief introduction to atomistic simulations and focus on the use of Molecular Dynamic (MD) simulations to obtain bulk and surface properties of crystals. The concept of surface excess energy will also be illustrated in this chapter, which brings about the definition of elastic surface property tensors. Finally, a complete dataset of GaN surface property tensors will be obtained and it could be used to study the surface effect of GaN nanostructures in the future.

Description of Molecular Dynamic Simulation

Nowadays, simulation models can cover quite a broad area of research interests and also involves different scales of length and time step[46]. Basically, in any simulation, a hierarchy of length and time scales is first established within the physical ensemble. Second, the elementary objects (atoms, clusters, grains, etc.) handled on the various scales of interest are defined. Third, those physical processes which are irreducible and independent at a given length scale are identified. The processes and objects handled at a given scale usually represent ‘averages’ calculated at the immediately lower scale.

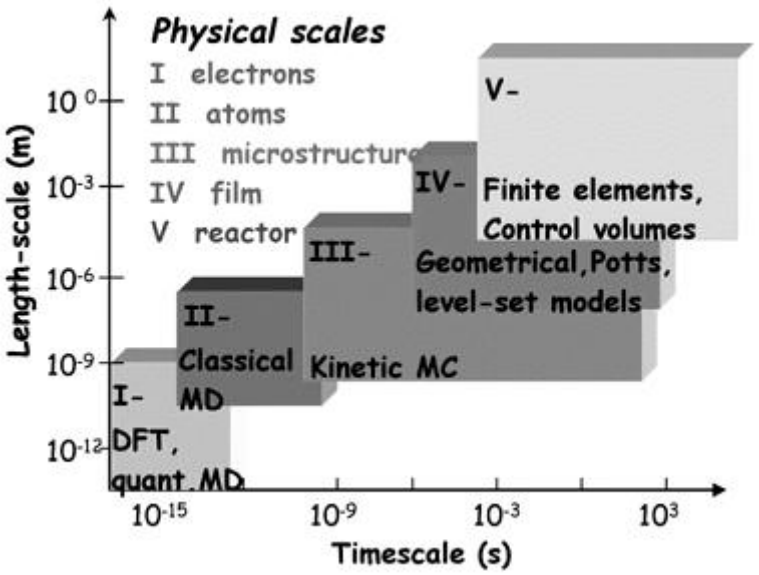

Figure 17. Simulation models in Materials Science and related length and time scale

In Figure 17 [46], it shows the characteristic length and time scales accessible to the main types of simulation models used in Materials Science. Ab initio methods such as density functional theory (DFT) or Carr–Parrinello (CP) Molecular Dynamics[47] are capable of describing electronic interactions between a few hundreds of atoms, in static (DFT) or over extremely short time scales (10^{-13} s for CP). They are generally used to calculate transition state structures, surface reaction pathways, etc. Electronic interactions are represented by empirical potentials in classical Molecular Dynamics models[48], thus enabling the simulation of the real atomic motions in systems of typically 10^5 atoms over 10^{-9} s. Classical Monte Carlo models [49] can also be used to determine the equilibrium state of molecular systems of this size, but they do not provide accurate information on dynamics. Conversely, Kinetic Monte Carlo (KMC) models[50], which are generally lattice-based, are capable of simulating atomic motions in systems consisting of more than 10^6 atoms over typically 10^3s. KMC models do not provide a description of atomic interactions as accurate as MD models, but they have a unique potential of bridging atomic scale and microscopic scale in dynamic simulations. Finally, continuum models

based on finite elements or finite volume methods are generally used to simulate transport phenomena inside the preparation chamber[51].

In MD simulations or any other atomistic simulations, the interatomic potentials are at the heart of the simulations. In classical atomistic simulations, the atoms are represented by mass-points in space interacting through many-body interactions potential. The complex description of electrons dynamics is abandoned and an effective depiction is taken. In this picture, the interatomic interaction and internal degrees of freedom are completely defined by a set of parameters and functions which depend on the positions of the atoms in the system.

As for the simulation tool, we adopt the freely−available open−source code: LAMMPS[49]. It is a classical molecular dynamics code that models an ensemble of particles in a liquid, solid, or gaseous state. It can model atomic, polymeric, biological, metallic, granular, and coarse−grained systems using a variety of force fields and boundary conditions. It can model systems with only a few particles up to millions or billions. LAMMPS runs efficiently on single−processor desktop or laptop machines, but is designed for parallel computers. It will run on any parallel machine that compiles C++ and supports the MPI message−passing library.

Bulk Properties of Nanostructures

In continuum mechanics, the elastic constants of crystal material are well defined. To keep consistent with the ideas of atomistic simulations later, here we introduce the elastic constants through the Taylor's expansion of the total strain energy density at the state of zero stress and strain:

$$E = \frac{1}{2} C_{ijkl} \varepsilon_{ij} \varepsilon_{kl} + \frac{1}{6} C_{ijklmn} \varepsilon_{ij} \varepsilon_{kl} \varepsilon_{mn} + \ldots \tag{22}$$

where ε_{ij} is the Lagrangian strain measured from the perfect lattice of an undeformed crystal of infinite extent, C_{ijkl} is a fourth order stiffness tensor consists of second order elastic constants, and C_{ijklmn} is a sixth order tensor consisting of the third order elastic constants of the solid.

All are defined in the reference configuration, or the initial stress-free configuration. In our case, we will neglect the sixth order and higher order items. The symmetric Piola-Kirchhoff stress is the gradient of the strain energy with respect to the strain:

$$\sigma_{ij} = \frac{\partial E}{\partial \varepsilon_{ij}} = C_{ijkl}\varepsilon_{kl} \tag{23}$$

In crystals, because of the symmetry of the structure systems, some components in the stiffness tensor will be null, and the most general anisotropic elastic solids require only 21 elastic constants. We can write the stiffness tensor in the following way.

$$C = \begin{bmatrix} C_{1111} & C_{1122} & C_{1133} & C_{1123} & C_{1113} & C_{1112} \\ C_{1122} & C_{2222} & C_{2233} & C_{2223} & C_{2213} & C_{1222} \\ C_{1133} & C_{2233} & C_{3333} & C_{2333} & C_{1333} & C_{1233} \\ C_{1123} & C_{2223} & C_{2333} & C_{2323} & C_{2313} & C_{1223} \\ C_{1113} & C_{2213} & C_{1333} & C_{2313} & C_{1313} & C_{1213} \\ C_{1112} & C_{1222} & C_{1233} & C_{1223} & C_{1213} & C_{1212} \end{bmatrix} \tag{24}$$

The indices of the notation above are quite cumbersome, so it's often in a simplified or contracted form:

$$C = \begin{bmatrix} C_{11} & C_{12} & C_{13} & C_{14} & C_{15} & C_{16} \\ C_{12} & C_{22} & C_{23} & C_{24} & C_{25} & C_{26} \\ C_{13} & C_{23} & C_{33} & C_{34} & C_{35} & C_{36} \\ C_{14} & C_{24} & C_{34} & C_{44} & C_{45} & C_{46} \\ C_{15} & C_{25} & C_{35} & C_{45} & C_{55} & C_{56} \\ C_{16} & C_{26} & C_{36} & C_{46} & C_{56} & C_{66} \end{bmatrix} \tag{25}$$

where C_{ij} is no longer the component of a second order tensor.

Considering some special materials, such as monoclinic, orthotropic or isotropic materials, they have planar or axial symmetry in their structure themselves, so the form can be even simplified more. In the next chapter, we will see the calculation of elastic constants for pure metals, for example, copper has FCC cubic lattice structure, and its stiffness tensor can be written as the following:

$$C = \begin{bmatrix} C_{11} & C_{12} & C_{12} & & & \\ C_{12} & C_{11} & C_{12} & & 0 & \\ C_{12} & C_{12} & C_{11} & & & \\ & & & C_{44} & 0 & 0 \\ & 0 & & 0 & C_{44} & 0 \\ & & & 0 & 0 & C_{44} \end{bmatrix} \tag{26}$$

The calculation procedures of the three elastic constants are quite similar. The principle is based on curve-fitting the parabola function between the total strain energy density and the strain. To simulate an infinite crystal, we constructed a rectangular cell and used periodic boundary conditions in all directions to mimic a crystal of infinite extend. A typical calculation cell contains 500 atoms. A bigger calculation sample is not necessary since the dimension of the calculation box are chosen to be at least twice as big as the cut-off distance of the interatomic potential.

For calculations, we have performed a strain meshing of the calculation cell with strains in the three directions ranging from -1% to 1% and incremented by ±0.01% strain steps. The calculation cell is stretched by independently varying the lattice constants along the three directions. This state corresponds to the energy state of the cell in the strain space. The procedure yields to a strain mesh of the total strain energy of the sample with respect to the reference configuration. The general steps of the calculation can be outlined as follows:

(a) Create the initial assembly using the given material properties (atomic weight, lattice spacing, EAM potential, crystallographic orientation, etc…).

(b) Apply a small strain field to the assembly.

(c) Compute the energy density corresponding to this given strain field.

(d) Increase the magnitude of strain and repeat steps (b) and (c).

After repeating steps (b) – (d) a sufficient number of times, we obtain a mesh strain energy density of as a function of the strain. A numerical interpolation of the energy density was performed to evaluate the elastic constants.

In our work, we compute pairwise interactions for FCC metals using embedded−atom method (EAM) potentials[52]. In the EAM framework, the total energy of an atom is expressed as the sum of the contribution from the energy of two-body interactions and the embedding energy incorporating the complex nature of metallic cohesion. Among all of the interatomic potentials, the EAM method is a very efficient technique for modeling realistic descriptions of metallic cohesion. It is a semi-empirical approach that uses multi-atom potential for modeling the interatomic forces. In this scheme all atoms are treated in a unified way. The method is so called “embedded” because it views each atom individually as if it was embedded in a host lattice comprising all other atoms. It has the important benefit of keeping the computational scaling on the

order of magnitude of N (if N is the number of particle composing the system) whereas more complex and thorough many-body potential scale on the order of magnitude N^3 (for instance, Density Functional Theory).

Let us take FCC Cu for example. For elastic constant C_{11}, by applying strain as $\varepsilon_{11} = \varepsilon$ and other strain components as zero (see Figure 18), The total strain energy density is simply as $E = \frac{1}{2} C_{11} \varepsilon^2$.

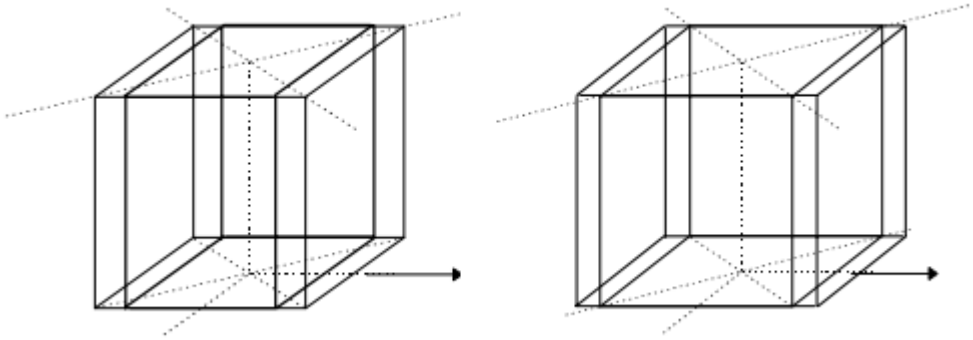

Figure 18. Deformation applied to the crystal Cu for calculation of C11

The interpolation result of the energy density vs. strain is shown in Figure 19, and the value obtained is C_{11} = 173.2 GPa.

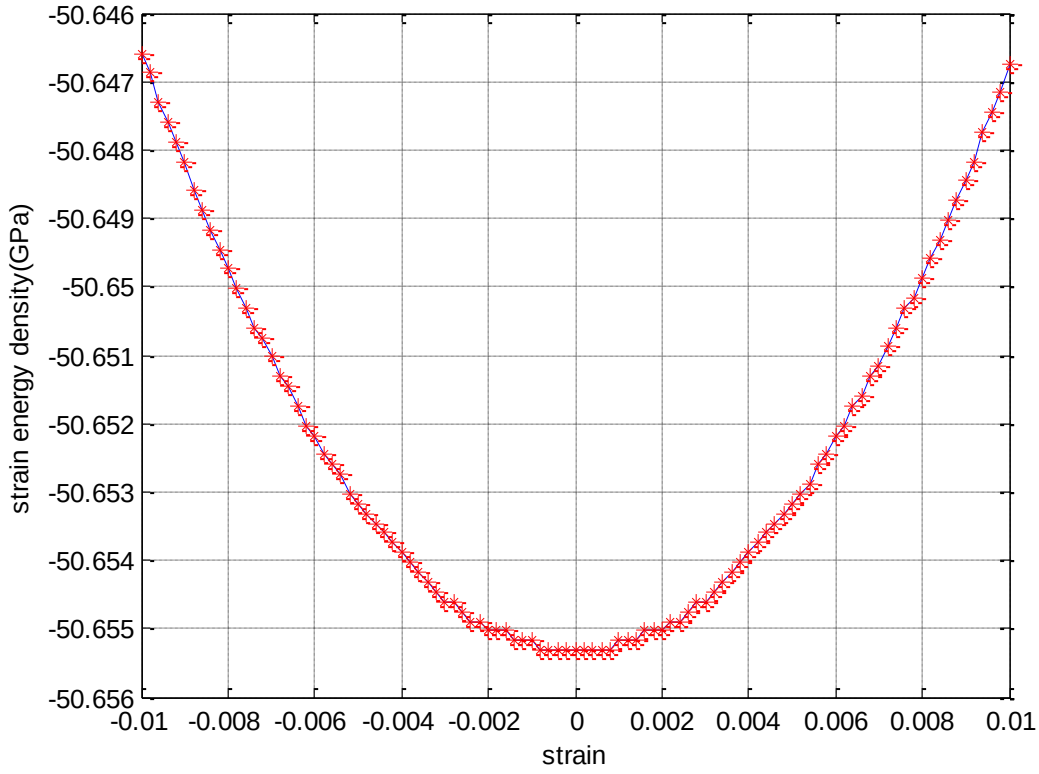

Figure 19. Interpolation result of C_{11} of Cu

For elastic constant C_{12}, by applying strain as $\varepsilon_{11} = -\varepsilon_{22} = \varepsilon$ and other strain components as zero (see Figure 20), the total strain energy density is simply as $E = (C_{11} - C_{12})\varepsilon^2$.

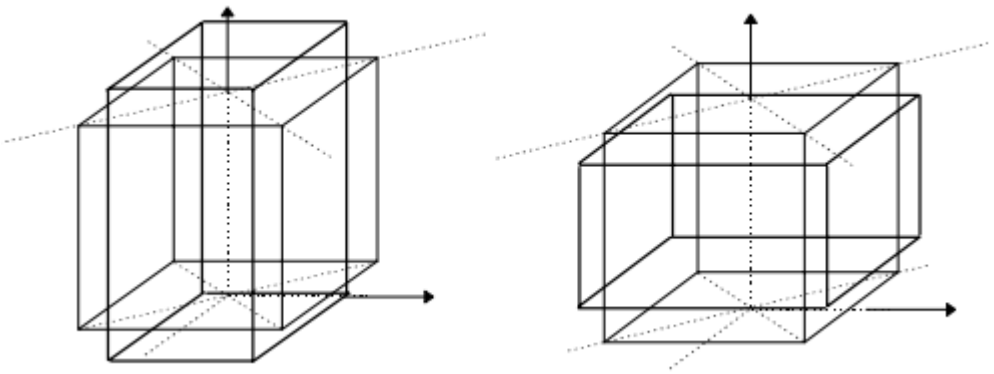

Figure 20. Deformation applied to the crystal Cu for calculation of C12

The interpolation result of the energy density vs. strain is shown in Figure 21, and the value obtained is C_{12} = 129.2 GPa.

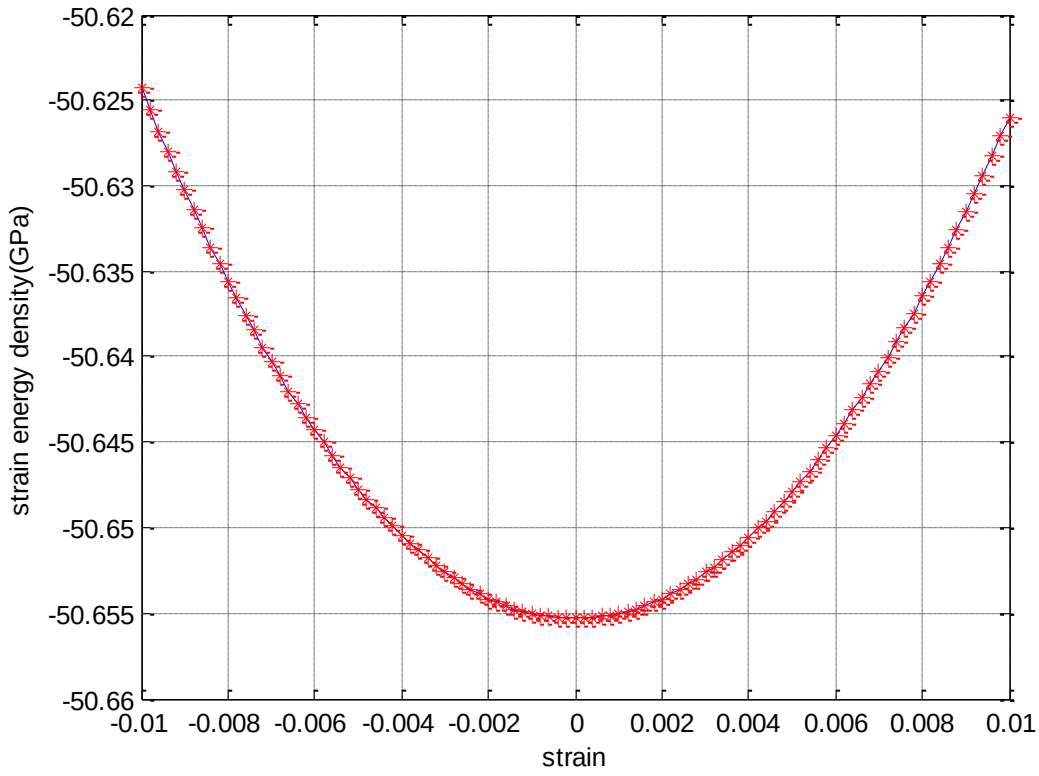

Figure 21. Interpolation result of C_{12} of Cu

This methodology for calculation of elastic constants is quite efficient and satisfactory. As long as a proper interatomic potential of the material is provided, its elastic constants can just be obtained by following this standard procedure. In our work, we also test this with other materials and compare our results to those literatures. The final results are listed in Table 2 (see more details in [53]).

Table 2. Results of elastic constants by MD simulations (unit: GPa)

	Cu	Au	Pd	Pt
C_{11}	167.1[54]	183.1[54]	198.3[54]	331.7[54]
	166.1[55]	192.9[55]	224.9	313.0
	173.2	189.1		
C_{12}	124.0[54]	158.7[54]	170.4[54]	294.2[54]
	119.9[55]	163.8[55]	191.9	283.1
	129.2	164.8		

Surface Properties of Nanostructures

The initial idea of "surface energy" can date back to the year of 1928 when Gibbs[56] first formulated the thermodynamics of a fluid interface through the use of interfacial free energy, which is a single dividing surface used to separate two homogeneous phases, and the interface contribution to the thermodynamic properties is defined as the excess over the values that would be obtained if the bulk phases retained their properties constant up to an imaginary surface (of zero thickness) separating the two phases. Gibbs showed that various combinations of the interfacial excess quantities can yield physically meaningful and experimentally measurable variables which are independent of the dividing surface position. By following Gibbs' work, Shuttleworth and many other researchers [16, 57, 58] extended this Gibbsian description of fluid-fluid interfaces to solid-solid interfaces and to associate a "surface stress" with the change of in interfacial energy upon deformation. From then on, instead of considering the surface excess energy as a constant quantity in all situations, researchers began to take the surface excess energy as a function of the surface strain, which is only due to the in-plane

deformation. For example, Shama[59] has used the Shuttleworth equation for solid-solid interfaces such as grain boundaries. On the other hand, although there are many similarities between a free surface and an interface in elastic solid, in the early 80s, Andreev and Kosevich[60]1 already noticed that there is one key difference between them, namely, in addition to in-plane deformation, an interface may be subjected to transverse (normal to the interface) stress. Such transverse stress and the corresponding transverse deformation also contribute to the interfacial excess, but they did not give an expression of the contribution from the transverse stress. Recently, Dingreville[54] provided a comprehensive way of determining the interfacial excess energy by taking consideration of both in-plane deformation and the effects of transverse stress. Later, Dingreville and Qu[61] successfully applied this approach to estimate interface elastic properties with a semi-analytical method of calculation.

The surface free (excess) energy of a near surface atom, E_n is defined by the difference between its total energy and that of an atom deep in the interior of a large crystal. Clearly, E_n depends on the location of the atom. If there are N atoms surrounding an area A in the deformed configuration, the Gibbs surface excess energy density is defined as the following:

$$\Gamma = \frac{1}{A}\sum_{i=1}^{N} E_i \tag{27}$$

From the work of Dingreville[54], this surface excess energy is linked to the surface stress and surface strain by introducing some surface property tensors. It then follows that the interfacial excess energy can be re-rewritten as:

$$\Gamma = \Gamma_0 + \Gamma^{(1)} : \varepsilon^s + \frac{1}{2}\varepsilon^s : \Gamma^{(2)} : \varepsilon^s \tag{28}$$

where Γ is the surface excess energy, ε^s is the surface strain and $\Gamma_0, \Gamma^{(1)}, \Gamma^{(2)}$ are the surface property tensors.

It is obvious that if no stress or strain is applied, the surface excess energy form is reduced to only the first item Γ_0 which becomes a constant quantity, and this is consistent to the definition originally introduced to fluid surfaces. However, when stress or strain is applied, the surface excess energy is no longer an intrinsic material property, but also depends on the surface strain. The second term $\Gamma^{(1)}$ is a two-dimensional second order tensor representing the internal excess stress of the surface. It is the part of residual stress that exists when the surface strain is absent. The third term $\Gamma^{(2)}$ is related to the two-dimensional fourth order tensor that represents the surface's in-plane elasticity.

The surface property tensors are intrinsic properties of the "elastic" surface. They can be calculated for a given material with known interatomic potentials by Molecular Dynamic (MD) simulations. Once these tensors are known, the elastic behavior of the surface is fully characterized.

The calculation procedures of the surface property tensors are quite similar to those of bulk elastic constants. In our calculations, we have performed a strain meshing of the calculation cell with strains in the two planar directions ranging from -1% to 1% and incremented by ±0.01% strain steps. Periodic boundary conditions are used in the two planar directions with free surfaces in the vertical direction to mimic an infinite plane. By varying the number of layers of atoms in the vertical direction we can represent thin films of different thicknesses. The slab thickness must be chosen to be thick enough to avoid interaction between the two surfaces. The film is stretched by independently varying the lattice constants along the two planar directions, while atoms in the third direction can fully relax. Prior to any deformation, the first step of the calculation is to determine the self equilibrium state of the films. This state corresponds to the lowest

energy state of the film in the strain space. The self equilibrium state serves as a reference configuration for the crystal. The procedure yields to a mesh of the total strain energy of the sample with respect to the reference configuration. The surface free energy of a near surface atom is obtained by taking the difference between its total energy and that of an atom deep in the interior of a large crystal. The procedure described above can be outlined in the following steps:

(a) Create the initial assembly using the given material properties (atomic weight, lattice spacing, atomic potential, crystallographic orientation, etc.).

(b) Equilibrate the assembly to find the self equilibrium state.

(c) Apply a small strain field to the assembly and re-equilibrate.

(d) Compute the surface energy density corresponding to this given strain field.

(e) Increase the magnitude of strain and repeat steps (c) and (d).

After repeating steps (c) – (d) a sufficient number of times, we obtain a mesh of surface energy density as a function of surface strains. Through curve fitting of Eq. (28), the coefficients of the surface property tensors can be determined.

By applying strain as $\varepsilon_{11} = \varepsilon$ and other strain components as zero, the total surface strain energy density is simply as:

$$\Gamma = \Gamma_0 + \Gamma_{11}^{(1)}\varepsilon + \frac{1}{2}\Gamma_{1111}^{(2)}\varepsilon^2 \tag{29}$$

By applying strain as $\varepsilon_{11} = \varepsilon_{22} = \varepsilon$ and other strain components as zero, the total surface strain energy density is simply as:

$$\Gamma = \Gamma_0 + (\Gamma_{11}^{(1)} + \Gamma_{22}^{(1)})\varepsilon + (\Gamma_{1111}^{(2)} + \Gamma_{1122}^{(2)})\varepsilon^2 \quad (30)$$

In both interpolations Γ_0 will be calculated. In this case, we also checked that the twice obtained values of Γ_0 here are the same. Table 3 shows the result of all the nonzero surface property tensors for Cu (100) surface and Table 4 shows the result of all the nonzero surface property tensors for Cu (110) surface.

Table 3. Results of surface tensors by MD simulations for Cu (100) surface (unit: J/m^2)

Γ_0	$\Gamma_{11}^{(1)}$	$\Gamma_{1111}^{(2)}$	$\Gamma_{1122}^{(2)}$
1.288[54]	1.396[54]	-0.712[54]	5.914[54]
1.28[52]	1.38[62]	-0.8328	5.3020
1.3584	0.1118		

Table 4. Results of surface tensors by MD simulations for Cu (110) surface (unit: J/m^2)

Γ_0	$\Gamma_{11}^{(1)}$	$\Gamma_{22}^{(1)}$	$\Gamma_{1111}^{(2)}$	$\Gamma_{2222}^{(2)}$	$\Gamma_{1122}^{(2)}$
1.413[54]	-1.126[54]	-0.993[54]	-7.798[54]	-2.263[54]	-3.600[54]
1.40[52]	0.957[63]	0.957[63]	-11.8204	-3.0120	-0.2657
1.4896	0.2889	0.4436			

Through the same approach, the surface elastic tensors of wurtzite GaN are also calculated in this work. The interatomic potential of GaN is taken from a three-body Tersoff potential [28]. The basic idea is to use a bond-order potential form, where the total potential energy is written as a sum over individual bond energies:

$$E = \sum_{i>j} f_{ij}(r_{ij})[V_{ij}^{R}(r_{ij}) - \frac{B_{ij} + B_{ji}}{2} V_{ij}^{A}(r_{ij})], \tag{31}$$

where the pair-like repulsive and attractive energies are given as Morse-like terms:

$$V^{R}(r) = \frac{D_0}{S-1} e^{-\beta\sqrt{2S}(r-r_0)}, \tag{32}$$

$$V^{A}(r) = \frac{SD_0}{S-1} e^{-\beta\sqrt{2/S}(r-r_0)}, \tag{33}$$

where D_0 is the dimer bond energy; r_0 is the dimer bond distance; S is the adjustable variable and β is the parameter to be determined by the ground state oscillation frequency of the dimer.

The interaction is restricted to the next-neighbour sphere by a cut-off function that is given as:

$$f(r) = \begin{cases} 1, r \le R - D, \\ 1/2 - \sin\{\pi(r-R)/(2D)\}/2, |R-r| \le D, \\ 0, r \ge R + D \end{cases} \tag{34}$$

where D and R are adjustable variables.

The bond-order parameter B_{ij} includes angular dependencies, which are necessary to accurately model the deformation of covalent bond:

$$B_{ij} = \frac{1}{\sqrt{1+\chi_{ij}}}, \tag{35}$$

where χ_{ij} consists of a cut-off function:

$$\chi_{ij} = \sum_{k \neq i,j} f_{ik}(r_{ik}) g_{ik}(\theta_{ijk}) e^{2\mu_{ik}(r_{ij}-r_{ik})}. \tag{36}$$

The indices monitor the type-dependent parameters of the bonds, which are important to describe the compound. The angular function is given as:

$$g(\theta_{ijk}) = \gamma[1 + \frac{c^2}{d^2} - \frac{c^2}{d^2 + (h + \cos(\theta_{ijk}))^2}], \tag{37}$$

where c, d, h and γ are all adjustable variables.

The GaN Tersoff potential is presented to describe a wide range of structural properties of GaN as well as bonding and structure of the pure constituents. Although long-range interactions are not explicitly included in the potential, it provides a good fit to different structural geometries including defects and high-pressure phases of GaN[28]. The GaN Tersoff potential is also pre-packaged with LAMMPS. Following the similar procedures for copper crystals, the result of different surfaces is shown in Table 5.

Table 5. Surface property tensors for wurtzite GaN (unit: N/m)

	(11-20)	(10-10)	(0001)
Γ_0	2.4420/1.9707[64]	2.1045/1.8906[64]	1.9671/2.0027[65]
$\Gamma_{11}^{(1)}, \Gamma_{22}^{(1)}$	-1.1608	-1.4226	-1.5871
$\Gamma_{1111}^{(2)}, \Gamma_{2222}^{(2)}$	-26.8376	2.0299	2.0299
$\Gamma_{1122}^{(2)}, \Gamma_{2211}^{(2)}$	-11.0793	-4.5780	-2.1985

Unfortunately, there are very few research reports about the surface property tensors for GaN in literatures. Here we only found the references on the constant surface excess energy values and they are obtained by first principle calculations[64, 65]. Our results agree well with those of the first principle calculations.

The results of GaN surface property tensors will be fed into the continuum work in the following part. This work will combine the outcome of the atomistic simulations with the continuum models to investigate the nano-epitaxy process. However, the GaN dataset in Table 5 is not only limited to use in this work, but also can be applied to other studies if necessary.

CHAPTER 5

DISLOCATION DISSIPATION BY ELASTIC SURFACES

This chapter aims at developing an analytical solution to the elastic field of solids with dislocations and surface stress. First, a complete analytical framework of stress/strain solution for general 3D anisotropic materials will be established based on the concept of eigenstrain. Second, we will study the 2D case of infinite isotropic circular nanowire to validate our solution by comparing with the classical one and complex variable method. Finally, the analytical formulation of image force for the nanowire will also be derived. This will be the foundation of further investigation of the image force in 3D anisotropic materials.

Analytical Framework of Stress/Strain Solutions

The knowledge of the stress and strain fields in solids is of great importance to determine the properties of the materials and thus predict their behaviors. Defects like dislocations, cracks, lattice mismatches and etc., could have crucial influence on the stress and strain fields. Within the scope of elastic deformations, Eshelby's pioneering work [66-68] led to a general framework to formulate the elastic fields in solids by introducing the concept of eigenstrain. Dundurs et al. [69, 70] studied the elastic fields with the consideration of the interaction between an edge dislocation and a circular inclusion. Lubarda [71] obtained the stress fields for screw and edge dislocations emitted from a cylindrical void and provided analytical formulations for image forces on dislocations. Shodja et al. [72-74] proposed a different scheme to analyze the displacement and strain fields of a screw dislocation in a nanowire using gradient elasticity theory. In such formulations and many more, there is no intrinsic length scale

associated in these constitutive relationships. Therefore, these results should be considered only in macroscopic cases.

Nanostructures have at least one of its dimensions below tens of nanometers. Due to the large surface to volume ratio, the surface stress begins to play an important role in changing the constitutive laws seen in the classical elastic theory. In this case, nanostructures usually demonstrate some size-dependent properties that could not be seen in conventional materials. This significant difference could be critical in fabrications and designs, so great efforts have been devoted to investigating the effect of surface stress. Relationship of the deformation-dependent surface energy with the surface stress was first described by the Shuttleworth's equation[16]. Gurtin et al. [17, 18] linked the surface stress to the bulk stress at the vicinity of the surface by regarding the surface as a negligibly thin object adhering to the underlying material without slipping. Fang et al. [19-22, 75] combined the surface stress model with complex variable method to solve the stress fields for a screw or edge dislocation located in materials of a circular nanowire embedded in an infinite matrix. Luo and Xiao [23] extended this analysis to the case of an elliptical nanowire embedded in an infinite matrix with conformal mappings. Recently, Ahmadzadeh-Bakhshayesh et al. [24] adopted the same method to analyze the surface/interface effect on elastic behavior of a screw dislocation in an eccentric core–shell nanowire. However, these results based on the complex variable method provide the stress fields as infinite power series, which are difficult to manipulate in further situations. The influences of the size parameter and surface elasticity are also hard to interpret clearly. Beside this limitation, their solutions by using the complex variable method are limited to Airy's stress functions which are only capable to deal with 2D elastic plane stress or strain problems and mainly used for isotropic materials.

Practically, most nanostructures are fabricated with anisotropic materials and they have 3D shapes [8, 76-80]. Kern and Müller [38] studied the strain relaxation inside isolated nanoislands deposited on substrate with a given lattice mismatch, and they

approximated the single nanoisland as an isotropic cube to obtain the analytical result of the strain distribution. Based on this, Bourret et al. [81] analyzed the strain distributions in (0001) AlN/GaN heterostructures and emphasized the important role of the flat platelets for dislocation nucleations. Recently, Colby et al. [15] investigated the dislocation filtering behavior in GaN nanodots (with a cylindrical base and a pyramid cap) by selective area growth through a nanoporous template. This dislocation dissipation mechanism has been studied numerically through finite element method [14, 82], in which the surrounding surfaces are considered only as free surfaces. In such situations, the possibility to obtain analytical stress or strain solutions should have a critical importance to investigate the general anisotropic 3D nanostructrues with surface effects. This will also bring much convenience in the design and fabrication process.

This work follows the concept of eigenstrain to describe the defect in solids. We use Green's function to formulate the strain or stress field, and also take into account the surface effect by considering the surface stress to a fictitious traction boundary condition. Our framework provides a complete analytical formulation for a general 3D domain of defected material with elastic anisotropy.

In Figure 22, consider an elastic solid of domain (V) with an inclusion (Ω) prescribed with an eigenstrain ε^*. The solid is subjected to traction boundary condition on its surface (S).

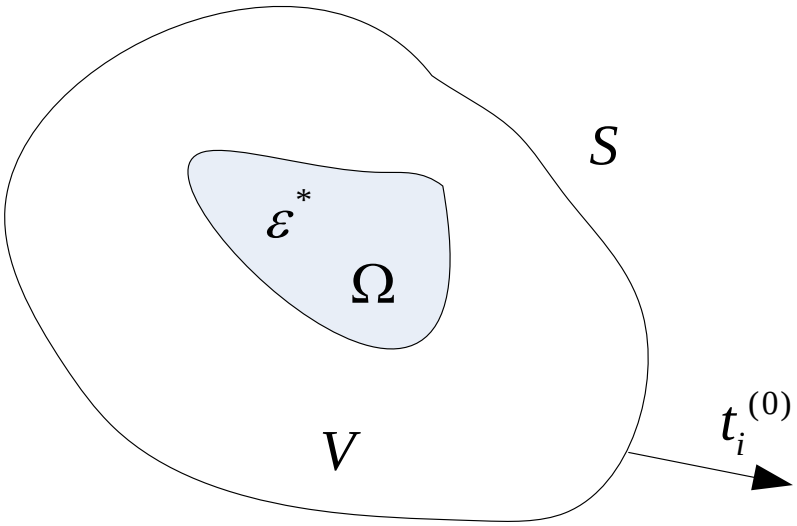

Figure 22. An elastic solid of domain (V) with an inclusion (Ω) prescribed with an eigenstrain

The constitutive relationship of the stress and the strain is:

$$\sigma_{ij} = L_{ijkl}(\varepsilon_{kl} - \varepsilon^{*}_{kl}) \tag{38}$$

where L_{ijkl} is the stiffness tensor of the material.

The strain is related to the displacement through compatibility condition:

$$\varepsilon_{ij} = \frac{1}{2}(u_{i,j} + u_{j,i}) \tag{39}$$

The traction boundary condition reads:

$$t_i^{(0)} = \sigma_{ij}^{b} n_j \tag{40}$$

where σ_{ij}^{b} is the bulk stress at the vicinity of the surface and n_j is the normal unit of the surface.

When no surface stress is concerned, the complete displacement field is given in classical micromechanics [31]:

$$u_i(\vec{x}) = \int_V L_{mnkl}\varepsilon_{kl}^{*}(\vec{y})\frac{\partial G_{mi}(\vec{x},\vec{y})}{\partial y_n}dV_y + \int_S t_k^{(0)}(\vec{y})G_{ik}(\vec{x},\vec{y})dS(\vec{y}), \tag{41}$$

where $G_{ij}(\vec{x},\vec{y})$ is the Green's function that embodies the interaction between point $\vec{x}$ and $\vec{y}$ in the material.

From Eqs. (39) and (41), the strain field is obtained as:

$$\varepsilon_{ij}(\vec{x}) = \int_V L_{klmn}\Gamma_{ijkl}(\vec{x},\vec{y})\varepsilon_{mn}^{*}(\vec{y})dV(\vec{y}) + \int_S Q_{ijk}(\vec{x},\vec{y})t_k^{(0)}(\vec{y})dS(\vec{y}), \tag{42}$$

where

$$\Gamma_{ijkl}(\vec{x},\vec{y}) = \frac{1}{2}\left(\frac{\partial^2 G_{ki}(\vec{x},\vec{y})}{\partial y_l \partial x_j} + \frac{\partial^2 G_{kj}(\vec{x},\vec{y})}{\partial y_l \partial x_i}\right), \tag{43}$$

$$Q_{ijk}(\vec{x},\vec{y}) = \frac{1}{2}\left(\frac{\partial G_{ik}(\vec{x},\vec{y})}{\partial x_j} + \frac{\partial G_{jk}(\vec{x},\vec{y})}{\partial x_i}\right). \tag{44}$$

When surface stress is concerned, the bulk stress state at the vicinity of the surface is determined from the surface stress [17, 18]:

$$\sigma^s_{\alpha\beta,\beta} + \sigma^b_{\alpha\beta} n_\beta = 0, \tag{45}$$

$$\sigma^s_{\alpha\beta} \kappa_{\alpha\beta} = \sigma^b_{ij} n_i n_j, \tag{46}$$

where $\sigma^s_{\alpha\beta}$, $\sigma^b_{\alpha\beta}$ are the surface stress and bulk stress respectively and $\kappa_{\alpha\beta}$ is the curvature tensor.

It should be noted that the surface stress tensor is a two-dimensional quantity and the strain normal to the surface is excluded. Thus, the Greek indices take the value of 1 or 2, while Latin subscripts adopt values from 1 to 3.

Consider a linear constitutive relationship between surface stress and surface strain as[83]:

$$\sigma^s_{\alpha\beta} = \tau^0_{\alpha\beta} + S_{\alpha\beta\gamma\delta} \varepsilon^s_{\gamma\delta}, \tag{47}$$

where $\tau^0_{\alpha\beta}$ is the residual surface stress when the bulk is unstrained, $S_{\alpha\beta\gamma\delta}$ is the elastic constants for the surface that can be determined from atomistic calculations. $\varepsilon^s_{\gamma\delta}$ is the surface strain that only accounts for in-plane deformation usually.

When the surface is assumed to be coherent, the surface strain is the same as the bulk strain at the vicinity of the surface. In this way, the bulk stress at the vicinity of the surface is linked to the surface properties from Eqs. (45) - (47) as:

$$\sigma^b_{\alpha\beta} = \sigma^b_{\alpha\beta}(\tau^0_{\alpha\beta}, S_{\alpha\beta\gamma\delta}, \kappa_{\alpha\beta}, \varepsilon^s). \tag{48}$$

When no external load is applied on the boundary, due to the effect of the surface stress, the traction boundary condition could be converted to a fictitious traction contributed from the surface stress by substituting Eq. (48) into (40):

$$t_i^{(0)} = \sigma_{ij}^b(\tau_{\alpha\beta}^0, S_{\alpha\beta\gamma\delta}, \kappa_{\alpha\beta}, \varepsilon^s)n_j. \tag{49}$$

Thus, the strain field with prescribed eigenstrain and surface stress is given as:

$$\varepsilon_{ij}(\vec{x}) = \int_V L_{klmn}\Gamma_{ijkl}(\vec{x},\vec{y})\varepsilon_{mn}^*(\vec{y})dV(\vec{y}) + \int_S Q_{ijk}(\vec{x},\vec{y})\sigma_{kl}^b(\tau_{\alpha\beta}^0, S_{\alpha\beta\gamma\delta}, \kappa_{\alpha\beta}, \varepsilon^s(\vec{y}))n_l(\vec{y})dS(\vec{y}). \tag{50}$$

For convenience, Eq. (50) is denoted by two parts:

$$\varepsilon_{ij} = \varepsilon_{ij}^1 + \varepsilon_{ij}^2 \tag{51}$$

where

$$\varepsilon_{ij}^1 = \varepsilon_{ij}^1(\vec{x}, \varepsilon^*) = \int_V L_{klmn}\Gamma_{ijkl}(\vec{x},\vec{y})\varepsilon_{mn}^*(\vec{y})dV(\vec{y}), \tag{52}$$

$$\varepsilon_{ij}^2 = \varepsilon_{ij}^2(\vec{x}, \varepsilon^s) = \int_S Q_{ijk}(\vec{x},\vec{y})\sigma_{kl}^b(\tau_{\alpha\beta}^0, S_{\alpha\beta\gamma\delta}, \kappa_{\alpha\beta}, \varepsilon^s(\vec{y}))n_l(\vec{y})dS(\vec{y}). \tag{53}$$

The first part, ε_{ij}^1 is in fact the classical solution to the eigenstrain problem with free surfaces, and it has been solved analytically for different types of eigenstrain [30, 31]. The second part, ε_{ij}^2 can be interpreted as the influence of the surface stress on the elastic field of the solid. In practical applications, the eigenstrain is usually pre-defined

and the solution of ε_{ij}^{1} could be adopted directly from literatures. Meanwhile, the ε_{ij}^{2} part contains the surface property tensors that could be determined by atomistic simulations, so the only unknown on the right side of Eq. (51) is the surface strain. In this way, the feature of Eq. (51) is an implicit equation of the strain field. One can set point $\vec{x} \in S$ first to solve ε^{s} and then plug it back to obtain the whole strain field.

Furthermore, Eq. (51) demonstrates a general analytical framework to solve the elastic field for solids with defects by considering surface effect. Compared to the limitations of complex variable method, this framework is applicable to anisotropic materials and 3D structures. More importantly, it allows for the exact analytical expression of the results instead of the power series solution in complex variable method. Such exact analytical expressions of the stress or strain field will be more flexible to manipulate in further applications, and the physical meanings of the surface property parameters are straightforward to interpret.

Validation in Case of Isotropic Circular Nanowire

The analytical framework could be used for 3D anisotropic solids with general defects. In some cases, numerical methods should be employed when the structure is quite complex, but analytical solutions are possible to be obtained for simple scenarios. As an application, this work has obtained the analytical close-form solutions to the stress fields of an infinite isotropic circular nanowire.

Nanowire is one of the important nanostructures in the fabrication and design. The radius of its cross section varies from several nanometers to tens of nanometers, while its longitudinal length could be sufficiently long that the nanowire could be seen as an infinite long and thin cylinder. Since the lateral surface is so close to the center, the surface stress affects the behavior of the nanowire dramatically. In addition to that, when there is a dislocation embedded in the nanowire, the interaction between the dislocation and the surrounding surface has drawn a great attention to many researches. To establish

a systematic model for this problem, the complex variable method is often used and the solutions are provided in infinite power series form [19-24]. In this section, based on the framework of the Section 2, the stress field is solved for an infinite long isotropic nanowire with a screw dislocation effected by the surface stress. The results of the stress fields are compared between this work and those of complex variable method.

Consider a straight screw dislocation with Burgers vector $\vec{b} = [0, 0, b]$ oriented in <001> direction in the nanowire (Figure 23). The radius of the nanowire is R and the dislocation is located on x_1-axis with an offset of a from the center. The bulk material elastic constants are denoted by μ as the shear modulus and υ as the Poisson's ratio.

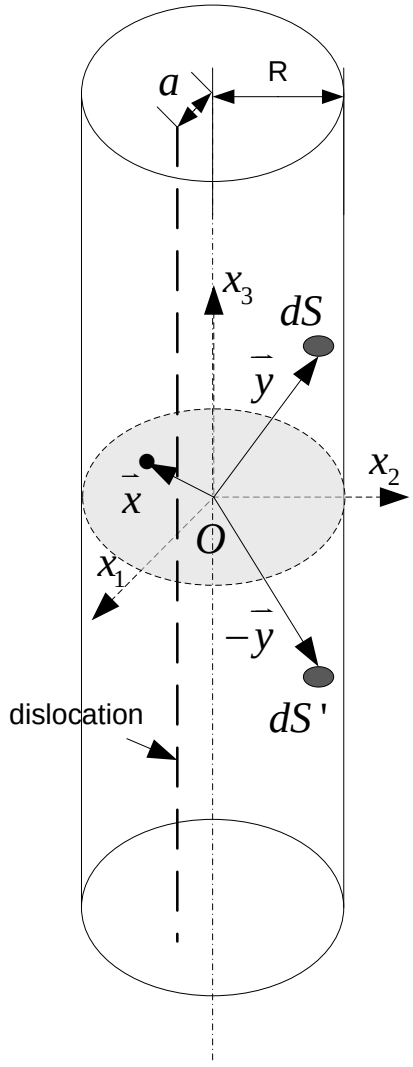

Figure 23. A circular nanowire with a straight screw dislocation inside

The surface elasticity is also considered to be isotropic and the surface constitutional relationship of Eq. (47) is simplified as[18]:

$$\sigma^s_{\alpha\beta} = \tau^0\delta_{\alpha\beta} + 2(\mu^0 - \tau^0)\varepsilon_{\alpha\beta} + (\lambda^0 + \tau^0)\varepsilon_{\gamma\gamma}\delta_{\alpha\beta}, \tag{54}$$

where μ^0 and λ^0 are the surface Lam é constants; $\delta_{\alpha\beta}$ is the Kroneker delta tensor.

In this scenario, only shear components of the stress and strain tensor are considered, as the same case dealt in the complex variable method. From equations (6, 7 and 15), the stress state on the lateral surface is given by [22-24]:

$$\sigma_{n3}^{b} = K\frac{d\sigma_{t3}^{b}}{dt}, \tag{55}$$

where σ_{n3}^{b} and σ_{t3}^{b} are the bulk shear stress component at the vicinity of the surface expressed in cylindrical coordinate system with $K = \dfrac{\mu^{0} - \tau^{0}}{R\mu}$.

Eq. (51) shows the calculation of the strain field but it's easier to manipulate the stress field by using Eq. (38). Therefore, an analog form of the stress field is expressed from Eqs. (38) and(51):

$$\sigma_{pq} = \sigma_{pq}^{1} + \sigma_{pq}^{2}, \tag{56}$$

where

$$\sigma_{pq}^{1} = \sigma_{pq}^{1}(\vec{x}, \varepsilon^{*}) = L_{pqij}\left(\int_{V} L_{klmn}\Gamma_{ijkl}(\vec{x}, \vec{y})\varepsilon_{mn}^{*}(\vec{y})dV(\vec{y}) - \varepsilon_{ij}^{*}(\vec{x})\right), \tag{57}$$

$$\sigma_{pq}^{2} = \sigma_{pq}^{2}(\vec{x}, \varepsilon^{s}) = \int_{S} L_{pqij}Q_{ijk}(\vec{x}, \vec{y})\sigma_{kl}^{b}(\tau_{\alpha\beta}^{0}, S_{\alpha\beta\gamma\delta}, \kappa_{\alpha\beta}, \varepsilon^{s}(\vec{y}))n_{l}(\vec{y})dS(\vec{y}). \tag{58}$$

The first part is the stress field due to the dislocation with free surface, which is difficult to be obtained directly from the Green's function method for finite domains. However, it has been obtained alternatively by using the "image dislocation" concept in micromechanics [25]:

$$\sigma_{13}^{1}(\vec{x}) = -\frac{\mu b}{2\pi}\left(\frac{x_2}{(x_1-a)^2+x_2^{\,2}} - \frac{x_2}{(x_1-\frac{R^2}{a})^2+x_2^{\,2}}\right), \tag{59}$$

$$\sigma_{23}^{1}(\vec{x}) = \frac{\mu b}{2\pi}\left(\frac{x_1-a}{(x_1-a)^2+x_2^{\,2}} - \frac{x_1-\frac{R^2}{a}}{(x_1-\frac{R^2}{a})^2+x_2^{\,2}}\right). \tag{60}$$

For the second part in Eq. (58), the Green's function of a cylindrical finite domain should be employed. Unfortunately, the explicit Green's function of finite domains is very difficult to derive and there is no such result available in literatures, so this work made an approximation for the calculation here with the Green's function of an infinite isotropic medium, which is given as:

$$G_{ij}(\vec{x},\vec{y}) = \frac{3-4\nu}{16\pi\mu(1-\nu)}\frac{\delta_{ij}}{\left\|\vec{x}-\vec{y}\right\|} + \frac{1}{16\pi\mu(1-\nu)}\frac{(x_i-y_i)(x_j-y_j)}{\left\|\vec{x}-\vec{y}\right\|^3}, \tag{61}$$

where $\left\|\vec{x}-\vec{y}\right\| = \sqrt{(x_i-y_i)(x_i-y_i)}$.

The derivative of Green's function is obtained as[84]:

$$\begin{aligned} Q_{ijk}(\vec{x},\vec{y}) = \frac{C}{\left\|\vec{x}-\vec{y}\right\|^5}\{&\left\|\vec{x}-\vec{y}\right\|^2[(2\nu-1)(\delta_{ik}(x_j-y_j)+\delta_{jk}(x_i-y_i))+\delta_{ij}x_k] \\ &-3(x_i-y_i)(x_j-y_j)(x_k-y_k)\}. \end{aligned} \tag{62}$$

where $C = \frac{1}{16\pi\mu(1-\nu)}$.

The second stress parts in Eq. (58) should be independent of x_3 coordinate, so take $x_3 = 0$ in the stress expressions. However, they involve with a cumbersome surface integration. Notice that it could be integrated by taking two mirroring piece $dS(\vec{y}) = Rd\theta dy_3$ and $dS'(-\vec{y}) = -Rd\theta dy_3$ (see Figure 23) where $0 \le y_3 \le +\infty$, so first integrate on y_3 and the second stress parts become:

$$\sigma_{13}^2(\vec{x}) = \int_\theta \frac{8\mu CR(\nu-1)(x_1-y_1)}{(x_1-y_1)^2+(x_2-y_2)^2}(\sigma^b{}_{13}\cos(\theta)+\sigma^b{}_{23}\sin(\theta))d\theta, \tag{63}$$

$$\sigma_{23}^2(\vec{x}) = \int_\theta \frac{8\mu CR(\nu-1)(x_2-y_2)}{(x_1-y_1)^2+(x_2-y_2)^2}(\sigma^b{}_{13}\cos(\theta)+\sigma^b{}_{23}\sin(\theta))d\theta, \tag{64}$$

where $\vec{x} \in V$, $\vec{y} \in S$, and $0 \le \theta < 2\pi$.

By combining Eqs. (55), (63) and (64), the final stress field is solved. Take the part of $\sigma_{13}^2(\vec{x})$ for example.

Note $\vec{y} \in S$, let $y_1 = R\cos(\theta), y_2 = R\sin(\theta)$ where $0 \le \theta < 2\pi$; meanwhile, $\vec{x} \in V$, let $x_1 = r\cos(\varphi), x_2 = r\sin(\varphi)$ where $0 \le r \le R, 0 \le \varphi < 2\pi$.

Denote $z = \mathrm{Re}^{i\theta}, z_0 = re^{i\varphi}$, so we have:

$$\sigma_{13}^2(\vec{x}) = \sigma_{13}^2(r,\varphi) = \int_\theta \frac{A((z_0-z)+(\bar{z}_0-\bar{z}))}{(z_0-z)(\bar{z}_0-\bar{z})}(\sigma^b{}_{13}\cos(\theta)+\sigma^b{}_{23}\sin(\theta))d\theta, \tag{65}$$

with $A = 4\mu CR(\nu-1)$.

Rewrite this as two terms:

$$\sigma_{13}^2(r,\varphi) = I_1 + I_2, \tag{66}$$

where

$$I_1 = \int_\theta \frac{A(\sigma^b{}_{13}\cos(\theta) + \sigma^b{}_{23}\sin(\theta))}{z_0 - z} d\theta, \tag{67}$$

$$I_2 = \int_\theta \frac{A(\sigma^b{}_{13}\cos(\theta) + \sigma^b{}_{23}\sin(\theta))}{\bar{z}_0 - \bar{z}} d\theta. \tag{68}$$

In complex analysis, the contour integral can be calculated easily when the integrating function is analytic in the region.

$$\oint \frac{f(z)}{z - z_0} dz = 2\pi i f(z_0). \tag{69}$$

By using $z = \mathrm{Re}^{i\theta}, d\theta = \frac{1}{iz} dz = \frac{1}{-iz} d\bar{z}$, then we get:

$$I_1 = \oint \frac{A(\sigma^b{}_{13}\cos(\theta) + \sigma^b{}_{23}\sin(\theta))}{z_0 - z} \frac{1}{iz} dz = \oint \frac{A(\sigma^b{}_{13}\cos(\theta) + \sigma^b{}_{23}\sin(\theta))}{z_0 - z} \frac{\bar{z}}{iR^2} dz. \tag{70}$$

where $1/z$ is intentionally changed to $\bar{z}/R^2$ because $1/z$ is not analytic at $z = 0$.

Now take

$$f(z) = -A(\sigma^b{}_{13}\cos(\theta) + \sigma^b{}_{23}\sin(\theta)) \frac{\bar{z}}{iR^2}. \tag{71}$$

In this way, we get:

$$I_1 = -\frac{2\pi A(\sigma^b{}_{13}\cos(\varphi) + \sigma^b{}_{23}\sin(\varphi))}{R^2}\bar{z}_0. \tag{72}$$

Similarly,

$$I_2 = -\frac{2\pi A(\sigma^b{}_{13}\cos(\varphi) + \sigma^b{}_{23}\sin(\varphi))}{R^2} z_0. \tag{73}$$

Therefore,

$$\begin{aligned}\sigma^2_{13}(r,\varphi) &= -\frac{2\pi A(\sigma^b{}_{13}\cos(\varphi) + \sigma^b{}_{23}\sin(\varphi))}{R^2}(z_0 + \bar{z}_0) \\ &= -\frac{4\pi Ar\cos(\varphi)(\sigma^b{}_{13}\cos(\varphi) + \sigma^b{}_{23}\sin(\varphi))}{R^2}.\end{aligned} \tag{74}$$

Similarly,

$$\sigma^2_{23}(r,\varphi) = -\frac{4\pi Ar\sin(\varphi)(\sigma^b{}_{13}\cos(\varphi) + \sigma^b{}_{23}\sin(\varphi))}{R^2}. \tag{75}$$

At this stage, the integration procedure is tackled and the rest is only algebraic operation. Set the two stress expressions with $r = R$ for the bulk stress at the vicinity of the surface, and plug them into Eq. (55), which can be written in Cartesian coordinate system:

$$\sigma^{b}{}_{13}\cos(\varphi)+\sigma^{b}{}_{23}\sin(\varphi)=K\frac{d}{d\varphi}(-\sigma^{b}{}_{13}\sin(\varphi)+\sigma^{b}{}_{23}\cos(\varphi)). \tag{76}$$

Setting the obtained formula of σ_{13}^{2}, σ_{23}^{2} in Eqs. (74) and (75) with Eqs. (59) and (60) for the stress at the vicinity of the surface, it can be calculated in the following after some algebraic operations:

$$\frac{d}{d\varphi}(-\sigma^{b}{}_{13}\sin(\varphi)+\sigma^{b}{}_{23}\cos(\varphi))=-\frac{\mu ab\sin(\varphi)(R^2-a^2)}{\pi(R^2+a^2-2Ra\cos(\varphi))^2}. \tag{77}$$

Put Eq. (77) to the second stress parts and the final stress fields are solved:

$$\sigma_{13}=\sigma_{13}^{1}-\frac{ab\sin(\varphi)\cos(\varphi)(R^2-a^2)}{\pi(R^2+a^2-2Ra\cos(\varphi))^2}\frac{r}{R^2}(\mu^0-\tau^0), \tag{78}$$

$$\sigma_{23}=\sigma_{23}^{1}-\frac{ab\sin(\varphi)\sin(\varphi)(R^2-a^2)}{\pi(R^2+a^2-2Ra\cos(\varphi))^2}\frac{r}{R^2}(\mu^0-\tau^0), \tag{79}$$

where σ_{13}^{1} and σ_{23}^{1} are given in Eqs. (59) and (60).

By using complex variable method, Liu and Fang [22] has solved the stress field of a screw dislocation inside an inhomogeneity with interface stress. In their solution, when setting the infinite matrix shear modulus to zero, it's reduced to the result of the current problem:

$$\sigma_{13}=-\frac{\mu b}{2\pi}\frac{x_2}{(x_1-a)^2+x_2{}^2}+\frac{\mu b}{2\pi}\sum_{k=0}^{\infty}\frac{\mu-(1+k)\dfrac{\mu^0-\tau^0}{R}}{\mu+(1+k)\dfrac{\mu^0-\tau^0}{R}}(\frac{a}{R^2})^{k+1}r^k\sin(k\varphi), \tag{80}$$

$$\sigma_{23} = \frac{\mu b}{2\pi}\frac{x_1 - a}{(x_1 - a)^2 + x_2{}^2} + \frac{\mu b}{2\pi}\sum_{k=0}^{\infty}\frac{\mu - (1+k)\dfrac{\mu^0 - \tau^0}{R}}{\mu + (1+k)\dfrac{\mu^0 - \tau^0}{R}}\left(\frac{a}{R^2}\right)^{k+1} r^k(-\cos(k\varphi)). \qquad (81)$$

Eqs. ((78), (79)) and Eqs. ((80), (81)) both disclose that the surface stress indeed plays a role in determining the stress field. The stress profile is changed more obviously near the surface region as the *r*-dependent parts of the solutions show. However, the result of this work can interpret the importance of the surface more straightforwardly, as the stress deviation from the classical part is clearly shown to be proportional to the surface elasticity parameter $\mu^0 - \tau^0$. In Eqs. ((78), (79)), $\sigma^2 / \sigma^1 \sim K = (\mu^0 - \tau^0)/R\mu$ and typically, $\mu^0 - \tau^0 \sim 10N/m, \mu \sim 100GPa, R \sim 10nm$, then $K \sim 0.01$.

Results

To compare the results obtained in this work and the complex variable method, the stress field is plotted along different paths of the nanowire (Figure 24): (i) x_1-axis; (ii) x_2-axis; (iii)a general path through the center oriented at angle φ; (iv) the outer circle. The shear modulus for a general crystal is set as $\mu = 50GPa$. The surface elastic constants for a general solid surface are obtained by atomistic simulations and the magnitude of $\mu^0 - \tau^0$ is between $-10N/m$ and $10N/m$ [83, 85]. In this work, the surface elastic constant is set as $\mu^0 - \tau^0 = 6N/m$. The dislocation offset to the center is set as $\delta = a/R = 0.5$.

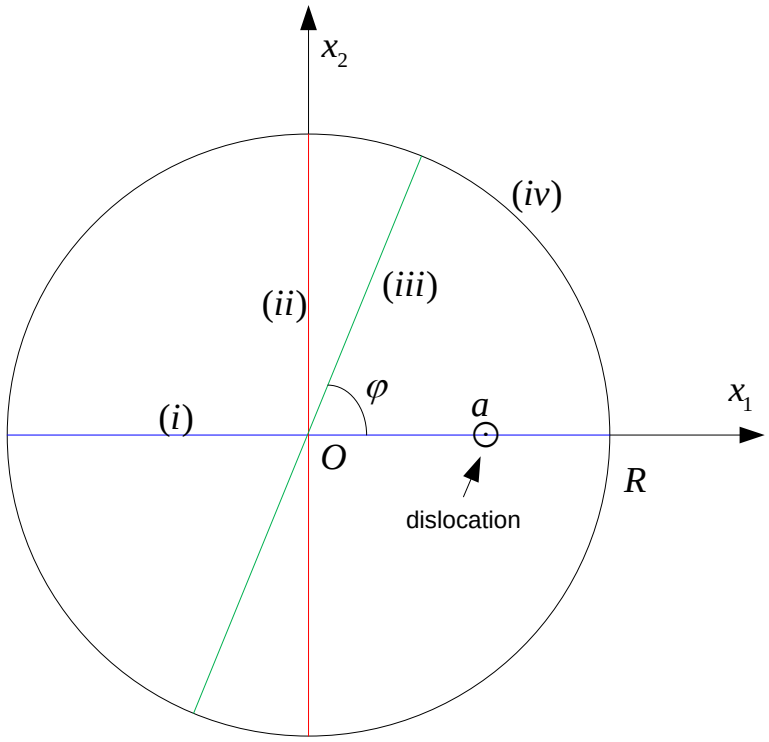

Figure 24. Cross section view of the nanowire with a screw dislocation

The classical stress solutions without surface stress are taken from Eqs. ((59), (60)), and the solutions of the complex variable method are from Eqs. ((80), (81)), while the results of this work are from Eqs. ((78), (79)).

Figure 25 shows the stress fields for two nanowires with distinct sizes along path (i): x_1-axis. The nanowire of $R = 100nm$ (Figure 25b) is large enough to neglect the effect of the surface stress compared to the nanowire of $R = 1nm$ (Figure 25a). However, along this special path, the stress values are not quite different for both cases. This could be predicted directly from the analytical results of this work when setting $\varphi = 0, \pi$ in Eqs. ((78), (79)).

Figure 26 shows the stress fields along path (ii): x_2-axis. The stress component of σ_{13} for both nanowires in this work is identical to the classical solution because $\varphi = \pi / 2$ in Eq. (78) along this special path. As for the stress component of σ_{23}, it is just

slightly different from the classical result for the nanowire with $R = 1nm$ (Figure 26a), and it becomes the same with the classical result as the surface effect should be negligible when the size of the structure becomes sufficiently large. However, the result of σ_{23} from the complex variable method is quite different from the classical result in both nanowires. This means its stress field is still largely affected by the surface stress, which deviates from the sense that surface stress should be negligible in sufficiently large structures, although its result of σ_{13} corresponds to the classical result as expected in the nanowire with $R = 100nm$ and shows a little difference in the nanowire with $R = 1nm$ due to the surface stress.

Figure 27 shows the stress fields along a general path through the center oriented. For example, one path is picked up at angle $\varphi = 60^{\circ}$. All the results behave similarly to the situation on path (ii). The stress component of σ_{23} from complex variable method still differs largely from the classical solution in the nanowire with $R = 100nm$, while the result of this work agrees well with the classical solution in this case. In addition to that, the stress solutions for the nanowire with $R = 1nm$ in this work also show noticeable differences from the classical solutions compared to the tiny differences in Figure 26. This means the stress deviation from the classical results duo to surface stress is not uniform in different domains of the nanowire, and this deviation becomes more significant as it approaches to the surface of the nanowire. This could be easily seen and confirmed in Eqs. ((78), (79)) as the second stress part due to surface stress is proportional to *r*.

Figure 28 shows the stress fields along the outer circle. The solutions of this work demonstrate obvious differences from the classical solutions in the nanowire with $R = 1nm$, while they maintain good agreements with one another in the nanowire with $R = 100nm$. On the other hand, the stress component of σ_{23} from complex variable method still conflicts from the classical result when the size of the nanowire becomes

sufficiently large. From Figure 28a, it is also interesting to see that the stress differences between with and without surface stress are most obviously seen in the region of $20^{\circ} \sim 50^{\circ}$ and the symmetric region of $310^{\circ} \sim 340^{\circ}$. This looks very hard to tell from the solutions of complex variable method (Eqs. ((80), (81))), but it could be predicted from the solutions of this work (Eqs. ((78), (79))) thanks to their explicit analytical expressions.

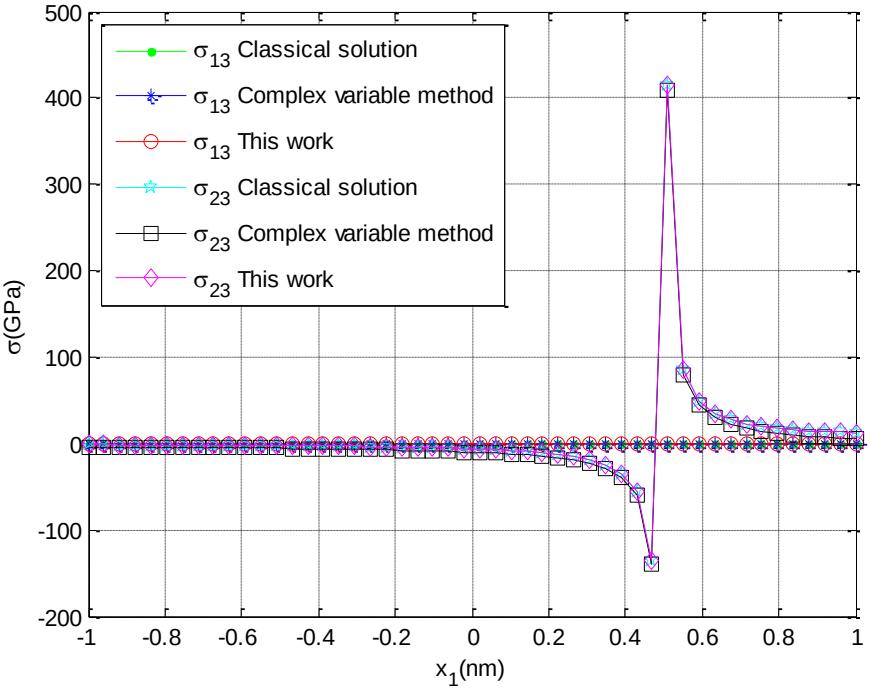

(a)

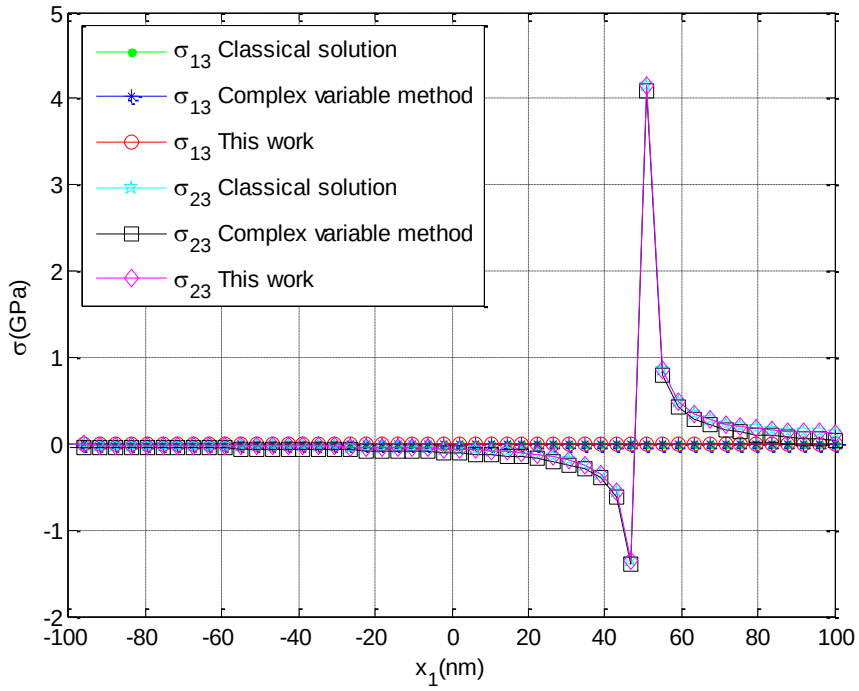

(b)

Figure 25. Stress fields along x_1 –axis (a. R = 1 nm; b. R = 100 nm)

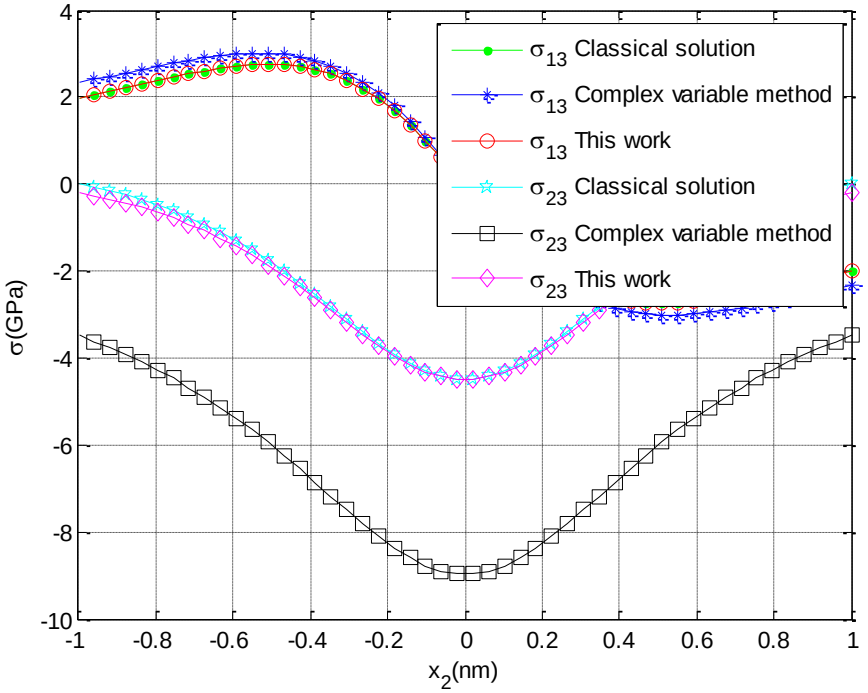

(a)

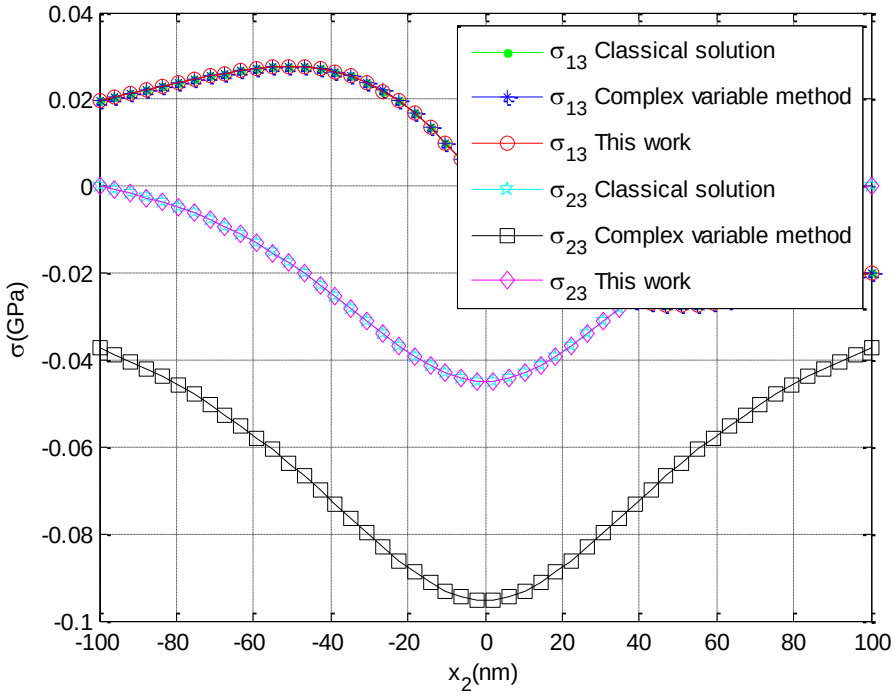

(b)

Figure 26. Stress fields along x_2 –axis (a. R = 1 nm; b. R = 100 nm)

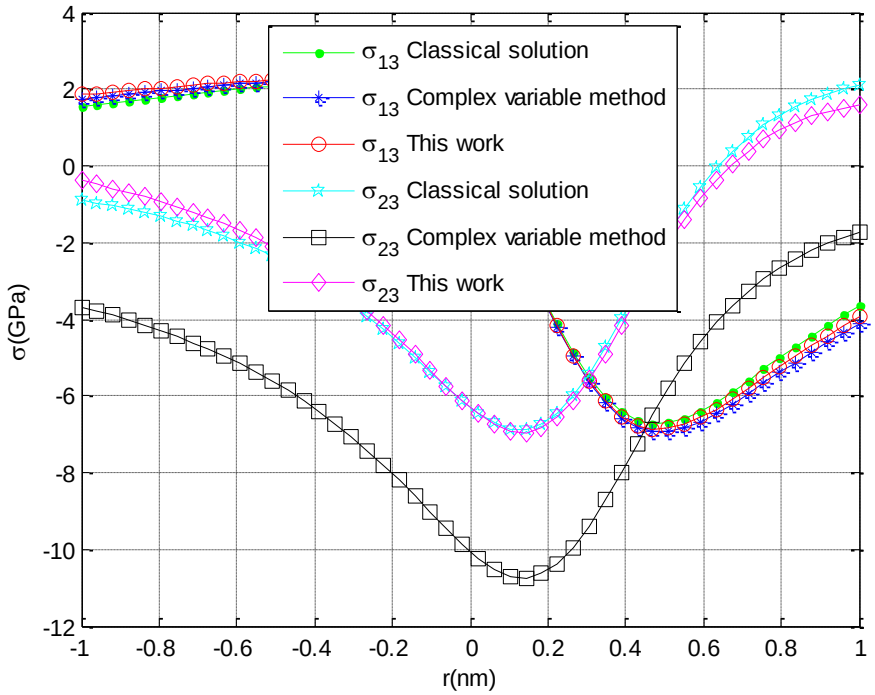

(a)

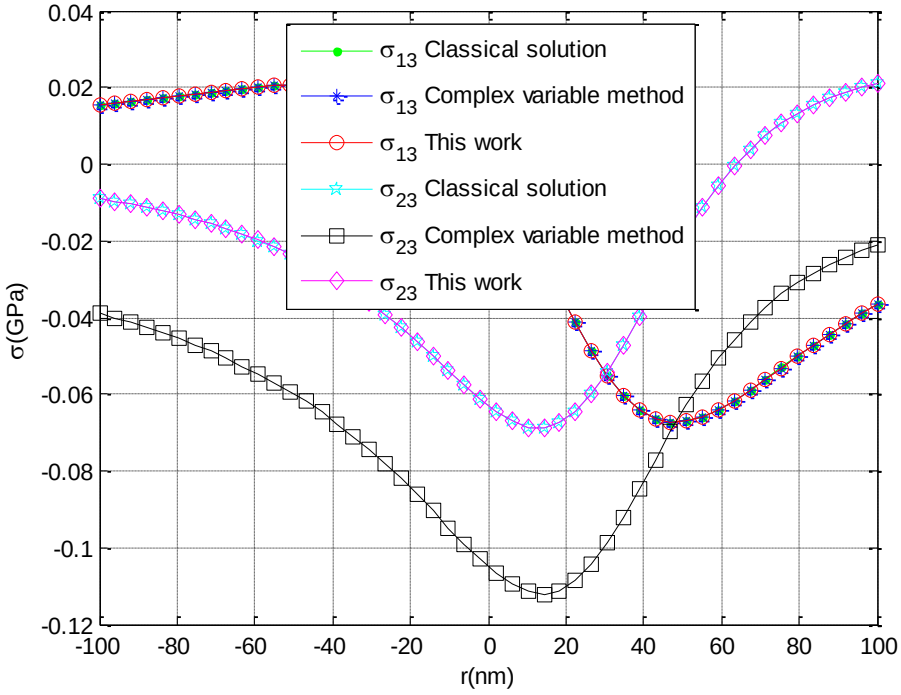

(b)

Figure 27. Stress fields along a path through the center (a. R = 1 nm; b. R = 100 nm)

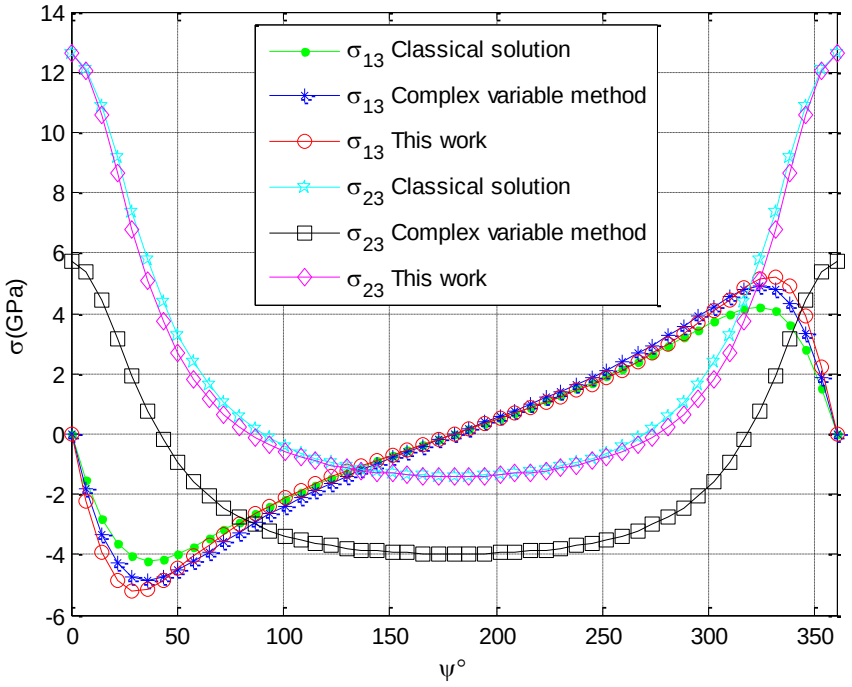

(a)

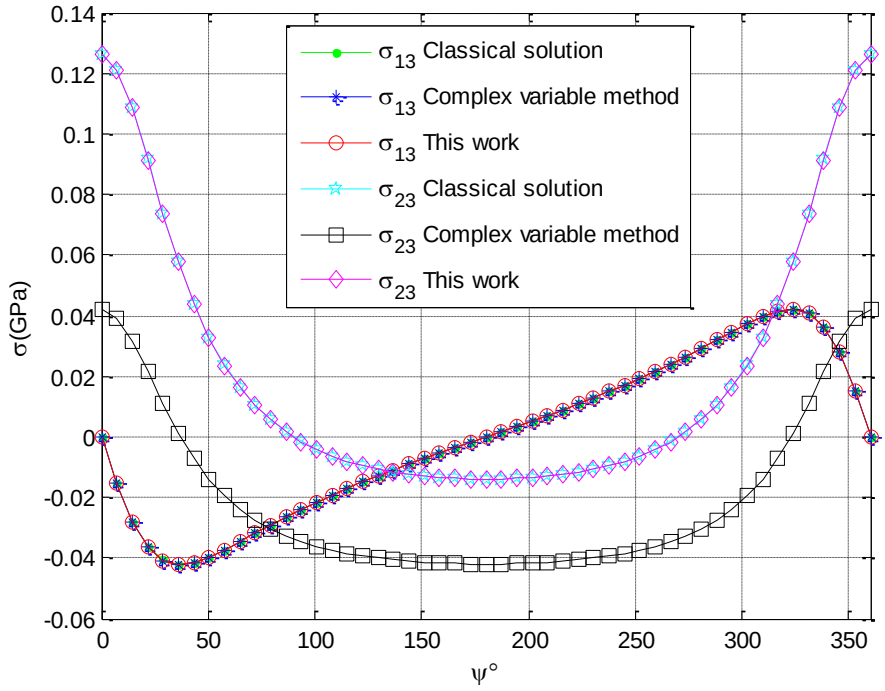

(b)

Figure 28. Stress fields along the outer circle (a. R = 1 nm; b. R = 100 nm)

The current result for nanowires is considered as a validation of the proposed analytical framework. This framework could be applied to more general situations compared to complex variable method which is mainly used for 2D isotropic cases. The solution in this work is given in explicit form, while the solution from complex variable method is provided in form of power series, which is not flexible to manipulate in further development. Comparing Eqs. ((78), (79)) and Eqs. ((80), (81)), the effect of surface property parameters on the stress field can be predicted more easily and straightforwardly from our solution. Concerning the result, σ_{13} components of our solution and complex variable method are close to each other and they both agree well with the classical result. σ_{23} components of our solution and complex variable method are different in magnitude, but they behave quite similarly in the changing trend. More favorably, our solution overlaps with the classical result for large nanowires but the solution of complex variable method deviates obviously from it.

Discussions

As seen in the numeric results, the stress fields could be altered by the surface stress significantly in the nanowire. This is reflected in the second stress part of Eqs. ((78), (79)) of this work. Essentially, either the solutions of this work or complex variable method attempt to take account for the interaction between the dislocation and the lateral surface. Obviously, this behavior should be size-dependent, i.e., when the radius of the nanowire shrinks, the stress difference ($\sigma_{13}^2, \sigma_{23}^2$) should be more significant. Besides of that, the influence of this interaction could also vary when the location of the dislocation or the surface elastic properties changes.

Figure 29 shows the size-dependent stress differences change with the nanowires with varied radii. The stress differences are expected to be much larger when the radius of the nanowire goes below $10nm$, and they also drop dramatically when the radius is

above $50nm$. In fact, since the surface constants of a typical crystal are between $-10N/m$ and $10N/m$, the contribution of the surface stress could be safely neglected for structures of their dimensions higher than $50nm$.

Figure 30 shows the stress differences changes when the location of the dislocation changes in the same nanowire and with the same surface elasticity. It is clearly shown that the interaction between the dislocation and the lateral surface becomes stronger when the dislocation approaches the surface. From this tendency, the stress differences will evolve into a spike when the dislocation is at the vicinity of the surface.

Figure 31 shows the stress differences changes with different surface elasticity parameters. In practical situations, the surface constant $\mu^0 - \tau^0$ could be positive or negative, but its magnitude is usually between $-10N/m$ and $10N/m$. From the analytical solutions of Eqs. ((78), (79)) in this work, the stress differences are proportional to $\mu^0 - \tau^0$, which is also seen in Figure 31. However, as seen in Eq. (47), there are also some other independent parameters to determine the surface elasticity, but they are not present in the formulations of this work or the complex variable method. This is because the current problem is limited to the shear stress field analysis of an infinite isotropic nanowire. Physically, when the surface stress is concerned, probably it could also induce some tensile deformation on the surface. After this tensile effect is taken into consideration, the complete set of surface elasticity parameters will be included in the formulation and the stress result will be better refined.

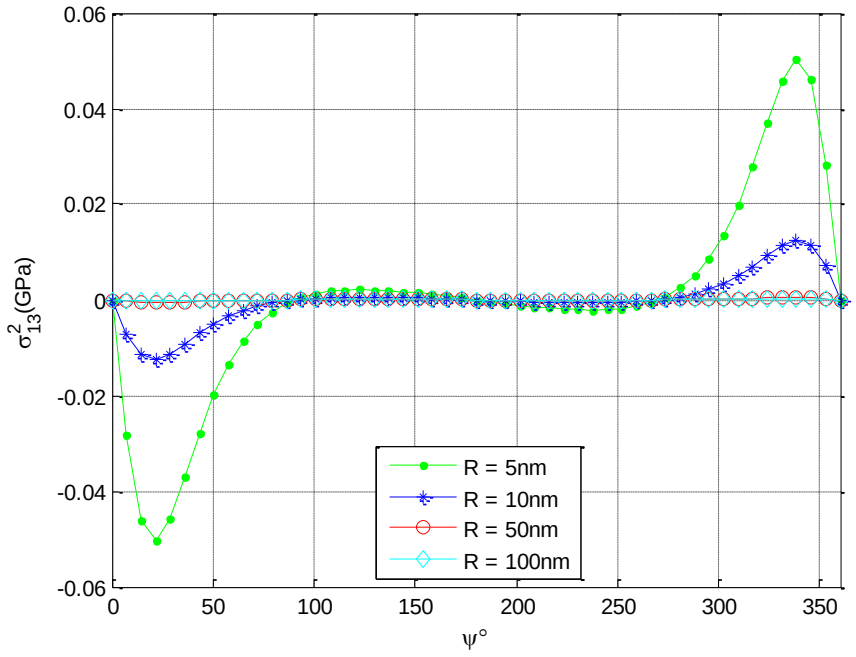

(a)

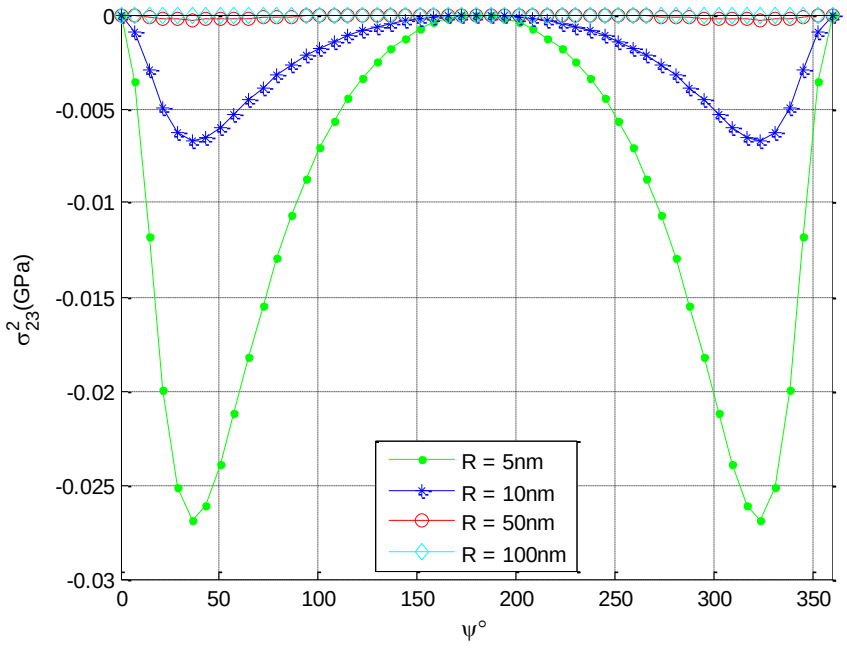

(b)

Figure 29. Stress differences changes when the size of the nanowire changes (a. σ^2_{13}; b. σ^2_{23})

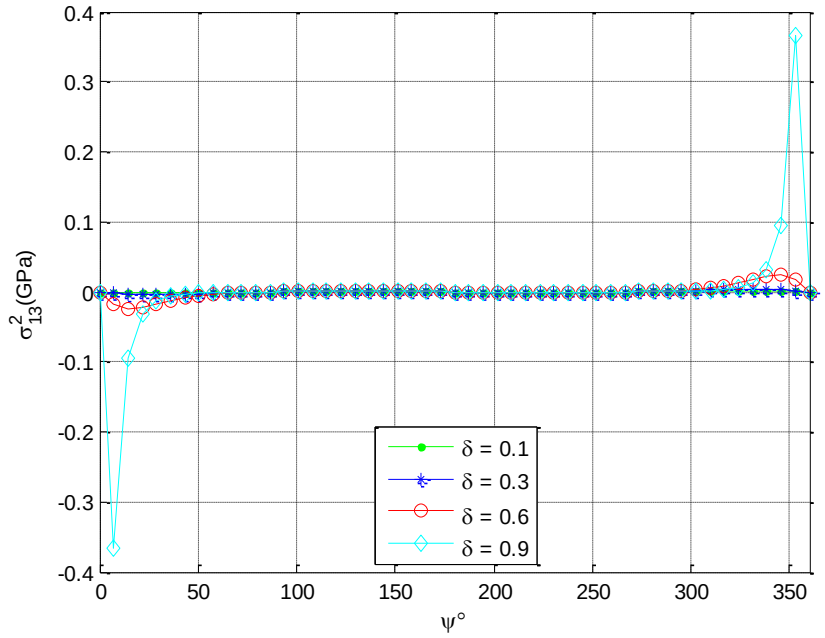

(a)

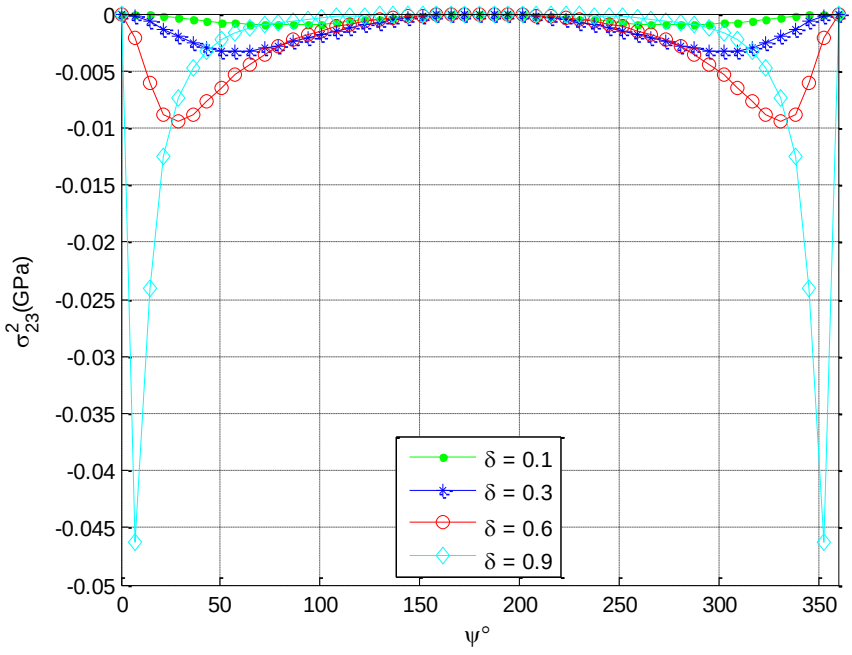

(b)

Figure 30. Stress differences changes when the location of the dislocation changes (a. σ^2_{13}; b. σ^2_{23})

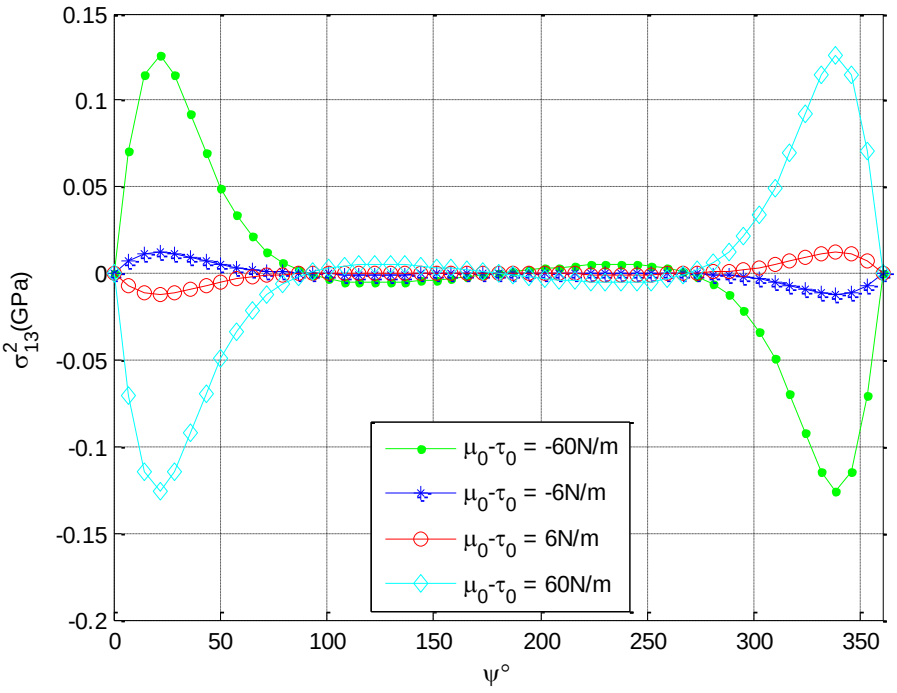

(a)

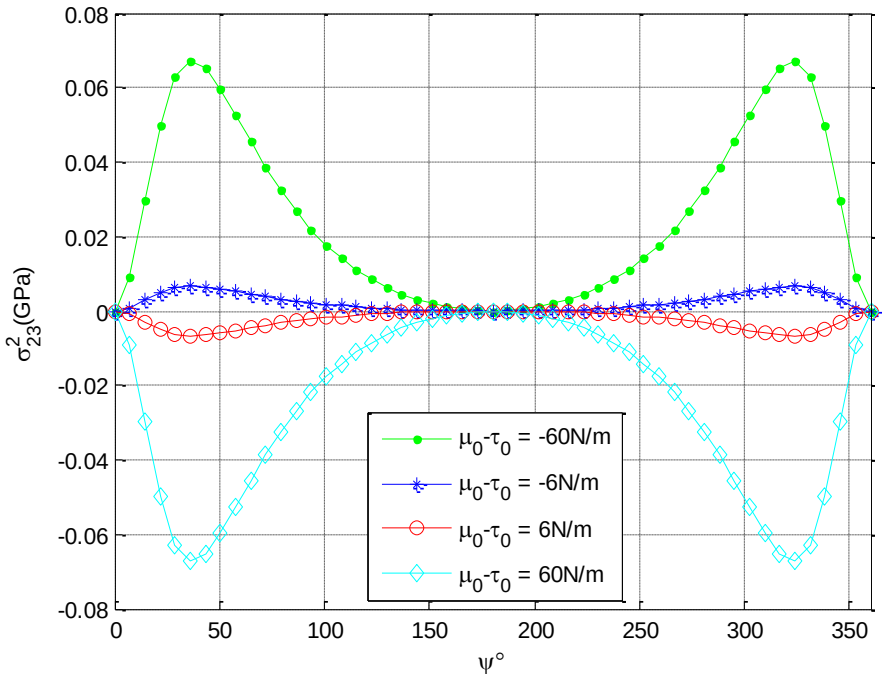

(b)

Figure 31. Stress differences changes when the surface elasticity changes (a. σ^2_{13}; b. σ^2_{23})

Analytical Formulation of Image Force

With the stress solutions, the image force could be obtained through the energy method. The total energy per unit length of the nanowire is given as:

$$W = W_b + W_s, \tag{82}$$

where W_b is the elastic strain energy stored in the bulk material, and W_s is the surface excess energy.

In continuum mechanics, the bulk elastic strain energy per unit length is:

$$\begin{aligned} W_b &= \int_S \frac{1}{2}\sigma_{ij}\varepsilon_{ij} ds \\ &= \int_S \frac{1}{2\mu}[(\sigma_{13})^2 + (\sigma_{23})^2] ds \\ &= \int_S \frac{1}{2\mu}[(\sigma_{13}^1)^2 + (\sigma_{23}^1)^2 + (\sigma_{13}^2)^2 + (\sigma_{23}^2)^2 + 2\sigma_{13}^1\sigma_{13}^2 + 2\sigma_{23}^1\sigma_{23}^2] ds. \end{aligned} \tag{83}$$

which can be rewritten as three parts:

$$W_b = W_1 + W_2 + W_3, \tag{84}$$

where

$$W_1 = \int_S \frac{1}{2\mu}[(\sigma_{13}^1)^2 + (\sigma_{23}^1)^2] ds \tag{85}$$

$$W_2 = \int_S \frac{1}{2\mu}[2\sigma_{13}^1\sigma_{13}^2 + 2\sigma_{23}^1\sigma_{23}^2] ds \tag{86}$$

$$W_3 = \int_S \frac{1}{2\mu}[(\sigma_{13}^2)^2 + (\sigma_{23}^2)^2]ds \tag{87}$$

The corresponding image force contribution (f_1, f_2, f_3) due to these three parts can be obtained from the energy method of Eq. (11). Note that W_1 is the same energy of the classical case of free surfaces, so f_1 is the same as the image force of the classical situation[25, 86]:

$$f_1 = \frac{\mu b^2}{2\pi}\frac{a}{R^2 - a^2} \tag{88}$$

After tedious calculations, the other two parts are obtained as:

$$\begin{aligned} f_2 = &-\frac{b^2(\mu^0 - \tau^0)}{\left(a^4 - 2R^2a^2 + R^4\right)R^5a^5\pi}[\left(4\ln\left(a+R\right) - 8\ln\left(R\right) + 4\ln\left(R-a\right)\right)R^{12} \\ &+\left(-8\ln\left(R-a\right)a^2 - 8\ln\left(a+R\right)a^2 + 16\ln\left(R\right)a^2 + 4a^2\right)R^{10} \\ &+\left(4\ln\left(R-a\right)a^4 + 4a^4\ln\left(a+R\right) - 6a^4 - 8a^4\ln\left(R\right)\right)R^8 \\ &+2R^6a^6 - a^7R^5 + \left(4a^8\ln\left(a+R\right) - 2a^8 - 4a^8\ln\left(a\right)\right)R^4 + 7a^9R^3 \\ &+\left(2a^{10} + 8a^{10}\ln\left(a\right) - 8a^{10}\ln\left(a+R\right)\right)R^2 - 4Ra^{11} - 4a^{12}\ln\left(a\right) + 4a^{12}\ln\left(a+R\right)] \end{aligned} \tag{89}$$

$$f_3 = -\frac{ab^2\left(R^4 + a^4 + 4R^2a^2\right)}{4\pi\mu\left(R^2 - a^2\right)^4}(\mu^0 - \tau^0)^2 \tag{90}$$

On the other hand, the surface excess energy per unit length of the nanowire is given as:

$$W_s = \int_s \Gamma ds = \int_s (\Gamma_0 + \Gamma^{(1)} : \varepsilon^s + \frac{1}{2}\varepsilon^s : \Gamma^{(2)} : \varepsilon^s) ds \tag{91}$$

The corresponding image force contribution due to the surface excess energy is:

$$f_4 = -\frac{\partial W_s}{\partial a} = -\int_s (\Gamma_{ij}^{(1)} \frac{\partial \varepsilon_{ij}^s}{\partial a} + \Gamma_{ijkl}^{(2)} \frac{\partial \varepsilon_{ij}^s}{\partial a} \varepsilon_{kl}^s) ds \tag{92}$$

From Eqs. (47) and (54), it can be simplified to:

$$f_4 = -\int_s \frac{1}{2(\mu^0 - \tau^0)} \frac{\partial \varepsilon_{ij}^s}{\partial a} \varepsilon_{ij}^s ds \tag{93}$$

where ε_{ij}^s is the same with the bulk strain for coherent surfaces and the bulk strain can be obtained from the known stress field.

Plugging in our analytical stress solutions and Hooke's Law, we obtain the last image force part:

$$f_4 = -\frac{Rab^2(\mu^0 - \tau^0)}{\pi\left(a^4 - 2R^2a^2 + R^4\right)} \tag{94}$$

Finally, we obtain the analytical solution to the image force of isotropic circular nanowire:

$$f = f_1 + f_2 + f_3 + f_4. \tag{95}$$

When the surface elasticity is set to zero, our solution is reduced to the classical solution in Eq. (88). By contrast, the image force solution of complex variable method is given from Eqs. (80) and (81) as infinite power series[22]:

$$f = \frac{\mu b^2}{2\pi} \sum_{k=0}^{\infty} \frac{\mu - (1+k)\dfrac{\mu^0 - \tau^0}{R}}{\mu + (1+k)\dfrac{\mu^0 - \tau^0}{R}} \frac{a^{2k+1}}{R^{2k+2}}. \tag{96}$$

It can be seen directly that Eq. (96) has the problem with the denominator when the surface elasticity $\mu^0 - \tau^0$ becomes negative, which makes it close to zero for a certain *k* value. This will lead the solution of complex variable method to abrupt fluctuations and to avoid this instability, summation terms need to be selected carefully.

Figure 32 shows the image forces of dislocation inside an isotropic nanowire obtained from our analytical framework and complex variable method. For the case of negative surface elasticity, our solution agrees well with that of complex variable method and both solutions shows obvious deviations to the classical solution when the size of the nanowire is below 10 nm. The image force also behaves as expected for the nanowire with a large size as it almost overlaps on the classical one. This means the surfaces stress only plays an important role in determining the image force in nano-scale and it can be negligible in macro-scale. However, for the case of positive surface elasticity, our solution shows a different tendency as the image force abruptly goes to negative values and this tendency seems opposite to that of complex variable method.

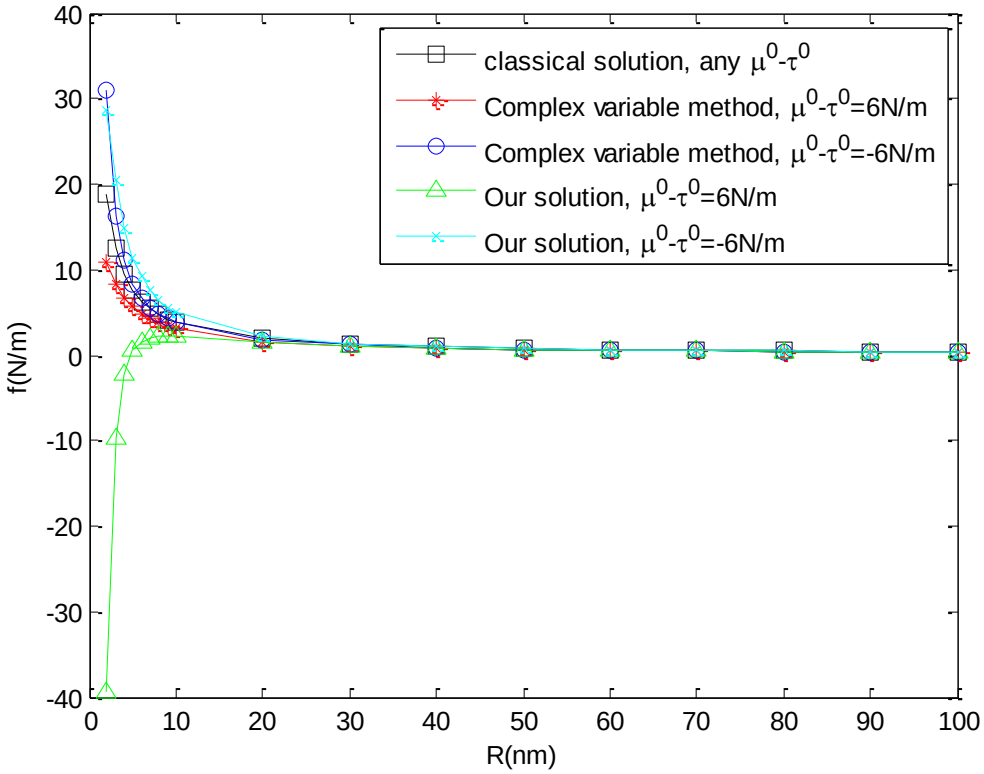

Figure 32. Image forces of dislocation inside an isotropic nanowire

However, after a deeper investigation, it is found out that our solution with positive surface elasticity only drops when the dislocation offset is close to the surface and the radius of the nanowire is below 5 nm (Figure 33).

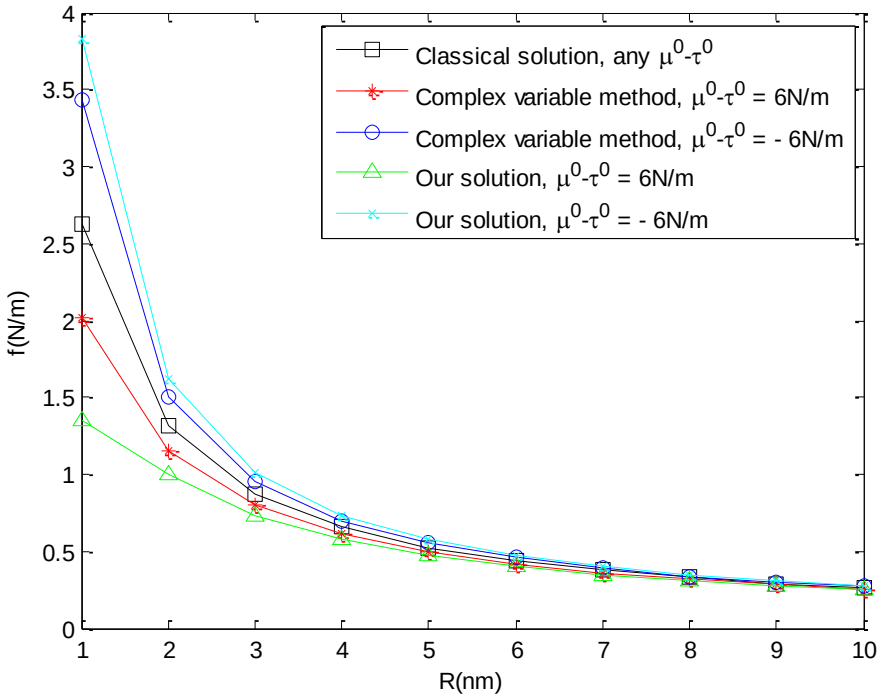
Classical solution, any μ^0-τ^0
Complex variable method, μ^0-τ^0 = 6N/m
Complex variable method, μ^0-τ^0 = - 6N/m
Our solution, μ^0-τ^0 = 6N/m
Our solution, μ^0-τ^0 = - 6N/m
f(N/m)
R(nm)
0
0.5
1
1.5
2
2.5
3
3.5
4
1
2
3
4
5
6
7
8
9
10

(a)

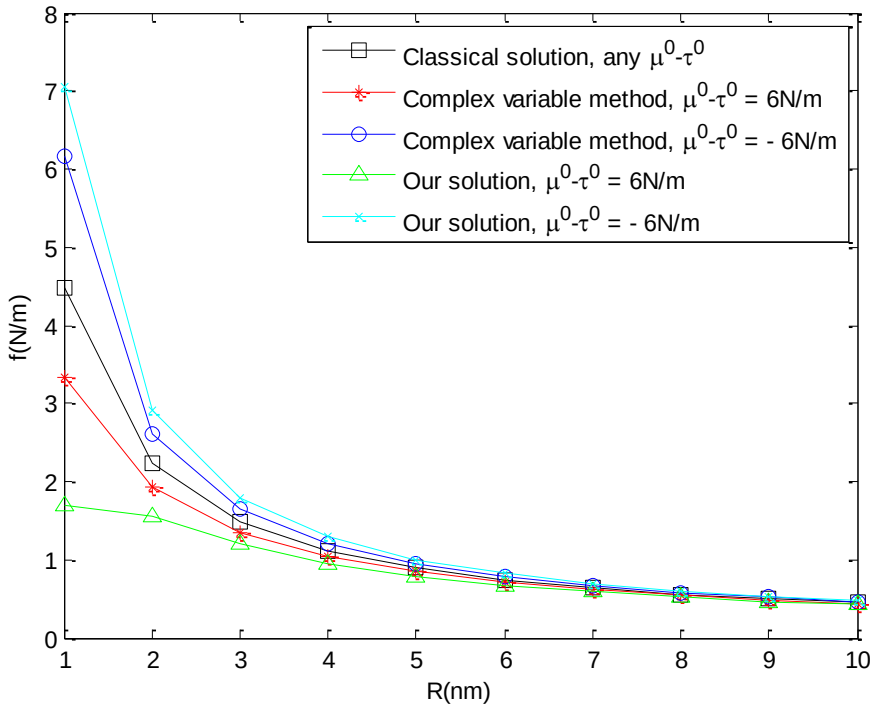
Classical solution, any μ^0-τ^0
Complex variable method, μ^0-τ^0 = 6N/m
Complex variable method, μ^0-τ^0 = - 6N/m
Our solution, μ^0-τ^0 = 6N/m
Our solution, μ^0-τ^0 = - 6N/m
f(N/m)
R(nm)
0
1
2
3
4
5
6
7
8
1
2
3
4
5
6
7
8
9
10

(b)

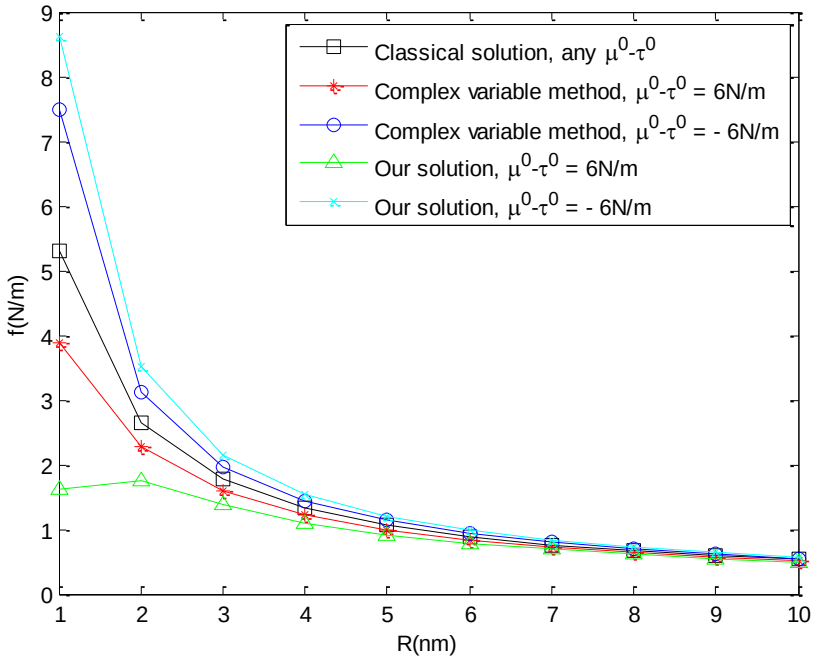

(c)

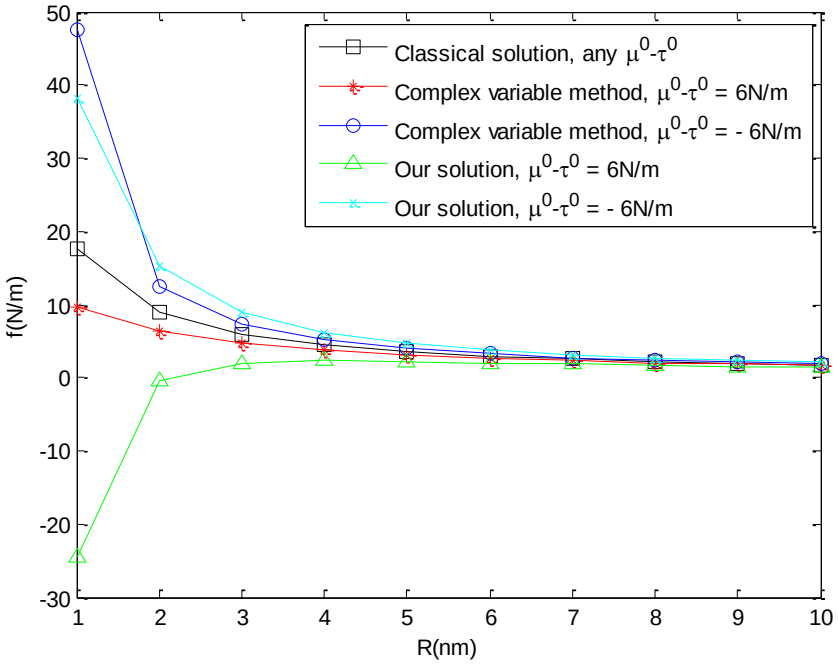

(d)

Figure 33. Image forces of dislocation inside an isotropic nanowire with different offsets

(a. $\delta = 0.3$; b. $\delta = 0.45$; c. $\delta = 0.5$; d. $\delta = 0.8$)

The calculation of image force for dislocations with surface stress is still an open question due to the lack of sufficient collaborations to validate different approaches. The complex variable method shows good results of image forces compared with the classical ones, but it is derived from the stress field of Eqs. (80) and (81), which is proven to be against the common sense of mechanics in case of large nanowires. On the other hand, our work provides an alternative solution to the image force based on the proposed analytical framework. The stress field has been checked to be agreeable to the classical one and it also has good correspondence with the result of complex variable method, although one stress component has a different magnitude from that. Our solution of image force is also acceptable but it has some deviations for the case of positive surface elasticity.

CHAPTER 6

MULTI-SCALE DESIGN OF NANO-EPITAXY

This chapter will adopt the outcome from Chapter 2 to Chapter 5 for fulfilling the objectives and goals of this work. First the image force of dislocations in anisotropic 3D nanorods will be obtained by extending the solution of nanowires in Chapter 5 to incorporate the 3D shape effect. Anisotropic effect will be discussed thereafter. Finally, this work will apply the knowledge to the practical application of GaN nano-epitaxy. A comprehensive parametric study of dislocations in GaN nanorods will be carried out, and thus the geometrical parameters could be optimized to fabricate dislocation-free nanostructures. This knowledge could be used to provide guidelines to the experimental process or fabrication technology in the next-generation nano-epitaxy.

Image Force of Dislocations in Anisotropic Finite Cylinders

In Chapter 5, our framework provides a complete analytical formulation for a general 3D domain of defected material with elastic anisotropy. In practice, the analysis of materials could start from the simplest case of isotropic 2D solids with surface effect, followed by extending isotropic materials to anisotropic materials. This can be implemented by plugging the corresponding anisotropic tensors into the formulation. On the other hand, the proposed analytical framework should have the flexibility to take 3D structures of solids, which could be adjusted to fit into various situations (finite cylinders, nanodots with a cap, etc). The ultimate target is to provide a promising solution to the analysis and design of general anisotropic materials with 3D shapes.

As a starting point, this work has obtained the close-form solutions to the stress fields of an infinite isotropic nanowire and compared with those of complex variable method. It can be also considered to consolidate the current analytical framework. Since

the surface stress is included, it is also capable to deal with nanostructures which may have quite different behaviors from conventional materials. In this way, the framework of this work could be applied to multi-scale studies of materials and bridge up other models developed for different dimensional scales of solids.

3D Shape Effect

To study the 3D shape effect, take the different shapes of GaN nanorods in

Figure 8, the volume and surface integrals in Eq. (56) are both dependent on three coordinates compared to the simpler case of two coordinates in nanowires. In addition to that, Eq. (56) is an implicit equation and the unknowns are also functions of three coordinates. Therefore, it is not feasible to obtain the exactly analytical solution to the elastic field of solids with dislocations embedded in such 3D isotropic materials. However, based on the available image force data from our finite element analysis, it is possible to expand the solution of nanowire in Chapter 5 to 3D finite cylinder case by approximating the 3D shape effect as a height dependent function.

Let us denote the image force of the isotropic circular nanowire by f_0 and that of the isotropic finite cylinder (nanorod) by f. When the two structures have the same radius R, the two image forces should behave as shown in Figure 34.

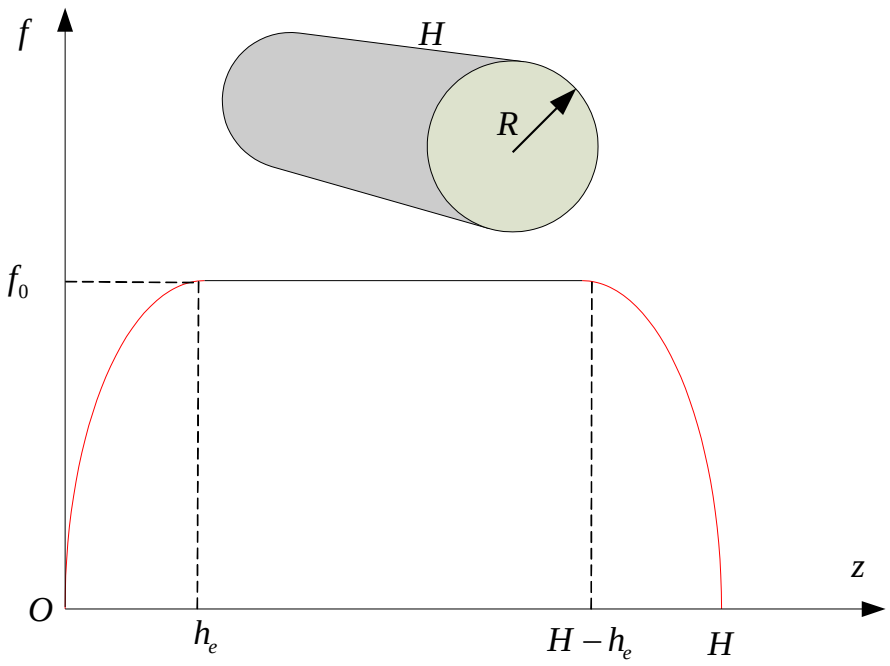

Figure 34. Image forces of nanowire and finite cylinder (nanorod)

According to St. Venant's principle, the surface effect of the two ends in the nanorod will only penetrate to a distance of order R, which is denoted as the effective length, h_e. Beyond the effective region, the image forces of the nanowire and nanorod should be identical in the middle region. As an approximation, when we take the image force of the nanowire from our framework, the corresponding one of 3D nanorod could be determined as:

$$f = f_0 \times g(z), \tag{97}$$

where $g(z)$ is a height dependent shape function that only consists z coordinate.

In principle, the shape function of a particular nanorod should be distinct, which could be influenced by the geometry of the nanorod (radius and height), the material anisotropic orientation and even the consideration of surface stress. To simplify the

analysis, we only take account the geometrical feature for the shape function in this work. In the following, we will obtain the shape function of the image force by curve fitting the finite element data, and this same shape function will be adopted for further study with surface stress.

In Chapter 3, we have performed a comprehensive study of the dislocation dissipation by image forces in solids due to the effect of free surfaces. This study provides all the image force curves for nanorods with different radius and height. Since the finite element analysis is based on the formulation of free surfaces, its image force magnitude of the middle region should be adjusted to the value of the analytical solution without surface stress.

Figure 35 shows the image forces for three groups of nanorods with five different ratios between radius and height respectively. Each group keeps the radius of the nanorod as a constant. It is quite straightforward to notice the plateau of the image force in the middle region of the nanorod when the height of the nanorod is obviously larger than the radius. Even for the case of short nanorods, the maximum image force at the middle point is consistent with the longer nanorods. The comparison of the maximum image force in finite element analysis with the image force of nanowires calculated in analytical solution is listed in Table 6.

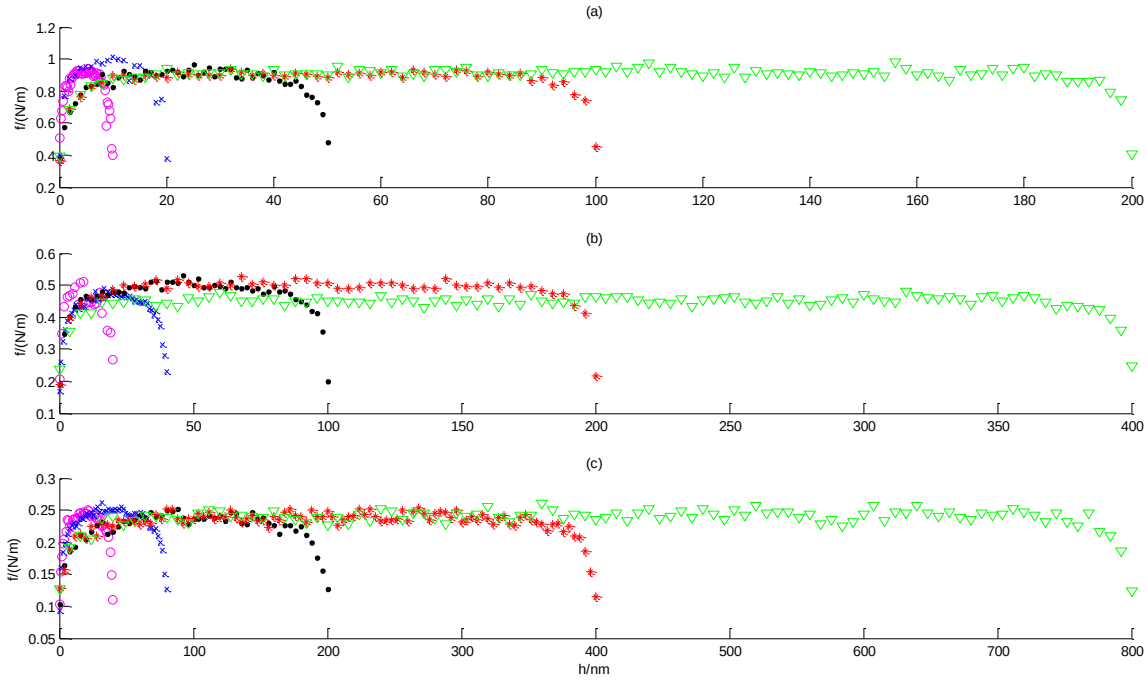

Figure 35. Image forces for nanorods with different radius and height

Table 6 shows that there are some deviations between the finite element analysis and classical analytical solution although both of them are calculated in the case of neglecting surface stress. This might arise from the approximations made to facilitate the calculation of image forces in each approach. However, the ratio of the two results is quite consistent when the radius changes. In this way, we can add the average ratio value as a correction factor to Eq. (97). For our case, the correction factor is set to $\gamma = 1.797$.

Table 6. Comparison of image forces in finite element analysis and analytical solution

r	FEM result	Classical analytical result	Ratio
10	0.9	0.5305	1.696
20	0.5	0.2653	1.885
40	0.24	0.1326	1.810

Another important quantity to be determined from the finite element data in Figure 35 is the effective length, h_e. It is instinctive to assume that the effective length should be proportional to the radius of the nanorod, since the shortest distance of the dislocation from the lateral free surface is close to R. In Figure 35, the ratio of the effective length to the radius for long nanorods ($H > 4R$) is found to be constant, and then the effective length could be determined as:

$$h_e = 2R. \tag{98}$$

For the case of short nanorods ($H < 4R$), the effective length is simply set to:

$$h_e = \frac{H}{2}. \tag{99}$$

The shape function to be determined in Eq. (97) should be agreeable to the curve trend shown in Figure 35, which is also schematically shown in Figure 34. The shape function at the initial stage ($z < h_e$) of the left end behaves quite similarly to an exponential function. In the plateau of the middle region, it can be simply set to 1 because

the image force of the nanorod overlaps with that of the nanowire. The region of the right end is symmetric with the left end. At last, it is sufficient to describe the shape function just with the region at the initial stage ($z < h_e$) of the left end, which could be proposed as a general exponential function:

$$g(z) = ae^{bz} + c, \tag{100}$$

where *a*, *b* and *c* are the unknown variables to be fitted with the finite element data.

Table 7 shows the curve fitting results of the shape function. For all the nanorods of different radius and height, the fitted values of *a*, *b* and *c* are consistent and the R-square values are also acceptable.

Table 7. Curve fitting of the shape function

r	***h***	***a***	***b***	***c***	**R-square**
	50	-0.5574	-3.6580	0.9936	0.9728
10	100	-0.5762	-4.0310	0.9964	0.9878
	200	-0.5365	-3.9540	0.9792	0.9947
	100	-0.5922	-6.0360	0.9990	0.9695
20	200	-0.5851	-4.8300	0.9582	0.9785
	400	-0.4846	-4.0210	1.0280	0.9855
	200	-0.5022	-3.8250	0.9693	0.9345
40	400	-0.4399	-3.7800	0.9823	0.9522
	800	-0.4459	-3.3160	0.9870	0.9467
Average:		-0.5244	-4.1612	0.9881	0.9691

The obtained shape function is obtained by fitting the classical analytical solution to the finite element data without surface stress. As for obtaining the shape function with surface stress, unfortunately there is no collaboration result from literatures. In Chapter 2, this work has demonstrated the possibility to incorporate surface effect into the current finite element model of dislocations in solids, but it would take some effort to implement the surface stress in Eqs. (45), (46) and (47) numerically, which might involve designing a novel surface element type and connecting it to the neighboring bulk element. However, for the present, this work directly adopts the shape function obtained for the case without surface stress and applies it to the case with surface stress. Therefore, the final analytical solution to the image force for 3D isotropic finite cylinder is given as:

$$f = \gamma f_0 \times g(z), \tag{101}$$

where γ is the correction factor by calibrating with the finite element data; f_0 is the corresponding image force of the nanowire with surface stress and it has been provided by Eq. (95); $g(z)$ is the shape function consisting of only z coordinate and it is given in Eq. (100) by curve fitting of the finite element data.

Figure 36 shows the comparison of image forces in 3D isotropic nanorods between the original finite element result without surface stress and the analytical results with and without surface stress. Although the finite element result has some fluctuations due to the precision of the numerical calculation, it agrees well with the analytical result without surface stress. This turns out to be as expected since the shape function is fitted to the original finite element data. In case that surface stress is considered, image forces generally increase for negative surface elasticity and decrease with positive surface elasticity. In this case, the surface with negative surface elasticity resembles a “soft”

media compared to the bulk material and it becomes “rigid” with positive surface elasticity. It can be also seen from Figure 36 that surface stress plays a more important role in thinner nanorods (R = 10 nm) and it diminishes as the radius of the nanorod increases. In fact, surface stress has only a little contribution to the final image force when the radius of the nanorod is around 50 nm and above. This is also seen in the case of nanowires in Figure 32.

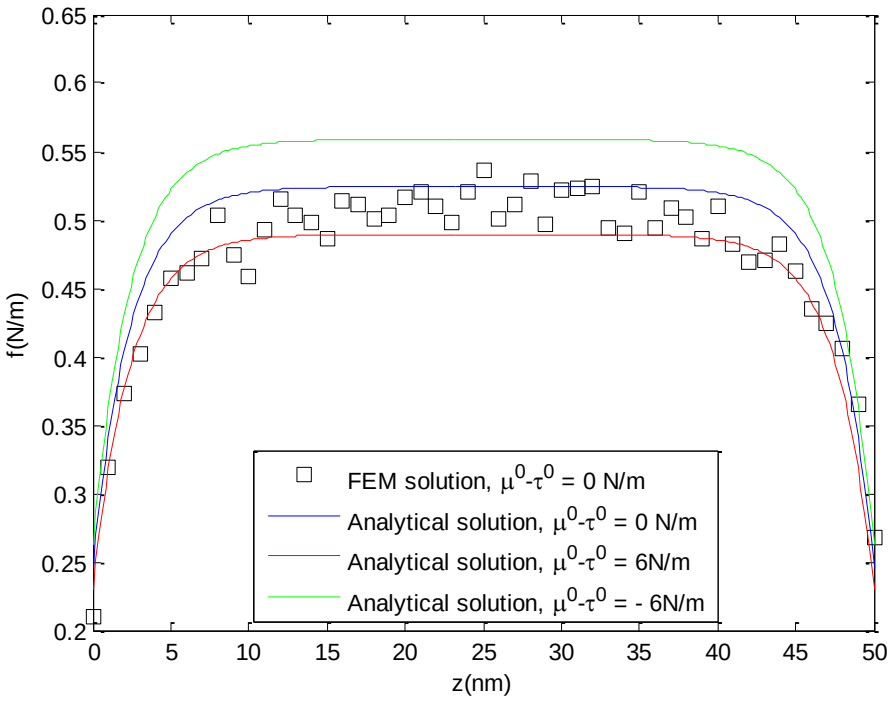
0.65
0.6
0.55
0.5
0.45
0.4
0.35
0.3
0.25
0.2
f(N/m)
0
5
10
15
20
25
30
35
40
45
50
z(nm)
FEM solution, μ0-τ0 = 0 N/m
Analytical solution, μ0-τ0 = 0 N/m
Analytical solution, μ0-τ0 = 6N/m
Analytical solution, μ0-τ0 = - 6N/m

(a)

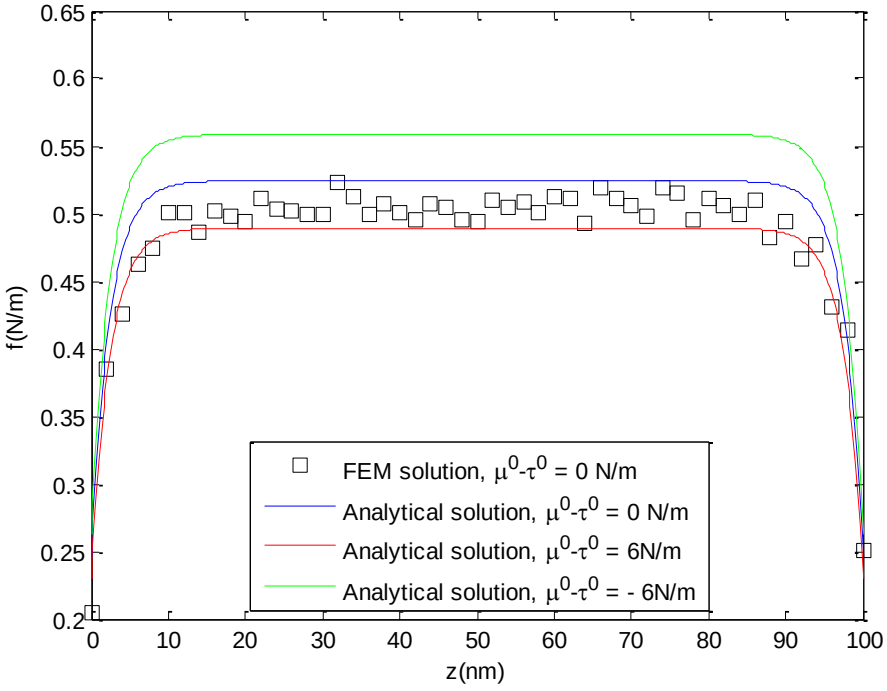
0.65
0.6
0.55
0.5
0.45
0.4
0.35
0.3
0.25
0.2
f(N/m)
0
10
20
30
40
50
60
70
80
90
100
z(nm)
FEM solution, μ0-τ0 = 0 N/m
Analytical solution, μ0-τ0 = 0 N/m
Analytical solution, μ0-τ0 = 6N/m
Analytical solution, μ0-τ0 = - 6N/m

(b)

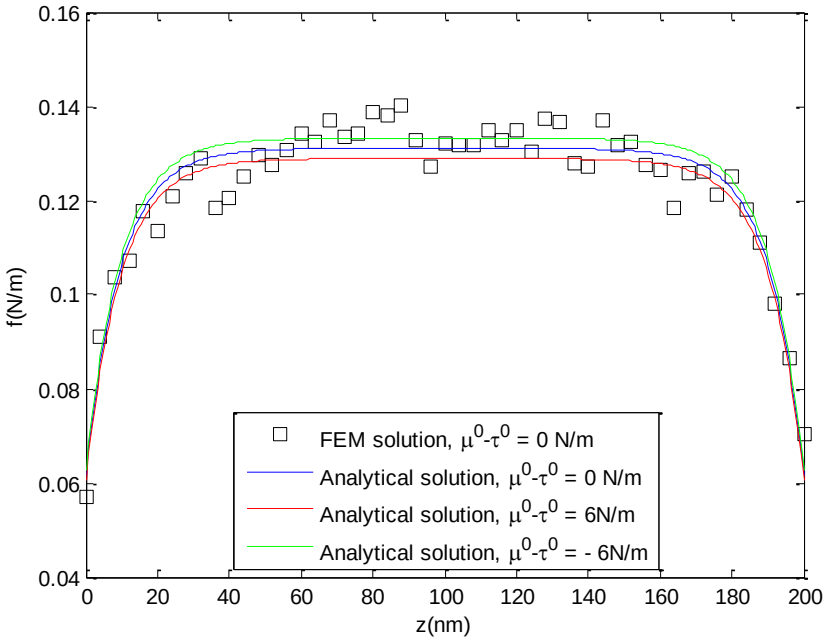

(c)

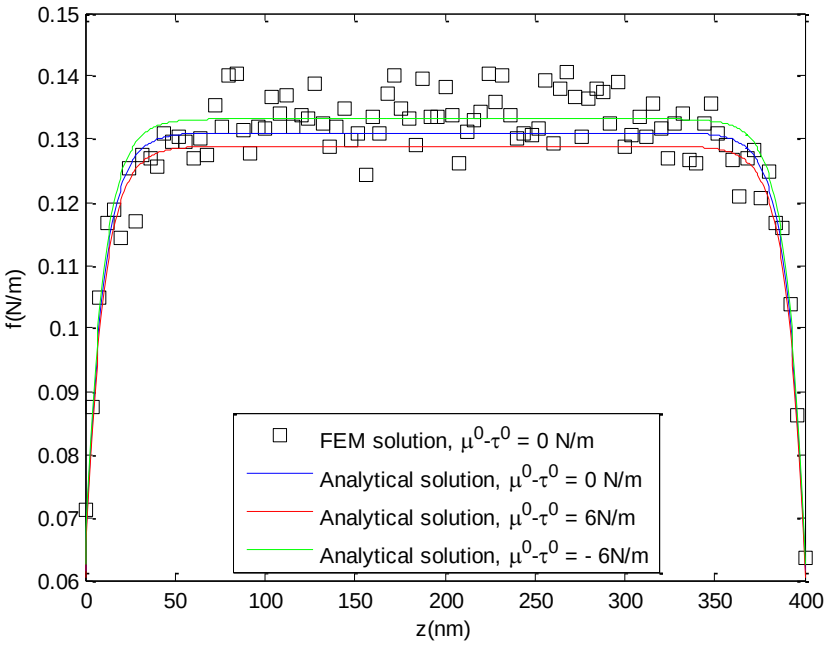

(d)

Figure 36. Comparison of image forces in isotropic nanorods (a. R = 10 nm, H = 50 nm; b.R = 10 nm, H = 100 nm; c. R = 40 nm, H = 200 nm; d. R = 40 nm, H = 400 nm)

Anisotropic Effect

To study the anisotropic effect, in the analytical framework, the anisotropy of materials is incorporated through Eq. (38) with the stiffness tensor and Eq. (41) with the Green's function. In the case of wurzite GaN with HCP lattice structure, it basically has 6 bulk elastic constants [28], or approximated as a transversely isotropic material with 5 bulk elastic constants[14, 15, 44, 82]. The nonzero independent components of its stiffness tensor in Eq. (25) are C_{11}, C_{12}, C_{13}, C_{33} and C_{44} with another nonzero dependent component $C_{66} = (C_{11} - C_{12})/2$. The expression of the Green's function for transversely isotropic materials is quite complex and it is provided by Pan and Chou[87]:

$$G_{11}(x) = \sum_{i=1}^{2} \{(A_i^{'} - B_i^{'})(\frac{\nu_i}{R_i} - \frac{\nu_i x_1^2}{R_i^3}) + 2\nu_i B_i^{'}(\frac{1}{R_i^*} - \frac{x_1^2}{R_i R_i^{*2}})\} + D(\frac{1}{R_3^*} - \frac{x_2^2}{R_3 R_3^{*2}}), \quad (102)$$

$$G_{12}(x) = G_{21}(x) = \sum_{i=1}^{2} \{-(A_i^{'} - B_i^{'}) \frac{\nu_i x_1 x_2}{R_i^3} - \frac{2\nu_i B_i^{'} x_1 x_2}{R_i R_i^{*2}}\} + D \frac{x_1 x_2}{R_3 R_3^{*2}}, \quad (103)$$

$$G_{3j}(x) = \sum_{i=1}^{2} \{-(A_i^{'} - B_i^{'}) \frac{\nu_i^2 k_i x_j z_i}{R_i^3} - \frac{2x_j (C_{11} A_i^{'} - C_{44} \nu_i^2 B_i^{'})}{R_i R_i^* (C_{13} + C_{44})}\}, (j = 1, 2) \quad (104)$$

$$G_{j3}(x) = \sum_{i=1}^{2} \{\frac{\nu_i A_i x_j}{R_i R_i^*} - \frac{(A_i + B_i)\nu_i z_i x_j}{R_i^3}\}, (j = 1, 2) \quad (105)$$

$$G_{33}(x) = \sum_{i=1}^{2} \{-\frac{C_{11} B_i + C_{44} \nu_i^2 A_i}{R_i (C_{13} + C_{44})} - \frac{(A_i + B_i)\nu_i^2 (C_{11} x_3^2 + C_{44} \rho^2)}{R_i^3 (C_{13} + C_{44})}\} \quad (106)$$

$$G_{22}(x) = \sum_{i=1}^{2} \{(A_i^{'} - B_i^{'})(\frac{\nu_i}{R_i} - \frac{\nu_i x_2^2}{R_i^3}) + 2\nu_i B_i^{'}(\frac{1}{R_i^*} - \frac{x_2^2}{R_i R_i^{*2}})\} + D(\frac{1}{R_3^*} - \frac{x_1^2}{R_3 R_3^{*2}}), \quad (107)$$

where

$$\nu_1 = \sqrt{\frac{(\widetilde{C}_{13} - C_{13})(\widetilde{C}_{13} + C_{13} + 2C_{44})}{4C_{33}C_{44}}} + \sqrt{\frac{(\widetilde{C}_{13} + C_{13})(\widetilde{C}_{13} - C_{13} - 2C_{44})}{4C_{33}C_{44}}}, \tag{108}$$

$$\nu_2 = \sqrt{\frac{(\widetilde{C}_{13} - C_{13})(\widetilde{C}_{13} + C_{13} + 2C_{44})}{4C_{33}C_{44}}} - \sqrt{\frac{(\widetilde{C}_{13} + C_{13})(\widetilde{C}_{13} - C_{13} - 2C_{44})}{4C_{33}C_{44}}}, \tag{109}$$

$$\widetilde{C}_{13} = \sqrt{C_{11}C_{33}}, \nu_3 = \sqrt{\frac{C_{66}}{C_{44}}}, D = \frac{1}{4}\pi C_{44}\nu_3, k_i = \frac{(\frac{C_{11}}{\nu_i^2} - C_{44})}{C_{13} + C_{44}}, \tag{110}$$

$$z_1 = \nu_1 x_3, z_2 = \nu_2 x_3, z_3 = \nu_3 x_3, R_i = \sqrt{x_1^2 + x_2^2 + z_i^2}, R_i^* = R_i + z_i. \tag{111}$$

For the case of $\widetilde{C}_{13} - C_{13} - 2C_{44} \neq 0$, the intermediate parameters are as follows:

$$\begin{aligned}
&A_1^{'} = B_1^{'} = -\frac{C_{44} - C_{33}\nu_1^2}{8\pi C_{33}C_{44}(\nu_1^2 - \nu_2^2)\nu_1^2}, \\
&A_2^{'} = B_2^{'} = \frac{C_{44} - C_{33}\nu_2^2}{8\pi C_{33}C_{44}(\nu_1^2 - \nu_2^2)\nu_2^2}, \\
&\nu_1 A_1 = -\nu_2 A_2 = \frac{C_{13} + C_{44}}{4\pi C_{33}C_{44}(\nu_2^2 - \nu_1^2)}, \\
&B_i = -A_i.
\end{aligned} \tag{112}$$

For the case of $\widetilde{C}_{13} - C_{13} - 2C_{44} = 0$, the intermediate parameters are as follows:

$$\begin{aligned}
&A_1^{'} = A_2^{'} = \frac{1}{16\pi C_{11}}, B_1^{'} = B_2^{'} = \frac{1}{16\pi C_{44}\nu_1^2}, \\
&A_1 = A_2 = 0, B_1 = B_2 = -\frac{C_{13} + C_{44}}{16\pi C_{11}C_{44}}.
\end{aligned} \tag{113}$$

Although the Green's function for transversely isotropic materials above is given as the simple case of infinite media, it is still difficult to plug into our framework in Eq. (41). As a matter of fact, in nano-epitaxy, it has always been a challenging task to investigate the anisotropy effect analytically, and thus the anisotropic semiconductors are often approximated as isotropic materials. Kern and Müller[38] analyzed the elastic relaxation of coherent epitaxial deposits and treated the nanoisland as a simple isotropic cube with applications to $In_{0.5}Ga_{0.5}As/GaAs$ epitaxy. Luryi and Suhir[6] studied the critical deposition height for Ge_xSi_{1-x}/Si systems by taking the Ge_xSi_{1-x} epilayer as an isotropic film. Zubia and Hersee[12] extended the work of Luryi and Suhir to incorporate the compliance of the substrate, and the example of depositing $Ga_{0.51}In_{0.49}P/GaAs$ was used as an isotropic case study. Sharma and Ganti[88] obtained the size-dependent strain state of embedded quantum dots for InAs/GaAs systems and both InAs and GaAs are set to isotropic materials. Recently, Ahmadzadeh-Bakhshayesh et al. [24] studied surface/interface effects on elastic behavior of a screw dislocation in an eccentric core-shell nanowire which takes InAs as an isotropic core and InP as an isotropic shell.

However, in practical situations, such anisotropic effect should not be neglected. For instance, there have been massive studies on semiconductors (GaN, GaAs, InGaN, etc.) prepared through Metal-Organic Vapor Phase Epitaxy (MOVPE), which requires more precise anisotropic calculations instead of the traditional idealization as isotropic materials. Compared with the isotropic case, the determination of the elastic field and image force of dislocation in anisotropic media is much more complex and difficult. Early in the 1950's, Eshelby et al. [89] proposed a sextic anisotropic elasticity theory of straight dislocations for two-dimensional (2D) problems. This theory was later elaborated by Stroh as the well-known Stroh's formalism [90]. A few researches have been devoted in the investigation of the interaction between the dislocation and inclusion or point force in anisotropic cases [91-94], but the analysis involves lengthy derivations and the results are not provided in explicit form even for 2D problems.

This work revisits Eshelby's sextic anisotropic elasticity theory to obtain the elastic field of a screw dislocation in infinite anisotropic solid (cubic and hexagonal crystal). The image force of the dislocation in anisotropic nanowire is derived based on such elastic field by using the concept of "image dislocation". More importantly, this work proposes to study the image force of nanorod by approximating the three-dimensional (3D) shape effect as a height-dependent shape function, which could be obtained through curve fitting of the finite element data. Finally this work provides a concise analytical solution to the image force of dislocation in a general anisotropic nanorod, which is applied to the case of GaN nanostructures. Based on such results, the analytical approach in this work could provide insights for the nanostructure design and fabrication widely.

Elastic field of dislocations in infinite anisotropic crystals

Let us reconsider the problem of the elastic displacement about a straight dislocation in an infinite anisotropic media. The constitutive relationship of the stress and the strain is:

$$\sigma_{ij} = C_{ijkl}\varepsilon_{kl} \tag{114}$$

where C_{ijkl} is the stiffness tensor of the material.

The strain is related to the displacement through compatibility condition:

$$\varepsilon_{ij} = \frac{1}{2}(u_{i,j} + u_{j,i}) \tag{115}$$

The stress equilibrium condition reads:

$$\sigma_{ij,j} = 0. \tag{116}$$

For convenience, the coordinate axes are oriented with the x_3 (or z) axis parallel to the dislocation line. The stiffness tensor, C_{ijkl} is referred to this basic system. As in the work of Eshelby et al.[89], it indicates that the general solutions of the elastic equations (displacement, strain and stress) for an arbitrary homogeneous anisotropic solid are independent of x_3. In this case, Eq. (116) can be rewritten as:

$$\sigma_{i\alpha,\alpha} = 0, \tag{117}$$

where the Latin index takes from 1 to 3 and the Greek index takes from 1 to 2 only.

From Eqs. (38), (39) and (117), the displacement is given in the following:

$$C_{i\alpha k\beta} \frac{\partial^2 u_k}{\partial x_\alpha \partial x_\beta} = 0. \tag{118}$$

Eq. (118) represents three simultaneous equations for the three components of the displacement, which have the standard-form solutions of the following type:

$$u_k = A_k f(\eta), \tag{119}$$

where $\eta = x_1 + px_2$ while A_k and p are constants to be determined.

Put Eq. (119) back into (118), it yields:

$$[C_{i1k1} + (C_{i1k2} + C_{i2k1})\, p + C_{i2k2} p^2] A_k \frac{\partial^2 f}{\partial \eta^2} = 0. \tag{120}$$

After cancellation of the common factor $\partial^2 f / \partial \eta^2$, and denote by $a_{ik} = C_{i1k1} + (C_{i1k2} + C_{i2k1})\, p + C_{i2k2} p^2$, Eq. (120) becomes a linear equation of A_k:

$$a_{ik} A_k = 0. \tag{121}$$

To ensure the final nonzero displacement, this linear equation should have nonzero solutions to A_k only when the determinant of the matrix $[a_{ik}]$ is zero:

$$|[a_{ik}]| = 0. \tag{122}$$

Eq. (122) is a sixth-order equation of p with roots p_n (n = 1, 2, 3, 4, 5, 6). For each root, there is a set of $A_k(n)$ that satisfies Eq. (121). Eshelby et al.[89] have shown that p_n and $A_k(n)$ must occur in pairs of complex conjugates ($p_i = p_{i+3}^*, A_k(i) = A_k^*(i+3), i = 1, 2, 3$), thus one can only consider the three roots (p_1, p_2, p_3) and the corresponding sets ($A_k(1)$, $A_k(2)$, $A_k(3)$), and the displacement is solved as:

$$u_k = \mathrm{Re}[\sum_{n=1}^{3} A_k(n)\, f_n(\eta_n)], \tag{123}$$

where Re[…] means “the real part of …” and $\eta_n = x_1 + p_n x_2$.

The three analytical functions, f_n are taken in the following form:

$$f_n(\eta_n) = \frac{D(n)}{2\pi i}\ln(\eta_n), \tag{124}$$

where *D(n)* are three complex variables to be solved.

The displacement of dislocations is satisfied from Eq. (123) and (124):

$$\mathrm{Re}[\sum_{n=1}^{3} \pm A_k(n) D(n)] = b_k, \tag{125}$$

where b_k is the k-th component of the Burgers vector of dislocations.

Since the dislocation is embedded in an infinite media, there should be no net force on the dislocation line, which is guaranteed by[25]:

$$\mathrm{Re}[\sum_{n=1}^{3} \pm B_{i2k}(n) A_k(n) D(n)] = 0, \tag{126}$$

where $B_{ijk}(n) = C_{ijk1} + C_{ijk2} p_n$.

In Eqs. (125) and (126), the plus sign is used when the imaginary part of p_n is positive and the minus sign is used when it is negative. Eqs. (125) and (126) are sufficient to solve *D(n)* and the displacement and stress field can be obtained from Eqs. (123) and (38) afterwards.

The anisotropic effect in cubic and hexagonal close-packed (HCP) crystals is depicted by the anisotropic ratio, $\beta = \sqrt{2C_{44}/(C_{11}-C_{12})}$. Table 8 shows the solutions to elastic fields of a screw dislocation embedded in cubic and hexagonal crystals along different directions. The result of Cubic <001>-oriented dislocation is identical to the textbooks [25, 31] by using eigenstrain method, and the result of Cubic <110>-oriented dislocation is also in accordance with Eshelby et al. [89] which has been given in cylindrical coordinate systems.

This work also provides the results for three basic axes oriented dislocations in hexagonal crystals in Table 8. It is interesting to find out that HCP <0001>-oriented dislocations generates the same elastic fields with Cubic <001>-oriented dislocations, and HCP <11-20> vs. Cubic <110> case. The result of HCP <1-100>-oriented dislocations is analog to HCP <11-20> by changing the anisotropic ratio from β to $1/\beta$. On the other hand, although hexagonal crystals have two more independent elastic constants (C_{13}, C_{33}) than cubic crystals, the two constants don't appear in the results for the three basic axes oriented dislocations in hexagonal crystals here. However, if we consider a dislocation oriented in other directions of cubic or hexagonal crystals, those two constants may appear in the final result[95].

Table 8. Elastic field of a screw dislocation embedded in infinite anisotropic media

	u_i	σ_{ij}
Cubic <001>	$u_3 = \frac{b}{2\pi}\arctan(\frac{x_2}{x_1})$	$\sigma_{13} = -\frac{C_{44}b}{2\pi}\frac{x_2}{x_1^2+x_2^2}$ $\sigma_{23} = \frac{C_{44}b}{2\pi}\frac{x_1}{x_1^2+x_2^2}$
Cubic <110>	$u_3 = \frac{b}{2\pi}\arctan(\frac{\beta x_2}{x_1})$	$\sigma_{13} = -\frac{C_{44}b}{2\pi}\frac{\beta x_2}{x_1^2+\beta^2 x_2^2}$ $\sigma_{23} = \frac{C_{44}b}{2\pi\beta}\frac{x_1}{x_1^2+\beta^2 x_2^2}$
HCP <0001>	$u_3 = \frac{b}{2\pi}\arctan(\frac{x_2}{x_1})$	$\sigma_{13} = -\frac{C_{44}b}{2\pi}\frac{x_2}{x_1^2+x_2^2}$ $\sigma_{23} = \frac{C_{44}b}{2\pi}\frac{x_1}{x_1^2+x_2^2}$
HCP <11-20>	$u_3 = \frac{b}{2\pi}\arctan(\frac{\beta x_2}{x_1})$	$\sigma_{13} = -\frac{C_{44}b}{2\pi}\frac{\beta x_2}{x_1^2+\beta^2 x_2^2}$ $\sigma_{23} = \frac{C_{44}b}{2\pi\beta}\frac{x_1}{x_1^2+\beta^2 x_2^2}$
HCP <1-100>	$u_3 = \frac{b}{2\pi}\arctan(\frac{x_2}{\beta x_1})$	$\sigma_{13} = -\frac{C_{44}b}{2\pi}\frac{\beta x_2}{\beta^2 x_1^2+x_2^2}$ $\sigma_{23} = \frac{C_{44}b}{2\pi}\frac{\beta^3 x_1}{\beta^2 x_1^2+x_2^2}$

Image force of dislocations in anisotropic cylindrical solids

As state in Chapter 2, when dislocations are embedded in an infinite media, there is no net force acted on dislocations. However, if the domain is finite, dislocations will be subjected to the so-called "image forces" due to the interaction between dislocations and crystal surfaces. The study of image forces is useful to investigate the stability and dynamic behavior of dislocations and further determine the properties of materials. One typical example is the study of dislocation dissipation in nanowires prepared by Nano-Epitaxy. The nanowire could be seen as an infinite anisotropic cylinder and the

dislocation could be attracted to the surrounding free surface by the image force when the nanowire meets certain geometrical requirements. This is very important for fabricating dislocation-free nanostructures and brings a promising approach for the design process.

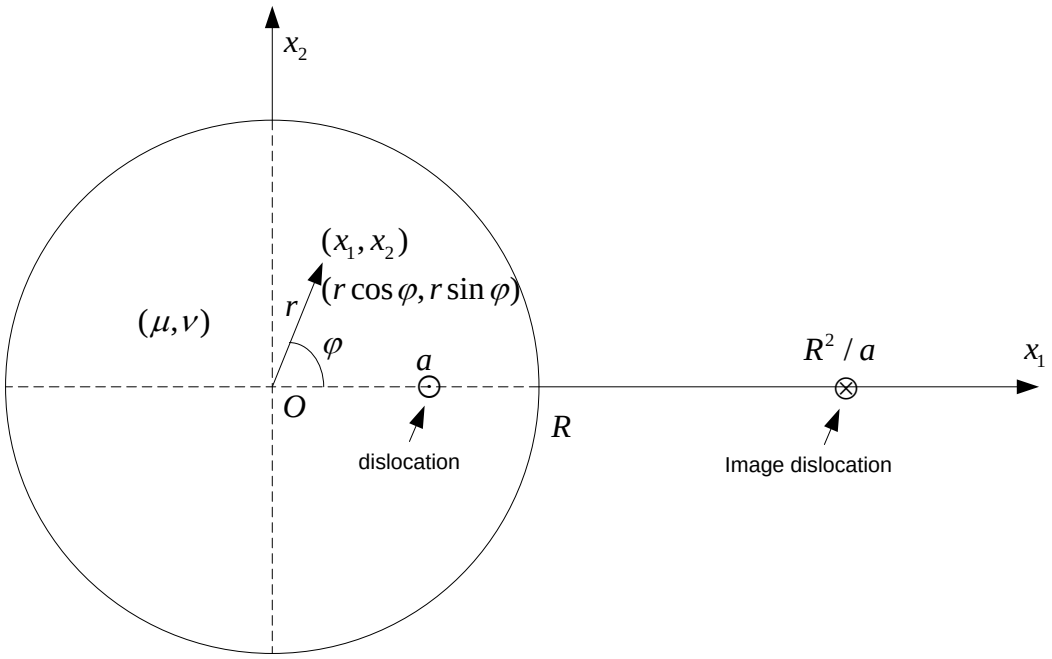

Figure 37. Cross-view of a screw dislocation in a nanowire with its "image dislocation"

For the present case, consider a straight screw dislocation with Burgers vector $\vec{b} = [0, 0, b]$ oriented in <001> direction in the nanowire (Figure 37). The radius of the nanowire is *R* and the dislocation is located on x_1-axis with an offset of *a* from the center. The bulk material elastic constants are denoted by μ as the shear modulus and υ as the Poisson's ratio. The free surface traction boundary condition is:

$$\sigma_{ij} n_j = 0, \tag{127}$$

where n_j is the unit vector normal to the free surface.

A simple solution to the image force of a screw dislocation in an isotropic nanowire is given by Eshelby et al. [86] by introducing an "image dislocation" with an opposite Burgers vector located at R^2/a. The stress field is solved as:

$$\sigma_{13} = -\frac{\mu b}{2\pi}\left(\frac{x_2}{(x_1-a)^2+x_2^{\,2}} - \frac{x_2}{(x_1-\frac{R^2}{a})^2+x_2^{\,2}}\right), \tag{128}$$

$$\sigma_{23} = \frac{\mu b}{2\pi}\left(\frac{x_1-a}{(x_1-a)^2+x_2^{\,2}} - \frac{x_1-\frac{R^2}{a}}{(x_1-\frac{R^2}{a})^2+x_2^{\,2}}\right). \tag{129}$$

The image force is given as [25, 86]:

$$f = \frac{\mu b^2}{2\pi}\frac{a}{R^2-a^2} \tag{130}$$

When the solid is considered to be anisotropic, the same results are found in case of Cubic <001> or HCP <0001> -oriented dislocations according to the stress field in Table 8 compared with isotropic case. However, if we apply the same "image dislocation" method for dislocations oriented along other directions in Table 8, the image force in case of Cubic <110> or HCP <11-20> -oriented dislocations is:

$$f = \frac{C_{44}b^2}{2\pi\beta}\frac{a}{R^2-a^2} \tag{131}$$

Similarly, the image force in case of HCP <1-100> -oriented dislocations is:

$$f = \frac{C_{44} b^2 \beta}{2\pi} \frac{a}{R^2 - a^2} \tag{132}$$

However, it could be checked that the free surface traction boundary condition of Eq. (127) will not be satisfied perfectly in these two cases.

Take the case of Cubic <110> or HCP <11-20> -oriented dislocations as an example. In cylindrical coordinate system, Eq. (127) can be reduced to prove $\sigma_{ij} n_j = \sigma_{ir} n_r = \sigma_{ir} = 0, (i, j = r, \theta, z)$. Since $\sigma_{rr} = \sigma_{r\theta} = 0$ for screw dislocations, it only requires $\sigma_{zr} = 0$. From Eq. (38), this means:

$$\sigma_{zr} = C_{zrkl} u_{k,l} = C_{zrzl} u_{z,l} = C_{zrzr} u_{z,r} + C_{zrz\theta} u_{z,\theta} \tag{133}$$

where $k = z$ and $l = r, \theta$ because only $u_z \neq 0$ and it exclusively depends on r, θ.

In Eq. (133), the stiffness tensor is expressed in cylindrical coordinate system. It can be calculated from the basic stiffness tensor in Cartesian coordinate system in the following way:

$$C_{rstu} = a_{ri} a_{sj} a_{tk} a_{ul} C_{ijkl} \tag{134}$$

where C_{rstu} is the stiffness tensor in cylindrical coordinate system and C_{ijkl} is the stiffness tensor in Cartesian coordinate system; $\boldsymbol{a}$ is the transformation matrix between the two coordinate systems which is given as:

$$\boldsymbol{a} = \begin{bmatrix} \cos\theta & \sin\theta & 0 \\ -\sin\theta & \cos\theta & 0 \\ 0 & 0 & 1 \end{bmatrix} \tag{135}$$

From Eqs. (134) and (135), one can easily get $C_{zrzr} = C_{1212} = C_{44}$ and $C_{zrz\theta} = 0$. Therefore Eq. (133) is reduced to prove:

$$u_{z,r} = 0 \tag{136}$$

If we apply the same "image dislocation" method to anisotropic case, and we assume the image dislocation is located at a general position λ instead of R^2/a in isotropic case, the displacement field is given as:

$$u_z = \frac{b}{2\pi}(\arctan\frac{\beta x_2}{x_1 - a} - \arctan\frac{\beta x_2}{x_1 - \lambda}) \tag{137}$$

Note that

$$u_{z,r} = \frac{\partial u_z}{\partial x_1}\frac{\partial x_1}{\partial r} + \frac{\partial u_z}{\partial x_2}\frac{\partial x_2}{\partial r} = \frac{\partial u_z}{\partial x_1}\frac{x_1}{r} + \frac{\partial u_z}{\partial x_2}\frac{x_2}{r} \tag{138}$$

It can be calculated as:

$$u_{z,r} = \frac{b}{2\pi}[\frac{-x_2\beta a}{(x_1 - a)^2 + (\beta x_2)^2} + \frac{x_2\beta\lambda}{(x_1 - \lambda)^2 + (\beta x_2)^2}] \tag{139}$$

Combining Eqs. (136) and (139) with the substitutions of $x_1 = R\cos\theta, x_2 = R\sin\theta$, we get:

$$R^2(1-\beta^2)(\lambda-a)\cos^2\theta - a(\lambda^2+\beta^2R^2) + \lambda(a^2+\beta^2R^2) = 0 \tag{140}$$

The free surface traction boundary condition on the outer circle indicates Eq. (140) holds for any $\theta \in [0, 2\pi)$. Since the case of $\lambda = a$ is not concerned here, the only choice is:

$$\beta = 1, \lambda = \frac{R^2}{a} \tag{141}$$

which is the solution to the isotropic case.

From Eq. (140), we can see that the first term cannot be eliminated for any $\theta \in [0, 2\pi)$ in anisotropic case. This means the free surface traction boundary condition cannot be satisfied by using "image dislocation" method in anisotropic case.

This deviation comes from the anisotropic effect on dislocations oriented along lower symmetric directions, thus it could be very sensitive to the anisotropic ratio. Furthermore, this deviation can be directly predicted from Eq. (127), which indicates the stress component, σ_{rz} (in cylindrical coordinate system) will become nonzero for dislocations oriented along lower symmetric directions.

Figure 38 shows the stress deviation changes with different anisotropic ratios for Cubic <110> or HCP <11-20>-oriented dislocations (HCP <1-100> case is similar by changing β to 1/β). The stress component, σ_{rz} has been normalized after being divided by $\sigma_0 = C_{44}b/2\pi R$. Obviously the deviation decreases so the stresses and image forces converge to isotropic case when β→1, otherwise the differences become larger as β

deviates more from 1. The curves for $\beta < 1$ and $\beta > 1$ cases look like "reciprocal" of each other, which can be seen directly from the image force formulations given in Eqs. (131) and (132). Moreover, the stress deviation is most obviously seen in the region of $20^\circ \sim 50^\circ$ and the symmetric region of $310^\circ \sim 340^\circ$. In fact, the maximum stress deviation can be controlled to be less than 10% of σ_0 when $0.9 < \beta < 1.1$. Note that the stress deviation is measured with respect to σ_0, which is mostly larger than the actual stress on the outer circle as seen in Eqs. (59) and (60). In some cases, such stress deviation could be neglected and the simple image force formulations could be directly adopted for the analysis thereafter.

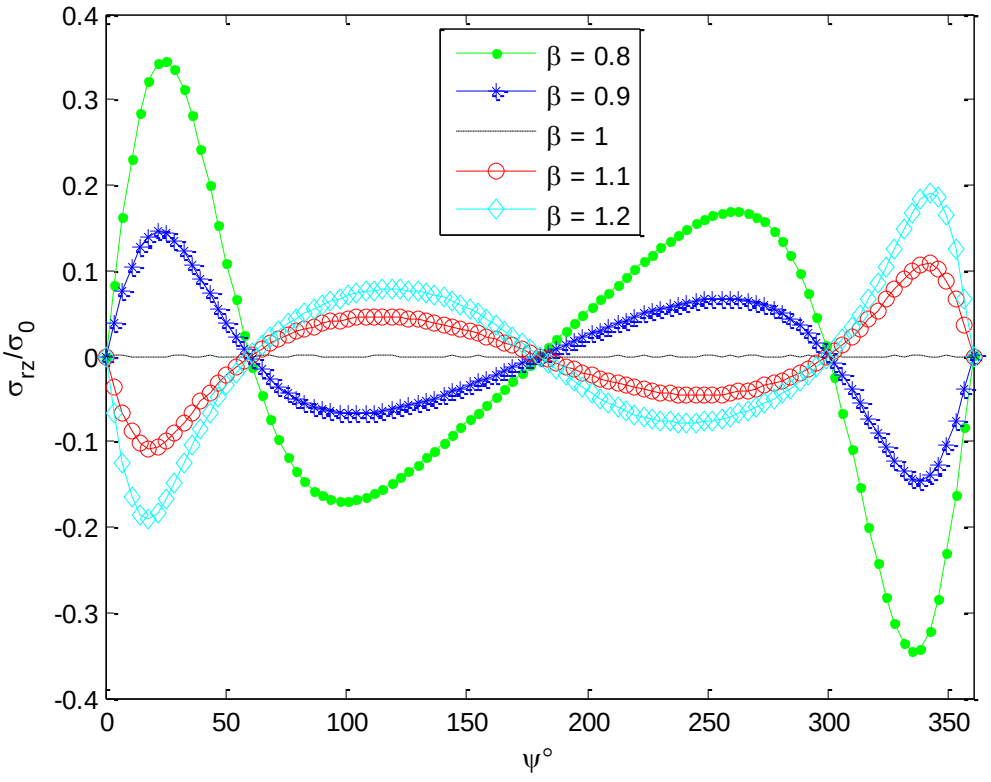

Figure 38. Anisotropic effect on the stress component, σ_{rz} along the outer circle for Cubic <110> or HCP <11-20>-oriented dislocations

Applications to GaN nanostructures

GaN nanowire is a typical semiconductor nanostructure which is widely prepared through Metal-Organic Vapor Phase Epitaxy (MOVPE). As a wurtzite lattice structure (an example of hexagonal crystal system), GaN is usually grown along <0001> (*c*-) polar axis, but nowadays it has been found out that epitaxial <11-20> (*a*-) and <1-100> (m-) non-polar GaN demonstrates better internal quantum efficiency by reducing spontaneous and piezoelectric polarizations [96-98]. Considering the crucial role that the dislocation plays in determining the properties of solids, it is important to investigate how dislocations behave in such anisotropic crystals, which is highly influenced by the image force acted on dislocations. Recently, there have been only some numerical studies by finite element method on the image force of dislocations in anisotropic GaN nanowires and nanorods [14, 15, 82], but analytical approaches will be more fundamental and they will provide better insights for the nanostructure design and fabrication.

The anisotropic ratio of GaN is calculated to be $\beta = \sqrt{2C_{44}/(C_{11}-C_{12})} = 0.9258$ [44], therefore the maximum stress deviation on the boundary of GaN nanowires will be less than 10% of σ_0 for this case as predicted in Figure 38. More specifically, the actual stress components of anisotropic GaN are plotted along with the isotropic case (Figure 39). As seen in Section 3, the stress deviation in Figure 38 is normalized by σ_0, which is much larger than the actual stress here, so the actual stress components of GaN are very close to the isotropic case. This means the "image dislocation" method could be directly applied to the analysis of image forces on GaN dislocations. The results for GaN dislocations along the three basic axes are provided in Eqs. (88) - (132).

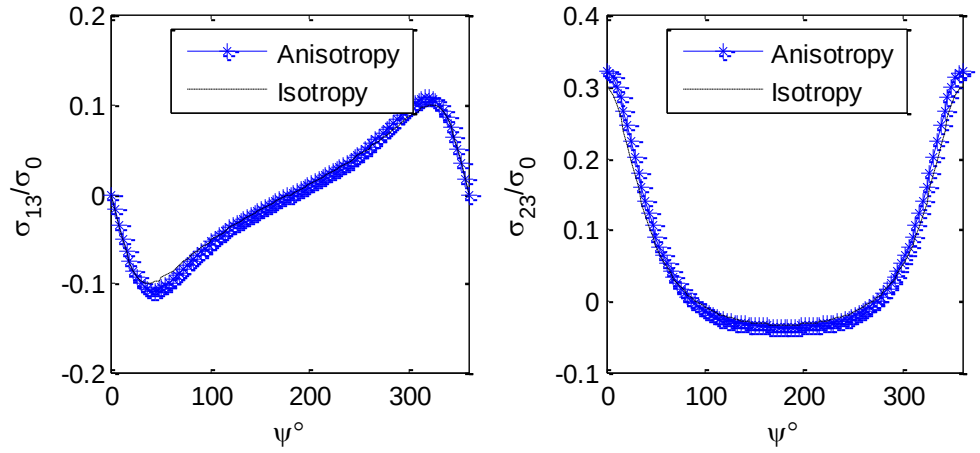

(a) (b)

Figure 39. Stress components of GaN nanowire on the outer circle and the comparison with isotropic case (a. σ_{13}; b. σ_{23})

The current analytical result is also compared with that from finite element analysis. Table 9 shows image forces of dislocations along <11-20> (*a*-) and <0001> (c-) axes of GaN nanowires with different sizes by finite element method[82]. For all nanowires, the result of f_c/f_a is close to GaN anisotropic ratio, which is consistent with the current solution predicted by Eqs. (88) and (131). The absolute magnitude of the image force in Table 9 is different from the current analytical result, but the magnitude ratios of the two results are consistent when the radius changes. This difference comes from the calculating approximation used in each approach as discussed in Ref. [99] and it suggests using a correction factor to link the analytical result to the finite element data. For the current case of GaN nanowires, the correction factor is set to $\gamma = 4.6803$.

Table 9. Image forces of GaN grown along <11-20> (*a*-) and <0001> (c-) axes

R (nm)	f_a (N/m)	f_c (N/m)	f_c/f_a
10	1.3630	1.3120	0.9626
20	0.7435	0.7072	0.9512
40	0.4209	0.3956	0.9399

With the obtained shape function, the final analytical solution to the image force for GaN nanorods is given as:

$$f = \gamma f_0 \times g(z), \tag{142}$$

where γ is the correction factor by calibrating with the finite element data; f_0 is the corresponding image force of the nanowire along different orientations provided by Eqs. (88) - (132); *g(z)* is the shape function consisting of only z coordinate and it is given in Eq. (100) by curve fitting of the finite element data.

The final result in Eq. (142) provides an analytical tool to calculate the image forces on dislocations in GaN nanorods. Compared with numerical results from finite element method, it is much easier and faster to obtain image forces for any GaN nanorod once the geometrical parameters are given, which brings much convenience to predict the behavior of dislocations in MOVPE process. Our solution is also extendable to comply with other types of crystals by replacing the original image force part (f_0) in Eqs. (88) - (132), which takes account for different elastic constants with different crystals. In addition to that, it is also possible to incorporate other influencing factors into the current analytical solution, e.g., surface stress of nanostructures that plays an important role when the critical dimension of nanostructures becomes less than 10 nm. This can be

implemented by refining the image force part (f_0) with the consideration of surface elasticity tensors [22, 23, 99-101].

In this work, image forces of dislocations along the three basic axes in GaN nanorods are calculated from the analytical solution in Eq. (142) and they are compared with finite element results. In Figure 40, image forces start from zero and increase along the height of nanorods, and then they stay as a plateau in the middle region until they approach the other end of nanorods. The two regions near each end of nanorods are symmetric with each other and we can see the surface effect from the two ends only penetrates to a certain depth into the nanorod. Although the finite element result has some fluctuations due to the precision of numerical calculations, it is clear that the curve trend agrees well with the corresponding analytical solution even when the radius of the nanorod changes. This is as expected since the shape function in the analytical solution of Eq. (142) is obtained by fitting to the finite element data.

As predicted by the analytical solution, the magnitudes of image forces on dislocations along different axes are ordered as: $f_a > f_c > f_m$. Since the image force could be viewed as the driving source in solids to dissipate dislocations towards surfaces, this is interesting to the process of MOVPE as it indicates GaN grown along one non-polar direction (a-axis) could have better mechanical properties than the standard growth method along the polar direction (c-axis), but the situation would be worse for GaN grown along the other non-polar direction (m-axis). Recently, experimental and theoretical studies on <0001>-oriented dislocation dissipation mechanism in anisotropic GaN nanowires and nanorods [14, 15, 82] have demonstrated: GaN nanorod grown along c-axis with a radius of 26 nm and a height of 65 nm provides the most efficient dislocation filtering with a probability of up to 95% as a result of image forces. Based on this result and the current work, one can expect GaN nanorods grown along a-axis with the same geometry aforementioned could have lower dislocation densities, or one can fabricate GaN nanorods of comparable qualities along a-axis with a larger range of radius choices and vice versa for GaN nanorods grown along m-axis. Unfortunately, there are only some provisional experimental observations on bulk GaN layers grown in non-polar

directions in literatures [96-98], but no effort has been devoted in growing GaN nanowires or nanorods in those directions so far.

The results of image forces are obtained specifically for GaN nanorods here, but the analytical approach developed in this work is applicable to other material systems, such as GaAs, InGaN etc. which also exhibit the anisotropic effect when their mechanical properties are considered. Therefore, this work could contribute to a wide range of nanostructure design and fabrication for dislocation-free devices.

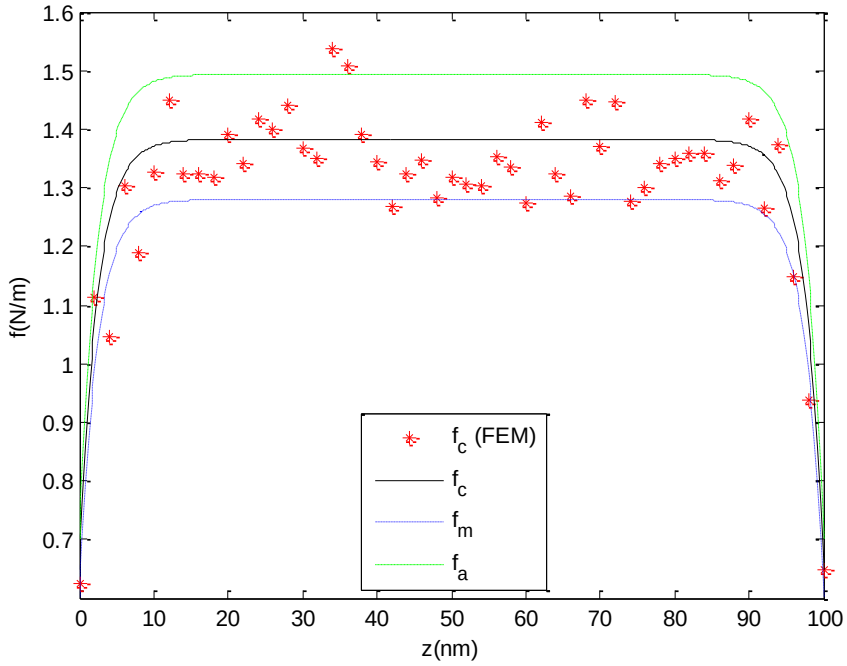

(a)

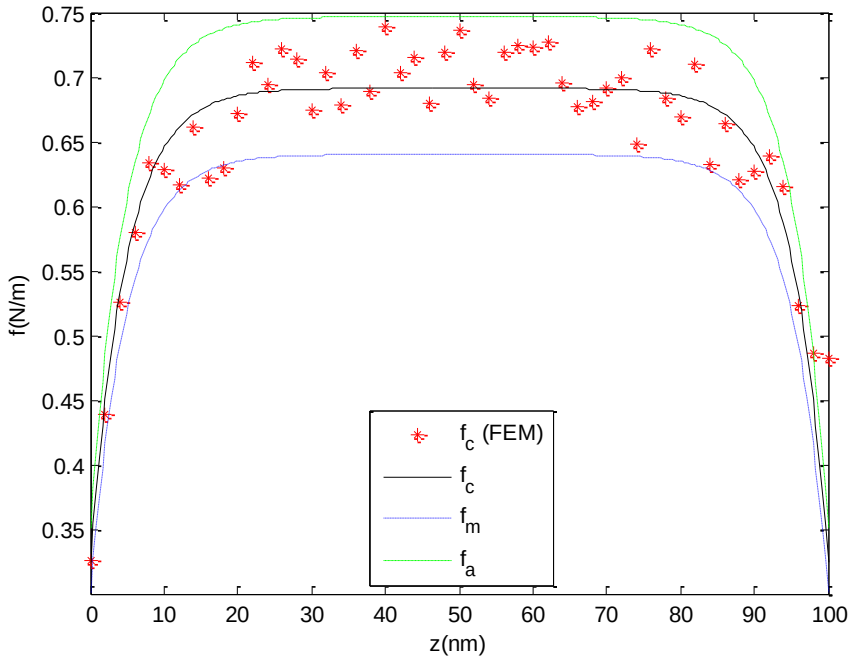

(b)

Figure 40. Image forces of dislocations in GaN nanorods (a. r = 10 nm; b. r = 20 nm)

This work solves the stress field of a screw dislocation in an infinite anisotropic solid. The image force of a dislocation in an anisotropic nanowire is then derived by using the concept of "image dislocation" and that is also obtained for nanorods by approximating the three-dimensional (3D) shape effect as a height-dependent shape function, which is fitted to the finite element data. The analytical solution is applied to analyze image forces on different dislocations in GaN nanorods oriented along polar (c-axis) and non-polar (a, m-axis) directions. The result shows the dislocation dissipation could be more effective in a-GaN but less in m-GaN by comparing with the standard growth of c-GaN. The approach developed in this work is applicable to other material systems, such as GaAs, InGaN etc. Therefore, it could contribute to a wide range of nanostructure design and fabrication for dislocation-free devices.

CHAPTER 7

CONCLUSIONS AND RECOMMENDATIONS

The work presented in this dissertation provides a thorough multi-scale modeling and design of nanostructures prepared through Metal-Organic Vapor Phase Epitaxy (MOVPE), along with its possible application to the practical fabrication of high-quality semiconductor devices. It aims at a systematic investigation about the dislocation dissipation mechanism in nanostructures by combining the surface effect at atomistic level and the mechanical model at macroscopic level. The target is to provide some feasible and reliable design tools or routines for growing high quality nanostructures (size, geometry, anisotropy, etc.). It will contribute to providing guidance for the fabrication of next-generation dislocation-free nano-devices.

Scientific Contributions

This work ranges from the development of fundamental mechanical formulations to the numerical application to practical nanostructure analysis. In terms of the former point, this work has the following significant contributions:

• It provides a clear understanding of dislocation dissipation mechanism by the image force due to surface effect. Two representative approaches, the nonlocal method and the energy method, are explained about their principles, calculating procedures, along with examples of their usage.

• It has developed a novel analytical framework to solve the elastic field of solids with dislocations and surface stress. The core idea of this framework is to combine the general eigenstrain problem solution from micromechanics and the surface elasticity model from atomistic studies. It could be applied to general anisotropic 3D materials which are unable to be handled by other literature works (mostly based on complex

variable method and its variants). More importantly, it allows for the exact analytical expression of the results instead of the power series solution in complex variable method. Such exact analytical expressions of the stress or strain field will be more flexible to manipulate in further applications, and the physical meanings of the surface property parameters are straightforward to interpret.

• It provides close-form stress solution to the case of isotropic circular nanowires (2D) based on the proposed analytical framework, and the analytical result of the image force has been derived afterwards. All the analytical results in this work are in explicit flexible forms compared to the complicate forms of infinite power series in complex variable method. The physical meaning of surface elasticity is clearly illustrated thanks to our result, which is hard to interpret from complex variable method. Concerning the result, σ_{13} components of our solution and complex variable method are close to each other and they both agree well with the classical result. σ_{23} components of our solution and complex variable method are different in magnitude, but they behave quite similarly in the changing trend. More favorably, our solution overlaps with the classical result for large nanowires but the solution of complex variable method deviates obviously from it.

On the other hand, in terms of applications, this work has the following contributions:

• It provides a finite element model of implementing a screw dislocation in solids with only free surfaces, which facilitate the specification of the surface boundary condition. The stress field obtained from finite element analysis is then used to calculate the image force of the dislocation. Through this numerical model, image forces of a screw dislocation embedded in various shaped GaN nanorods are calculated. By comparing with critical force to overcome the lattice resistance, this work demonstrate the mechanism of dislocation dissipation in GaN nanorods.

• It has obtained bulk and surface properties of crystals through Molecular Dynamic (MD) simulations. The concept of surface excess energy has also been illustrated, which brings about the definition of elastic surface property tensors. Finally, a complete dataset of GaN surface property tensors has been obtained and it could be used to study the surface effect of GaN nanostructures in the future.

• It revisits Eshelby's sextic anisotropic elasticity theory to obtain the elastic field of a screw dislocation in infinite anisotropic solid (cubic and hexagonal crystal). The image force of the dislocation in anisotropic nanowire is derived based on such elastic field by using the concept of "image dislocation". The result of HCP <1-100>-oriented dislocations is analog to HCP <11-20> by changing the anisotropic ratio from β to $1/\beta$. On the other hand, although hexagonal crystals have two more independent elastic constants (C_{13}, C_{33}) than cubic crystals, the two constants don't appear in the results for the three basic axes oriented dislocations in hexagonal crystals here.

• It proposes to extend the image force solution of nanowires (2D) to the case of nanorods (3D) by introducing a height-dependent shape function, which is obtained by curve fitting to the finite element data. The magnitude of the image force is adjusted with a correction factor. The comparison of image forces between the original finite element result without surface stress and the analytical results with and without surface stress shows that it agrees well with one another. This turns out to be as expected since the shape function is fitted to the original finite element data. In case that surface stress is considered, image forces generally increase for negative surface elasticity and decrease with positive surface elasticity. In this case, the surface with negative surface elasticity resembles a "soft" media compared to the bulk material and it becomes "rigid" with positive surface elasticity.

• It devotes to a specialized investigation on the case of anisotropic GaN nanostructures based on the aforementioned method. The analytical solution is applied to analyze image forces on different dislocations in GaN nanorods oriented along polar (c-

axis) anAlferov, 2001d non-polar (a, m-axis) directions. The result shows the dislocation dissipation could be more effective in a-GaN but less in m-GaN by comparing with the standard growth of c-GaN. The approach developed in this work is applicable to other material systems, such as GaAs, InGaN etc. Therefore, it could contribute to a wide range of nanostructure design and fabrication for dislocation-free devices.

Future Work Suggestions

The current work presented in this dissertation has provided a multi-scale nano-epitaxy modeling and design from atomistic simulations to continuum methods. It indeed has accomplished a thorough investigation of the elastic field and image force in solids with dislocations and surface stress, with some applications to the case of anisotropic GaN nanostructures. However, there are still some issues to be further improved, or some problems are not addressed within this work but might be related to this work. Here are some suggestions about such future work directions:

• The finite element model illustrated in Chapter 3 of this dissertation is only used for free surfaces. Such boundary condition is insufficient to describe the surface behavior for nanostructures as elaborated in this work. A possible improvement could be a refined specification of the surface boundary condition through the surface stress formulation in Eq. (18) or the surface excess energy model in Eq. (28). However, it requires additional work to make some codes of the user material properties. When the nano-scale surface effect is incorporated in a better way, the image force behavior should be expected to be distinct, and the dislocation dissipation could be investigated more accurately. Based on the methodology introduced in this work, it provides a feasible approach to incorporate the surface stress into the current dislocation model.

• Surface elasticity tensors are obtained in this work through MD simulations. Unfortunately, there are very few research reports about the surface property tensors for GaN in literatures. Here we only found the references on the constant surface excess energy values and they are obtained by first principle calculations[64, 65]. Although our

results agree well with those of the first principle calculations, but it is based on the simple curve fitting method which is mainly used for the pure crystal of single element at 0K temperature in principle. More theoretical work should be carried out on the validation of such calculations, or a better scheme of obtaining the surface elasticity tensors could be seek out.

• This work has developed a novel analytical framework to solve the elastic field of solids with dislocations and surface stress. It could be applied to general anisotropic 3D materials, which is only used for the calculation of the image force afterwards in this work. In fact, the solution to the stress and strain field could be used for many other scenarios but not limited to the case of image force. Since it allows for the exact analytical expression of the results instead of the power series solution in complex variable method, such exact analytical expressions of the stress or strain field will be more flexible to manipulate in further applications, especially some interdisciplinary situations such as mechanical-electrical, mechanical-optical or mechanical-magnetical devices.

• In Chapter 6, this work has obtained the image force of dislocations in anisotropic nanowires with the concept of "image dislocation". This is an approximated solution because it doesn't satisfy the boundary condition perfectly, so it should be improved by finding out the exact solution to this problem. In literatures, there have been some works devoted into such solutions to dislocations in anisotropic media with free surfaces[91, 93, 94]. The approach is based on the Stroh's formulism of complex analysis but it takes account for the free surface as a disturbance to the original stress field. It could provide an exact solution to the current problem but an explicit close-form solution seems to be impossible. However, when an exact solution is obtained, it should be helpful for a refined calculation in this work.

• An important factor of nano-epitaxy that is not addressed in this work is the lattice mismatch between the substrate and the epilayer, which is crucial in practical

fabrications of nanostructures. It could be seen as the main source of dislocation generation. In experiment, different substrates are carefully chosen to minimizing the lattice mismatch under the consideration of costs or other issues. Within the scope of this work, the lattice mismatch could be considered as an additional eigenstrain compared with the dislocation eigenstrain. The lattice mismatch is usually used to calculate the strain energy (without dislocation inside the material at this stage) and then it is compared to the critical energy of a single dislocation (without lattice mismatch inside the material then). However, it might be a challenging task to deal with the lattice mismatch and dislocation all together, which is rarely investigated in literatures neither. So far, the study on the interaction between lattice mismatch and dislocation is still an open question, even when no surface effect is considered.

• The work is to contribute to providing guidance for the fabrication of next-generation dislocation-free nano-devices. Therefore abundant experimental results will be a great collaboration with this work in terms of validation and inspiration. The aforementioned theoretical work has been supported from the experiment lab led by Dr. Abdallah Ougazzaden at Georgia-Tech, Lorraine, but the collaboration between my research and the experiment work needs to be intensified. Nowadays it is possible to analyze the stress or strain state in crystals through experimental measurements. This could be a great help to consolidate my work and make good correspondences with each other. It will be quite promising to provide feasible and reliable design tools or routines for growing high quality nanostructures in practical applications.

REFERENCES

[1] Z. I. Alferov, "Nobel Lecture: The double heterostructure concept and its applications in physics, electronics, and technology," *Reviews of modern physics,* vol. 73, pp. 767-782, 2001.

[2] C. Lin, *et al.*, "Improved GaN film overgrown with a molybdenum nanoisland mask," *Applied Physics Letters,* vol. 93, p. 031906, 2008.

[3] M. H. Lo, *et al.*, "Defect selective passivation in GaN epitaxial growth and its application to light emitting diodes," *Applied Physics Letters,* vol. 95, p. 211103, 2009.

[4] H. Y. Ryu, *et al.*, "Measurement of junction temperature in GaN-based laser diodes using voltage-temperature characteristics," *Applied Physics Letters,* vol. 87, p. 093506, 2005.

[5] K. Schwarz, "Simulation of dislocations on the mesoscopic scale. I. Methods and examples," *Journal of Applied Physics,* vol. 85, p. 108, 1999.

[6] S. Luryi and E. Suhir, "New approach to the high quality epitaxial growth of lattice-mismatched materials," *Appl. Phys. Lett.,* vol. 49, p. 140, 1986.

[7] R. People and J. Bean, "Calculation of critical layer thickness versus lattice mismatch for Ge_xSi_{1-x}/Si strained-layer heterostructures," *Applied Physics Letters,* vol. 47, p. 322, 1985.

[8] S. Srinivasan, *et al.*, "Slip systems and misfit dislocations in InGaN epilayers," *Applied Physics Letters,* vol. 83, p. 5187, 2003.

[9] Y. Zhong and T. Zhu, "Simulating nanoindentation and predicting dislocation nucleation using interatomic potential finite element method," *Computer Methods in Applied Mechanics and Engineering,* vol. 197, pp. 3174-3181, 2008.

[10] D. Du and D. J. Srolovitz, "Faceted dislocation surface pits," *Acta Materialia,* vol. 52, pp. 3365-3374, 2004.

[11] X. Liu, *et al.*, "Glide of edge dislocations in tungsten and molybdenum," *Materials Science and Engineering A,* vol. 365, pp. 96-100, 2004.

[12] D. Zubia and S. Hersee, "Nanoheteroepitaxy: The Application of nanostructuring and substrate compliance to the heteroepitaxy of mismatched semiconductor materials," *Journal of Applied Physics,* vol. 85, p. 6492, 1999.

[13] E. Kröner, "Continuum theory of defects," *Physics of defects,* vol. 35, pp. 217-315, 1981.

[14] Z. Liang, *et al.*, "GaN nanostructure design for optimal dislocation filtering," *Journal of Applied Physics,* vol. 108, p. 074313, 2010.

[15] R. Colby, *et al.*, "Dislocation Filtering in GaN Nanostructures," *Nano Letters,* vol. 10, pp. 1568-1573, 2010.

[16] R. Shuttleworth, "The surface tension of solids," *Proceedings of the Physical Society. Section A,* vol. 63, p. 444, 1950.

[17] M. E. Gurtin, *et al.*, "A general theory of curved deformable interfaces in solids at equilibrium," *Philosophical Magazine A,* vol. 78, pp. 1093-1109, 1998.

[18] M. E. Gurtin and A. Ian Murdoch, "A continuum theory of elastic material surfaces," *Archive for Rational Mechanics and Analysis,* vol. 57, pp. 291-323, 1975.

[19] Q. H. Fang and Y. W. Liu, "Size-dependent interaction between an edge dislocation and a nanoscale inhomogeneity with interface effects," *Acta Materialia,* vol. 54, pp. 4213-4220, 2006.

[20] Q. H. Fang, *et al.*, "Effect of interface stresses on the image force and stability of an edge dislocation inside a nanoscale cylindrical inclusion," *International Journal of Solids and Structures,* vol. 46, pp. 1413-1422, 2009.

[21] Q. H. Fang and Y. W. Liu, "Size-dependent elastic interaction of a screw dislocation with a circular nano-inhomogeneity incorporating interface stress," *Scripta Materialia,* vol. 55, pp. 99-102, 2006.

[22] Y. W. Liu and Q. H. Fang, "Analysis of a screw dislocation inside an inhomogeneity with interface stress," *Materials Science and Engineering: A*, vol. 464, pp. 117-123, 2007.

[23] J. Luo and Z. Xiao, "Analysis of a screw dislocation interacting with an elliptical nano inhomogeneity," *International Journal of Engineering Science*, vol. 47, pp. 883-893, 2009.

[24] H. Ahmadzadeh-Bakhshayesh, *et al.*, "Surface/interface effects on elastic behavior of a screw dislocation in an eccentric core-shell nanowire," *International Journal of Solids and Structures*, vol. 49, pp. 1665-1675, 2012.

[25] J. P. Hirth and J. Lothe, "Theory of dislocations," *John Wiley and Sons, Inc.*, 1982.

[26] D. Hull and D. J. Bacon, *Introduction to Dislocations*: Elsevier Science, 2011.

[27] E. Kröner, "Elasticity theory of materials with long range cohesive forces," *International Journal of Solids and Structures*, vol. 3, pp. 731-742, 1967.

[28] J. Nord, *et al.*, "Modelling of compound semiconductors: analytical bond-order potential for gallium, nitrogen and gallium nitride," *Journal of Physics: Condensed Matter*, vol. 15, p. 5649, 2003.

[29] R. DeWit, "Theory of disclinations IV," *J. Res. Natl Bur. Stand.(US). 77A*, pp. 607–658, 1973.

[30] T. Mura, *Micromechanics of defects in solids*: M. Nijhoff, 1987.

[31] J. Qu and M. Cherkaoui, *Fundamentals of micromechanics of solids*. Hoboken, N.J.: Wiley, 2006.

[32] R. C. Cammarata, "Surface and interface stress effects in thin films," *Progress in surface science*, vol. 46, pp. 1-38, 1994.

[33] P. Sharma, *et al.*, "Effect of surfaces on the size-dependent elastic state of nano-inhomogeneities," *Applied Physics Letters*, vol. 82, pp. 535-537, 2003.

[34] L. Tian and R. Rajapakse, "Finite element modelling of nanoscale inhomogeneities in an elastic matrix," *Computational Materials Science,* vol. 41, pp. 44-53, 2007.

[35] L. Tian and R. Rajapakse, "Elastic field of an isotropic matrix with a nanoscale elliptical inhomogeneity," *International Journal of Solids and Structures,* vol. 44, pp. 7988-8005, 2007.

[36] L. Tian and R. Rajapakse, "Analytical solution for size-dependent elastic field of a nanoscale circular inhomogeneity," *Journal of applied mechanics,* vol. 74, p. 568, 2007.

[37] G. Wang and T. Wang, "Deformation around a nanosized elliptical hole with surface effect," *Applied Physics Letters,* vol. 89, p. 161901, 2006.

[38] R. Kern and P. Müller, "Elastic relaxation of coherent epitaxial deposits," *Surface Science,* vol. 392, pp. 103-133, 1997.

[39] Y. Honda, *et al.*, "Selective area growth of GaN microstructures on patterned (111) and (001) Si substrates," *Journal of Crystal Growth,* vol. 230, pp. 346-350, 2001.

[40] Y. S. Chen, *et al.*, "Threading dislocation evolution in patterned GaN nanocolumn growth and coalescence overgrowth," *Journal of Applied Physics,* vol. 106, pp. 023521-023526, 2009.

[41] A. Murai, *et al.*, "Hexagonal pyramid shaped light-emitting diodes based on ZnO and GaN direct wafer bonding," *Applied Physics Letters,* vol. 89, p. 171116, 2006.

[42] B. Beaumont, *et al.*, "Magnesium induced changes in the selective growth of GaN by metalorganic vapor phase epitaxy," *Applied Physics Letters,* vol. 72, pp. 921-923, 1998.

[43] J. Farrer and C. Carter, "Defect structure in GaN pyramids," *Journal of materials science,* vol. 41, pp. 779-792, 2006.

[44] I. Vurgaftman and J. R. Meyer, "Band parameters for nitrogen-containing semiconductors," *Journal of Applied Physics,* vol. 94, p. 3675, 2003.

[45] G. Wei, *et al.*, "Finite element characterization of the size-dependent mechanical behaviour in nanosystems," *Nanotechnology,* vol. 17, p. 1118, 2006.

[46] A. Dollet, "Multiscale modeling of CVD film growth—a review of recent works," *Surface and Coatings Technology,* vol. 177-178, pp. 245-251, 2004.

[47] K. Ohno, *et al.*, *Computational Materials Science: From Ab Initio to Monte Carlo Methods* vol. 129: Springer, 2000.

[48] D. Raabe, *et al.*, *Continuum Scale Simulation of Engineering Materials: Fundamentals-Microstructures-Process Applications*: Wiley-VCH, 2006.

[49] S. Plimpton, "Fast parallel algorithms for short-range molecular dynamics," *Journal of Computational Physics,* vol. 117, pp. 1-19, 1995.

[50] M. S. Daw and M. I. Baskes, "Semiempirical, Quantum Mechanical Calculation of Hydrogen Embrittlement in Metals," *Physical Review Letters,* vol. 50, pp. 1285-1288, 1983.

[51] J. W. Martin, "Many-body forces in metals and the Brugger elastic constants," *Journal of Physics C: Solid State Physics,* vol. 8, p. 2837, 1975.

[52] S. M. Foiles, *et al.*, "Embedded-atom-method functions for the fcc metals Cu, Ag, Au, Ni, Pd, Pt, and their alloys," *Physical Review B,* vol. 33, pp. 7983-7991, 1986.

[53] W. Ye, "Nano-heteroepitaxy stress and strain analysis: from molecular dynamic simulations to continuum methods," Master Master Thesis, 2010.

[54] R. Dingreville, "Modeling and characterization of the elastic behavior of interfaces in nanostructured materials: From an atomistic description to a continuum approach," PhD, Mechanical engineering, Georgia Institute of Technology, 2007.

[55] Y. Hiki and A. Granato, "Anharmonicity in noble metals; higher order elastic constants," *Physical Review,* vol. 144, p. 411, 1966.

[56] J. Gibbs, "The collected works of J. Willard Gibbs. 1928," ed: New York: Longmans.

[57] C. Herring, "Diffusional viscosity of a polycrystalline solid," *Journal of Applied Physics,* vol. 21, pp. 437-445, 1950.

[58] W. W. Mullins, "Flattening of a nearly plane solid surface due to capillarity," *Journal of Applied Physics,* vol. 30, pp. 77-83, 1959.

[59] P. Sharma and S. Ganti, "On the grain-size-dependent elastic modulus of nanocrystalline materials with and without grain-boundary sliding," *Journal of materials research,* vol. 18, pp. 1823-1826, 2003.

[60] A. Andreev and Y. A. Kosevich, "Capillary phenomena in the theory of elasticity," *Zhurnal Eksperimentalnoi Teor. Fiz,* vol. 81, pp. 1435-1443, 1981.

[61] R. Dingreville and J. Qu, "A semi-analytical method to estimate interface elastic properties," *Computational Materials Science,* vol. 46, pp. 83-91, 2009.

[62] P. Gumbsch and M. S. Daw, "Interface stresses and their effects on the elastic moduli of metallic multilayers," *Physical Review B,* vol. 44, pp. 3934-3938, 1991.

[63] G. J. Ackland, *et al.*, "Simple N-body potentials for the noble metals and nickel," *Philosophical Magazine A,* vol. 56, pp. 735-756, 1987/12/01 1987.

[64] J. E. Northrup and J. Neugebauer, "Theory of GaN ($10\bar{1}0$) and ($11\bar{2}0$) surfaces," *Physical Review B,* vol. 53, p. 66679, 1996.

[65] J. E. Northrup and J. Neugebauer, "Indium-induced changes in GaN (0001) surface morphology," *Physical Review B,* vol. 60, pp. 8473-8476, 1999.

[66] J. D. Eshelby, "Elastic inclusions and inhomogeneities," *Progress in solid mechanics,* vol. 2, pp. 89-140, 1961.

[67] J. D. Eshelby, "The elastic field outside an ellipsoidal inclusion," *Proceedings of the Royal Society of London. Series A, Mathematical and Physical Sciences,* pp. 561-569, 1959.

[68] J. D. Eshelby, "The determination of the elastic field of an ellipsoidal inclusion, and related problems," *Proceedings of the Royal Society of London. Series A. Mathematical and Physical Sciences,* vol. 241, pp. 376-396, 1957.

[69] J. Dundurs and T. Mura, "Interaction between an edge dislocation and a circular inclusion," *Journal of the Mechanics and Physics of Solids,* vol. 12, pp. 177-189, 1964.

[70] J. Dundurs and G. Sendeckyj, "Edge dislocation inside a circular inclusion," *Journal of the Mechanics and Physics of Solids,* vol. 13, pp. 141-147, 1965.

[71] V. A. Lubarda, "Image force on a straight dislocation emitted from a cylindrical void," *International Journal of Solids and Structures,* vol. 48, pp. 648-660, Mar 1 2011.

[72] K. M. Davoudi, *et al.*, "A screw dislocation near a circular nano-inhomogeneity in gradient elasticity," *International Journal of Solids and Structures,* vol. 47, pp. 741-750, 2010.

[73] K. M. Davoudi, *et al.*, "Analysis of stress field of a screw dislocation inside an embedded nanowire using strain gradient elasticity," *Scripta Materialia,* vol. 61, pp. 355-358, 2009.

[74] H. Shodja, *et al.*, "Analysis of displacement and strain fields of a screw dislocation in a nanowire using gradient elasticity theory," *Scripta Materialia,* vol. 59, pp. 368-371, 2008.

[75] Q. H. Fang, *et al.*, "Screw dislocations in a three-phase composite cylinder model with interface stress," *Journal of Applied Mechanics-Transactions of the Asme,* vol. 75, Jul 2008.

[76] H. Wei, *et al.*, "Spontaneous growth of indium nanostructures," *Journal of Crystal Growth,* vol. 297, pp. 300-305, 2006.

[77] H. Song, *et al.*, "Nonlinear Kinetics of GaAs MOVPE Examined by Selective Area Growth Technique," *Journal of The Electrochemical Society,* vol. 154, p. H91, 2007.

[78] M. Coltrin, *et al.*, "Modeling the parasitic chemical reactions of AlGaN organometallic vapor-phase epitaxy," *Journal of Crystal Growth,* vol. 287, pp. 566-571, 2006.

[79] J. Randallcreighton, *et al.*, "Fundamental chemistry and modeling of group-III nitride MOVPE," *Journal of Crystal Growth,* vol. 298, pp. 2-7, 2007.

[80] A. A. Sirenko, *et al.*, "Strain relaxation and surface migration effects in InGaAlAs and InGaAsP selective-area-grown ridge waveguides," *Applied Physics Letters,* vol. 88, Feb 2006.

[81] A. Bourret, *et al.*, "Strain relaxation in (0001) AlN/GaN heterostructures," *Physical Review B,* vol. 63, 2001.

[82] W. Ye, *et al.*, "Finite element modeling of dislocation in solids and its applications to the analysis of GaN nanostructures," *Computational Materials Science,* vol. 58, pp. 154-161, Jun 2012.

[83] R. E. Miller and V. B. Shenoy, "Size-dependent elastic properties of nanosized structural elements," *Nanotechnology,* vol. 11, p. 139, 2000.

[84] V. G. Lee, "Derivatives of the three-dimensional Green's functions for anisotropic materials," *International Journal of Solids and Structures,* vol. 46, pp. 3471-3479, 2009.

[85] V. B. Shenoy, "Atomistic calculations of elastic properties of metallic fcc crystal surfaces," *Physical Review B,* vol. 71, p. 094104, 2005.

[86] J. D. Eshelby, "Screw dislocations in thin rods," *Journal of Applied Physics,* vol. 24, pp. 176-179, 1953.

[87] Y.-C. Pan and T.-W. Chou, "Point force solution for an infinite transversely isotropic solid," *ASME, Transactions, Series E-Journal of Applied Mechanics,* vol. 43, pp. 608-612, 1976.

[88] P. Sharma and S. Ganti, "Rapid Research Note Interfacial Elasticity Corrections to Size-Dependent Strain-State of Embedded Quantum Dots," *phys. stat. sol.(b),* vol. 234, pp. R10-R12, 2002.

[89] J. D. Eshelby, *et al.*, "Anisotropic elasticity with applications to dislocation theory," *Acta Metallurgica,* vol. 1, pp. 251-259, 1953.

[90] A. Stroh, "Dislocations and cracks in anisotropic elasticity," *Philosophical Magazine,* vol. 3, pp. 625-646, 1958.

[91] C. Hwu and W. J. Yen, "On the anisotropic elastic inclusions in plane elastostatics," *Journal of applied mechanics,* vol. 60, 1993.

[92] T. Ting and Y. Gongpu, "The anisotropic elastic solid with an elliptic hole or rigid inclusion," *International journal of solids and structures,* vol. 27, pp. 1879-1894, 1991.

[93] W. J. Yen, *et al.*, "Dislocation inside, outside, or on the interface of an anisotropic elliptical inclusion," *Journal of applied mechanics,* vol. 62, pp. 306-311, 1995.

[94] W. J. Yen and H. CHYANBIN, "Interactions between dislocations and anisotropic elastic elliptical inclusions," *Journal of applied mechanics,* vol. 61, pp. 548-554, 1994.

[95] A. Head, "The [111] dislocation in a cubic crystal," *physica status solidi (b),* vol. 6, pp. 461-465, 1964.

[96] Z. Liliental-Weber, *et al.*, "GaN grown in polar and non-polar directions," *OPTOELECTRONICS REVIEW,* vol. 12, p. 339, 2004.

[97] B. Hyun Kong, *et al.*, "Anisotropic strain relaxation and abnormal zigzag shape planar defects in nonpolar a-GaN grown by metalorganic chemical vapor deposition," *Journal of Crystal Growth,* vol. 313, pp. 8-11, 2010.

[98] Y.-L. Hu, *et al.*, "Extended defect structure of a-plane GaN produced by sidewall lateral epitaxial overgrowth," *Journal of Crystal Growth,* vol. 331, pp. 49-55, 2011.

[99] W. Ye, *et al.*, "Analytical formulations of image forces on dislocations with surface stress in nanowires and nanorods " *International Journal of Solids and Structures,* vol. 50, pp. 4341-4348, 2013.

[100] W. Ye, *et al.*, "On the elastic field and image force of dislocations in anisotropic solids and its application to GaN nanostructures," submitted, 2013.

[101] W. Ye, *et al.*, "Analytical close-form solutions to the elastic fields of solids with dislocations and surface stress," *Philosophical Magazine*, vol. 93, pp. 2497-2513, 2013.